Title

From mouse to human: Accessing the biochemistry of vision in vivo by two-photon excitation.

Authors

Wojtkowski, Maciej
Palczewski, Krzysztof
Palczewska, Grazyna

Publication Date

2023-03-01

DOI

10.1016/j.preteyeres.2023.101170

Peer reviewed

HHS Public Access

Author manuscript

Prog Retin Eye Res. Author manuscript; available in PMC 2023 August 29.

Published in final edited form as:

Prog Retin Eye Res. 2023 March ; 93: 101170. doi:10.1016/j.preteyeres.2023.101170.

From mouse to human: Accessing the biochemistry of vision *in vivo* by two-photon excitation

Grazyna Palczewska[1,2,3,4,#,*], **Maciej Wojtkowski**[2,4,5,#,*], **Krzysztof Palczewski**[1,6,#,*]

[1]Gavin Herbert Eye Institute, Department of Ophthalmology, University of California, Irvine, California, USA

[2]Department of Physical Chemistry of Biological Systems, Institute of Physical Chemistry, Polish Academy of Sciences, Warsaw, Poland

[3]Polgenix, Inc., Department of Medical Devices, Cleveland, Ohio, USA

[4]International Center for Translational Eye Research, Polish Academy of Sciences, Warsaw, Poland

[5]Faculty of Physics, Astronomy and Informatics, Nicolaus Copernicus University, Torun, Poland

[6]Department of Physiology & Biophysics, School of Medicine, and Chemistry, Molecular Biology and Biochemistry, University of California, Irvine, California, USA

Abstract

The eye is an ideal organ for imaging by a multi-photon excitation approach, because ocular tissues such as the sclera, cornea, lens and neurosensory retina, are highly transparent to infrared (IR) light. The interface between the retina and the retinal pigment epithelium (RPE) is especially informative, because it reflects the health of the visual (retinoid) cycle and its changes in response to external stress, genetic manipulations, and drug treatments. Vitamin A-derived retinoids, like retinyl esters, are natural fluorophores that respond to multi-photon excitation with near IR light, bypassing the filter-like properties of the cornea, lens, and macular pigments. Also, during natural aging some retinoids form bisretinoids, like diretinoid-pyridiniumethanolamine (A2E), that are highly fluorescent. These bisretinoids appear to be elevated concurrently with aging. Vitamin A-derived retinoids and their bisretinoidss are detected by two-photon ophthalmoscopy (2PO), using a new class of light sources with adjustable spatial, temporal, and spectral properties. Furthermore, the two-photon (2P) absorption of IR light by the visual pigments in rod and cone photoreceptors can initiate visual transduction by *cis-trans* isomerization of retinal, enabling parallel functional studies. Recently we overcame concerns about safety, data interpretation and complexity of the

[*]To whom correspondence should be addressed: Grazyna Palczewska, Department of Ophthalmology 837 Health Sciences Rd, Irvine, CA 92657; gpalczew@uci.edu; Tel: (949) 824-6527, Krzysztof Palczewski, Department of Ophthalmology 837 Health Sciences Rd, Irvine, CA 92657; kpalczew@uci.edu; Tel: (949) 824-6527, Maciej Wojtkowski, International Center for Translational Eye Research, ul. Skierniewicka 10A, 01-230 Warsaw, Poland; mwojtkowski@ichf.edu.pl; Tel: +48-607-293-453.

[#]co-first authors

11.Author contributions

All authors (G. P., K.P., M.W.) contributed to writing and editing the manuscript.

10.Conflict of interest

K.P. is the Chief Scientific Officer of Polgenix Inc., and a consultant for Editas Medicine. K.P. is Chief Scientific Officer at Polgenix, Inc. K.P. is an inventor of U.S. patents 7,706,863 and 8,346,345, whose values may be affected by this publication. G.P. is an employee of Polgenix, Inc. M.W. declared no conflict of interest exists.

2P-based instrumentation, the major roadblocks toward advancing this modality to the clinic. These imaging and retina-function assessment advancements have enabled us to conduct the first 2P studies with humans.

Keywords

vision; retinoid cycle; retina; optical nonlinear processes; two-photon absorption; two-photon excited fluorescence; two-photon SLO; two-photon vision; *in vivo* retinal imaging

1. Introduction

Color photography, narrow band reflectance photography, scanning laser ophthalmoscopy (SLO) and fundus autofluorescence are some of the methods currently being used for *en face* imaging of the retina. They provide 2-dimensional images of large areas of anatomy. In addition, Optical Coherence Tomography (OCT) provides volumetric data and differentiates layers of specialized cell classes in the retina. While each of these different imaging methods can offer insight into retinal structure, they do not always correlate reliably with visual acuity (Blumenkranz *et al.*, 2010). Furthermore, existing optical imaging tools are insensitive to early or low-grade tissue dysfunction, since they only reveal disease phenotypes after a structural phenotype already exists.

Light-evoked changes in the structure of retinal tissue have been quantified using new techniques of functional imaging of the retina (Hillmann et al., 2016; Jonnal, 2021; Pandiyan et al., 2020; Tomczewski et al., 2022; Zhang et al., 2019a). There is, however, a very different aspect of tissue function which is encoded at the biochemical level through absorption of light interacting with retinal fluorophores, and the ensuing fluorescence emission (Sauer *et al.*, 2019; Yung *et al.*, 2016). Conventional approaches to in vivo retinal imaging and studying retinal function are based on a one photon absorption of visible light, whereas more recent developments demonstrate the advantages of employing two-photon (2P) excitation of endogenous fluorophores. Two-photon ophthalmoscopy (2PO) and two-photon microperimetry both have great potential and only recently have been applied in humans.

2P excitation of endogenous fluorophores is an optical nonlinear effect in which the response of the light propagating medium depends nonlinearly on the light intensity. The advantages of 2P as compared to 1P excitation imaging arise from two physical properties, namely, excitation of molecules at twice the wavelength and localization (optical confinement), which enables spatial reduction of the fluorescence volume (Wang et al., 2010). When using near-infrared radiation, the first property allows the excitation radiation to be delivered deep into the tissue with decreased scattering and minimal absorption along the light propagation path. The second property, minimizes out of focus signal, resulting in low noise images, and avoids excessive bleaching of the dyes outside the tight focus of the light beam, thus avoiding phototoxicity. Consequently, spatial confinement can contribute to improved imaging resolution, even leading to breaking the diffraction limit barrier. (Betzig et al., 2006; Hell and Wichmann, 1994; Moerner, 2006). In this contribution, the reader will mainly find the advantages of two-photon studies related to the ability to excite endogenous

fluorophores associated with the processes sustaining vision using wavelengths in the near-infrared range that are not strongly absorbed and scattered by eye tissues.

After absorption of light, some endogenous chromophores (Fig. 1) release the energy by emitting fluorescence photons. Fluorophores remain in the excited state, followed by vibrational relaxation and fluorescence emission recorded over time as an exponential decay. Thus, in addition to the absorbance and emission spectra, fluorescence lifetime is another property of the molecule (Lakowicz *et al.*, 1992). These properties are influenced by the environment in which a fluorophore resides. Bi-exponential approximation of fluorescence lifetimes in response to 446-nm excitation of numerous substances including collagen, elastin, A2E, and NADH were reported previously (Schweitzer et al., 2007). Fortunately for eye imaging, the chemistry of our vision is based on retinoids that are fluorescent, specifically all-*trans*-retinol (all-*trans*-ROL) and retinyl esters. Their short excitation wavelengths, however, pose a problem for traditional one-photon (1P) imaging, as short-wavelength UV light poorly penetrates the front of the human eye (Boettner and Wolter, 1962). However, lasers delivering femtosecond (fs) pulses are capable of excitation of these fluorophores by two-photon (2P) absorption, thus pulsing IR can be used to interrogate nearly any tissue of the eye (Palczewska et al., 2020; Palczewska et al., 2010; Stremplewski et al., 2015). Because two-photon excitation (2PE) requires locally intense light power, there are concerns regarding tissue damage and the stability of the fluorophores involved. These concerns are somewhat diminished, because wavelengths of IR light that are used for two-photon excitation of retinal fluorophores are not strongly absorbed by the structures in the anterior chamber of the eye or by those in the retina. Nevertheless, extra precautions need to be taken in the case of live animals and humans.

Advantages of 2PE, namely transmission of IR light and ability to excite retinal fluorophores that would not be accessible to a 1P-based process have been presented in numerous studies. Data from human tissues *in vitro* and animal models *in vivo* have demonstrated that two-photon excited fluorescence (2PEF) imaging can identify a series of disease-specific biomarkers that are specific to particular diseases (Imanishi and Palczewski, 2010; Palczewska *et al.*, 2014b; Palczewska *et al.*, 2010). In addition to the endogenous fluorophores, many biomolecules and pharmaceuticals, can be tagged with highly efficient fluorophores and can be used to evaluate detailed structures or follow biological pathways.

The usefulness of 2P imaging was further demonstrated by the ability to detect early molecular changes in retinoid metabolism linked to light- and age-induced retinal defects, and the ability to assess the efficacy of treatments for such conditions. The sequence of events leading to retinal degeneration following bright-light exposure was delineated in the intact mouse eye (Maeda *et al.*, 2014), concurrently supporting the development of novel therapeutic strategies (Chen *et al.*, 2013). Moreover, the ability of 2P imaging to assess the functionality of induced pluripotent stem cells transplanted into the mouse retina (Maeda *et al.*, 2013) can be applied to similar studies in humans. In this context, 2P imaging provides an opportunity to monitor the integrity of the biochemical processes and structures of the retina and the RPE and their preservation or repair in response to diverse therapeutic approaches. Such applications of 2P imaging is a prominent subject of this review.

Fluorescence imaging with 2PE provides valuable information about the molecular state of the retina, but the very act of 2PE can also be the foundation for new clinical tools to study retinal function. Already in the 1940s, Wald and his colleagues began to study the topic of infrared vision, however systematic study and description of 2P-mediated IR vision had to wait for the development of novel optical devices, and critically, tunable picosecond (ps) and femtosecond (fs) lasers (Dmitriev et al., 1979; Griffin et al., 1947; Palczewska et al., 2014c; Ruminski et al., 2019; Zaidi and Pokorny, 1988).

In next paragraphs we discuss in detail advancements in understanding of the biochemistry of vision in health and disease, elucidation of retinal damage mechanisms and progression, and efficacy and mechanism of action of novel drug candidates which would not be possible without 2P-based imaging of the intact eye. We describe challenges that needed to be overcome to apply 2P-based technology to its first applications in humans; and we present successful implementation of this approach to measure visual function and 2P images of the eye in human subjects *in vivo*.

2. Two-photon excitation as a tool for understanding the biochemistry of vision

To gain a full understanding of the value of 2P imaging of the eye for assessing the health of the retina and the RPE, we must first consider the fluorophores available for investigation. As a result of the action of light on photoreceptors, the 11-*cis*-retinal (11-*cis*-RAL) chromophore of the visual pigment is photoisomerized to an all-*trans* configuration. (Hubbard and Wald, 1952; Wald, 1968). During the ensuing phototransduction cascade, the light receptor couples with its cognate G protein, eliciting conformational changes that trigger the subsequent steps in the visual transduction and retinoid cycle processes that lead to restoration of the light sensitive visual pigment (Palczewski, 2006). The maintenance of vision is dependent on mechanisms that regenerate ground-state visual pigments (Kiser *et al.*, 2014; McBee *et al.*, 2001). The canonical regeneration pathway was originally referred to as the “visual cycle”; however, it is probably more accurate to refer to it as the “retinoid cycle,” as it has been more commonly called in recent years (Fig. 2). As retinoids, such as all-*trans*-ROL, retinyl esters (RE in Fig. 2), and the derived compounds including A2E, are fluorescent molecules, 2P imaging can detect abnormalities in their processing, indicative of different disease states.

After photoactivation and hydrolysis of the visual pigment, the chromophore is released in the form of all-*trans*-retinal (all-*trans*-RAL) (Hong *et al.*, 2022), which is then reduced to all-*trans*-ROL within the outer segments of the photoreceptor cells (Dowling, 1960). All-*trans*-ROL is then transferred with assistance by the interphotoreceptor retinoid-binding protein into the RPE, where it undergoes esterification by an enzyme called lecithin:retinol acyltransferase (LRAT) (Andrews and Futterman, 1964), to form fatty acyl, all-*trans*-retinyl esters (Ruiz *et al.*, 1999). These retinyl esters are gradually converted *via* hydrolysis and isomerization into 11-*cis*-RAL, which then combines with apo-opsins to regenerate light-responsive, ground-state visual pigments (Dowling, 1960). A membrane-dependent retinoid isomerase activity was discovered in RPE cells of the retina and was identified as an

RPE-specific protein called retinoid isomerase (RPE65) (Jin *et al.*, 2005; Moiseyev *et al.*, 2005; Redmond *et al.*, 2005; Redmond *et al.*, 1998). Some of the intermediates and aberrant bisretinoids are fluorescent and can be observed by 2P imaging.

2.1. Discovery of retinosomes. Chemical reactions in the visual cycle vs. chromophores (molecular selectivity)

The authors of this contribution and their collaborators have employed 2P imaging to detect naturally abundant fluorophores in the eye. This imaging is based on the fluorescence of retinoid metabolites, and was found to be valuable in the study of mouse models of eye diseases involving defects in critical enzymes in the retinoid cycle. In an early study (Imanishi et al., 2004b), lipid-droplets were identified in the retinas of live mice and named "retinosomes," because they were found to contain retinyl esters in high concentrations. It was demonstrated by Imanishi *et al.* (2004) that retinosomes play an active role in the production of 11-*cis*-RAL *in vivo*, opening up the possibility of imaging this process at the subcellular level *in vivo* (Imanishi et al., 2004b). Further imaging experiments with different mouse models have shown that retinosomes over-accumulate in the eyes of $Rpe65^{-/-}$ mice, whereas retinosomes are absent in the eyes of $Lrat^{-/-}$ mice which are deficient in retinyl ester synthesis (Batten *et al.*, 2004; Batten *et al.*, 2005). The data presented herein support the corollary that 2P imaging can be used to detect defects in the retinoid pathways associated with genetic diseases that lead to blindness in humans through identifying defects in the pathways associated with these diseases (discussed below). Accordingly, genetic testing can be limited to a smaller number of genes.

2.2. Physical effects of two-photon absorption (2PA) and two-photon excited fluorescence (2PEF); Intensity based and fluorescence-lifetime imaging (FLIM)

A number of optical processes relate to how light interacts with matter, such as absorption, reflection, scattering, and refraction, which exhibit a linear dependence on the intensity of the incident light wave. In contrast, certain physical processes depend nonlinearly on the intensity of the incident light, including 2P absorption and the related 2PEF, which are both examples of nonlinear optical processes. 2P absorption was originally predicted by Maria Goeppert-Mayer in 1931 in her doctoral dissertation (Diaspro *et al.*, 2006; Goeppert-Mayer, 1931).

Atoms or molecules of a medium can be excited to an elevated energy level at a given time by absorption of a discrete amount of energy carried by light (photons). Thus, 2P absorption is understood as the simultaneous absorption of two photons with a combined energy that is equal to the energy required for excitation. The probability of occurrence of such an event depends on the square of the instantaneous light intensity or photon flux (the power density of light)(Masters and So, 2008).The 2P-absorption cross-sections for the 2P process are very small, on the order of 10^{-58} m^4s per photon (Xu and Webb, 1996), necessitating the use of light sources such as mode-locked short-pulse lasers that emit a large number of photons in a very short period of time, and focusing the light into very small volume.

Fortunately for imaging the retina by 2PE, wavelengths within the 700- and 1100-nm window correspond to the absorption spectra of molecules present in the retina and RPE,

and these wavelengths are well transmitted by the cornea, aqueous, lens, and vitreous layers of the eye. Therefore, it is possible to excite retinal fluorophores (which require UV for 1P excitation) by enabling the 2P process with IR. The effect of improved localization of 2PEF is evident by comparison with 1P excitation. Due to the quadratic dependence of the occurrence of the 2PE effect on the energy flux, the fluorescence light is generated only in a small volume at the focus of the lens, as shown in Fig. 3. In the case of 1P excitation, fluorescence production occurs in a much larger volume. This difference translates to two practical effects: 1. spatial localization in the case of 2PEF obviates the need for additional mechanisms such as a confocal pinhole; and 2, the detector can be placed as close to the sample as geometry allows so that all emitted photons can be collected, thereby improving collection efficiency (Schweitzer *et al.*, 2020).

In addition to improving image quality, the longer-wavelength light also has the advantage of being less susceptible to scattering. In the healthy and young human eye, scattering is mostly confined to layers outside the main imaging pathway (sclera, iris, RPE), whereas in older or elderly eyes, opacities of the lens and vitreous body impact transmission of visible light, making it much more difficult to image. As a result of advanced cataracts or corneal dystrophy, fluorescence imaging with optical instruments based on visible light becomes impossible, rendering the majority of diagnostic equipment useless in extreme cases.

The efficiency of 2P absorption and thus the fluorescence emission of a fluorophore, as measured by the number of photons that are absorbed per pulse by the fluorophore molecule n_a, is inversely proportional to excitation light pulse duration τ_p, and the square of pulse repetition frequency (PRF) ((Denk et al., 1990)):

$$n_a \approx \frac{p_0^2 \delta}{\tau_p PRF^2}\left(\frac{\pi NA^2}{hc\lambda}\right)^2, \quad (1)$$

where p_0 stands for average laser power, NA = numerical aperture of objective lens, c = speed of light, h = the Planck constant, δ = 2P absorption cross-section, and λ = wavelength.

According to equation 1, an increase in the efficiency of the 2PEF process can be achieved by reducing the duration of the laser pulses. It is important to note that this will result in an increase in pulse spectral bandwidth, leading to phase distortion caused by dispersion by the optical components of the imaging system as well as by the tissue itself. Thus it is essential that in the design of imaging systems, the dispersion introduced by the optical system and the tissue, is pre-compensated (Entenberg et al., 2011). However, when increasing pulse spectral bandwidth above the absorption spectral bandwidth of the dye, the absorption efficiency of 2P as a function of pulse duration tends to saturate (Pang et al., 2009). It is therefore crucial that PRF is optimized as a second factor that contributes to 2PEF efficiency. Additionally, it is vital to keep in mind safety constraints, since reducing PRF will result in an increase in peak power density for the same average power, which means that the tissue could be impacted by photochemical effects (Delori et al., 2007). There are a number of other factors that contribute to the performance of 2PEF imaging of the tissue, such as the light scattering and wavefront distortion caused by the tissue layers between the tissue of interest and the lens. In addition, a reduction in the power of laser light is also required to

achieve safe and repeatable imaging of the cellular and biochemical components *in vivo*. A number of additional hardware and software methods have been developed to overcome these limitations, such as the use of adaptive optics, high order dispersion compensation with Multiphoton Intrapulse Interference Phase Scan (MIIPS), or registering and averaging images obtained with low laser power levels with a low signal to noise ratio (Alexander et al., 2016; Biss et al., 2007; Cua et al., 2016; Geng et al., 2012; Hunter et al., 2010; Rossi et al., 2013; Vogel et al., 2006).

2PEF imaging offers the opportunity to identify and distinguish 2PEF signals from diverse fluorophores present in the retina. When measuring unstained samples *in vivo*, there are usually many compounds engaged in various biochemical processes, all contributing to signals detected in the same image pixel. There are a number of ways to quantify individual contributions from these diverse fluorophores; for instance, by fluorescence lifetime imaging (FLIM) and complementary spectral analysis of 2PEF light (Golfetto et al., 2015a; Malacrida et al., 2016; Rahim et al., 2022). Short pulse laser light used in FLIM enables the excitation and measurements of the timing of energy release by atoms and molecules. It is through a number of different pathways (radiative and/or non-radiative) that the excited fluorophore returns to the ground state. These pathways determine the fluorescence decay rate of the fluorophore (Fig. 4A). The fluorescence decay times (lifetimes) are several orders of magnitude longer than the duration of the single pulse of excitatory external electromagnetic field (fs). Using short laser pulses at a selected PRF, and high-speed electronics, it is possible to measure fluorescence decay rate by detecting the number of fluorescent photons as a function of time in a time-correlated single-photon counting scheme (TCSPC)(O'Connor and Phillips, 1984). Furthermore, by applying gating methods to filter out photons with selected arrival times it was possible to improve the discrimination between the fluorophores of interest (Palczewska et al., 2020). Similar information can also be obtained in the Fourier domain. As part of this measurement scheme, it is necessary to measure or calculate shifts in the phase of the fluorescence as related to excitation. Frequently TCSPC is used for the data collection and then, in post-processing, an approach developed for Fourier methods is used, such as the phasor technique (Golfetto et al., 2015b).

Fluorescence lifetimes are determined by a combination of the properties of the fluorophore and the local microenvironment in which it lives. It is possible to identify the distribution of chemical components of the imaged sample after measuring the fluorescence decay at each pixel in the image (Fig. 4B). In one approach, for each image pixel a multi-exponential curve was fitted to the measured fluorescence decay. Then, mean fluorescence lifetime (τ_m) was obtained using equation 2 (Sauer *et al.*, 2018),

$$\tau_m = \left(\sum A_i \blacksquare \tau_i\right) / \left(\sum A_i\right), \quad (2)$$

where the coefficients A_i and τ_i represent amplitudes and lifetimes based on the approximation of fluorescence decay (F) by the sum of 1, 2 or 3 exponential functions, such that $F = A_1 \blacksquare e^{-t/\tau_1} + A_2 \blacksquare e^{-t/\tau_2} + A_3 \blacksquare e^{-t/\tau_3}$.

Then, the arbitrary colors can be assigned to image pixels with selected fluorescence lifetimes. The combination of 2PEF and FLIM is a very useful tool for non-invasively

mapping the subcellular distribution of endogenous fluorophores based on their fluorescence lifetime data in animal models and human eyes. Combined with 2PEF process, FLIM can access fluorophores with 1P excitation spectra in the UV range. Moreover, it works well for thicker samples because the effects of photon scattering are reduced by using infrared wavelengths. It is important to note, that for both 1PEF and 2PEF FLIM data collection over a large area requires long acquisition times.

2.3. General description of the impact of 2PEF on the eye

When a photon reaches a photoreceptor cell in the eye, it gets absorbed by a visual pigment, initiating a cascade of processes that culminate in the sensation of vision. The first step in this process is photoisomerization of the visual chromophore, 11-*cis*-retinylidene to all-*trans*-retinylidene. For sustained vertebrate vision, the 11-*cis*-retinylidene needs to be continuously replenished *via* a metabolic pathway named the retinoid (visual) cycle. As a result of the biochemical reactions comprising the retinoid cycle, fluorescent retinyl esters are formed in the RPE, and bisretinoids accumulate in the RPE with age (Sparrow *et al.*, 2010). Retinosomes were discovered using non-invasive 2PEF microscopy of wild type (WT) mice and genetically modified mouse models (Imanishi et al., 2004b). The 1P excitation maximum of the retinyl esters at ~330 nm was the main reason for delayed discovery of the retinosomes, until 2PE was used to image the endogenous fluorophores in the intact eye (Imanishi et al., 2004b).

The ability to assess the function of the retinoid cycle in human eyes *in vivo* is becoming necessary for assessing therapeutic interventions (Palczewski and Kiser, 2020), owing to the advent of novel retinal therapies such as transplantation of retinal tissue layers derived from human embryonic stem cells or retinal organoids (Lin et al., 2020), or gene therapy. However, after fluorescent signals were obtained from retinosomes (Imanishi et al., 2004b), progress in 2-photon imaging of the human retina *in vivo* was constrained by concerns about the safety of retinal exposure to short-pulse infrared light. In addition, there have been a number of practical problems to overcome, such as the introduction of the Ti:Sapphire laser into clinical settings and the high cost of the apparatus required for such measurements. With the current rapid development of photonic technologies, including fiber lasers, it was possible to create a robust and compact clinical instrument and reduce the cost of such a system (Boguslawski *et al.*, 2022). In addition, previously acquired knowledge from experiments with animals enabled optimization of the operating conditions for the imaging system, including selection of the pulse duration Palczewska et al., 2018, central wavelength Palczewska et al., 2014a, and pulse repetition frequency Palczewska *et al.*, 2020). This optimization opened up prospects for new imaging methods to measure differences in the content and geographic localization of retinoid-derived molecules, which in the future will provide information on disease progression, retinal aging, and the impact of therapy.

3. Two-photon excited fluorescence (2PEF) imaging of animal models

3.1. Mouse models of human diseases. Relationship of mouse models to changes in fluorescence signals.

Retinosomes are elongated structures which have a diameter of 0.8 ± 0.2 μm, and a frequency of 36.2 ± 2.2 per double-nuclei RPE cells (Imanishi *et al.*, 2004a; Imanishi *et al.*, 2004c; Orban *et al.*, 2011)(Fig. 5A). The chemical and protein compositions of these structures was reported previously (Orban *et al.*, 2011). As mentioned above, retinoid-containing retinosomes over-accumulate in animals lacking retinoid isomerase, and their size is significantly enlarged in *Rpe65*$^{-/-}$ mice as compared to wild-type (WT) animals, because the esters cannot be converted into 11-*cis*-retinal in the mutant animals (Imanishi et al., 2004c; Palczewska et al., 2014a) (Fig. 5B). 2PEF-based analysis of retinoid-content in the *Rpe65*$^{-/-}$ mice corresponded with the concentration of the esters (Imanishi *et al.*, 2004c). The enzyme responsible for the retention of retinoids in the eye is lecithin-retinol acyl transferase (Lrat) (Batten *et al.*, 2004; Golczak *et al.*, 2015; Imanishi *et al.*, 2004b). Indeed, mice lacking this Lrat enzyme were unable to retain retinoid in the eye and no retinosomes are observable in 2PEF images (Fig. 5C). Specifically, *Lrat*$^{-/-}$ mice contained only residual amounts of retinoids (~8.3 pmol/eye versus about 1000 pmol/eye for WT mice), and no functional rhodopsin (Imanishi *et al.*, 2004c). Moreover, the aberrant bisretinoids in the animal model of Stargardt disease display a distinctive pattern and spectral characteristics unique for this disease (Chen et al., 2013; Maeda et al., 2011; Palczewska et al., 2020; Palczewska et al., 2014a; Palczewska et al., 2010). *Mertk*$^{-/-}$ mice lack the ability to recycle the outer segments because of defective phagocytosis. Consequently, membranous material accumulates around the tips of the photoreceptors. However, it was observed by 2PE imaging techniques that A2E and other bisretinoids were transported to, or formed *in situ,* in RPE cells lacking the phagocytosis process (Palczewska et al., 2016), documenting a phenotype for this animal model. Moreover, it was confirmed by alternative methods that bisretinoid fluorophores that form in photoreceptor outer segments occupy the un-phagocytosed outer-segment debris that accumulate in *Mertk*$^{-/-}$ mice (Zhao et al., 2018).Together, these observations verified that 2PO imaging could be used to demonstrate functional deficiencies in the visual cycle in animal models. Finally, documentation of increased bisretinoids in mouse and human eyes (Palczewska et al., 2014a) could inform the use of pharmacological agents to enhance visual cycle activity.

Bisretinoids are also fluorescent and accumulate in the RPE, and they tend to over-accumulate in mouse models of retinal dystrophies. Inadequate clearance and conversion of all-*trans*-retinal back to 11-*cis*-retinal through the visual cycle leads to accumulation of stable bisretinoids, A2DHP-PE and all-*trans*-retinal dimers, all of which are components of the lipofuscin of the RPE (Maeda et al., 2009b; Maeda et al., 2008; Sparrow et al., 2010). These by-products of the retinoid cycle have absorption spectra with second maxima in the range of 438 – 510 nm, distinctly different from the retinyl esters. Therefore, as the excitation wavelength is varied dominant fluorescent molecules become more visible. With 730-nm 2PE, retinyl esters in the retinosomes, which are located mostly next to cell membranes, are brightly visible in the images of the RPE (Fig. 6A). As the excitation wavelength is increased, fluorescence from retinosomes gets dimmer; however, other

fluorescent granules that are uniformly distributed in the interior of the cells become visible and contribute to RPE fluorescence (Fig. 6B). Moreover, fluorescence signals from these granules are markedly elevated in mouse models of Stargardt disease and in older WT animals in comparison to young WT mice; and there are other differences also in the fluorescence spectra among the three types of mice (Palczewska *et al.*, 2010). Thus, 2P imaging with different excitation wavelengths combined with spectral analysis can be used to provide information about the distribution and relative quantity of diverse Vitamin A derivatives as they undergo molecular transformations to sustain vision; or to detect aberrant formation of bisretinoids reflective of aging or disease.

3.2. Fluorophore-selective imagining

The contribution of retinyl esters and bisretinoids to fluorescence-based images, obtained with 2PEF microscopy with spectral detectors and hyperspectral imaging with tunable lasers was further validated by analytical measurements of these compounds in mouse eyes (Palczewska *et al.*, 2010). Higher precision in identifying molecular content of individual fluorescent granules in the RPE images was achieved by applying phasor analyses to 2PEF lifetime data (Palczewska *et al.*, 2020). In this approach, the lifetime decay data were collected individually for each image pixel by measuring photon arrival time as the difference between the photon detection event and the corresponding excitation pulse. The pseudo color scale for FLIM imaging was assigned based on a phasor plot formed by converting the data for each pixel from the time domain to the phase domain, using a phasor transformation relationship (Malacrida *et al.*, 2021):

$$x_{i,j} = g_{i,j} = \int_0^T I_{i,j}(t) \cdot \cos(2\pi \cdot PRF \cdot t)dt / \int_0^T I_{i,j}(t)dt \tag{3}$$

$$y_{i,j} = s_{i,j} = \int_0^T I_{i,j}(t) \cdot \sin(2\pi \cdot PRF \cdot t)dt / \int_0^T I_{i,j}(t)dt \tag{4}$$

Thus, phasor points representing fluorescence decay in each individual image pixel are plotted in the Cartesian coordinate system with x and y coordinates obtained from the phasor transformation. Moreover, it was shown that phasor points are located within a universal semicircle to form a phasor plot. Phasor points located on the line of the universal semicircle, can be assigned a mono-exponential fluorescence lifetime (τ), following the formula $\tan(\Phi) = 2*\pi*PRF*\tau$, where Φ is the angle between the X axis and a line connecting the phasor point with the origin of the Cartesian graph; and the PRF of the excitation light. Accordingly, for PRF = 80 MHz, the values of $\Phi = 0$ degrees and $\Phi = 45$ degrees on the universal semicircle phasor plot correspond to 0 and 2 ns, respectively. Phasor points located inside the universal circle contain contributions from multiple components, such that the relative contribution of each component is reflected in the distance between the particular phasor point and the phasor positions of the pure components. By selecting clusters of phasor points and assigning them arbitrary colors, the same colors are assigned to the corresponding pixels in the image, allowing one to visualize the geographical distribution of molecules with the same fluorescence lifetime. By analyzing fluorescence lifetimes from

artificial standards in relationship to the analysis of mice with genetically modified proteins the identity of molecules and their relative content can be calculated. These analyses were used to obtain the FLIM shown in Fig. 7. Images of RPE of *Rpe65*$^{-/-}$ mice, the model of Leber congenital amaurosis, are shown in Fig. 7A.

Because these mice have an impairment of the retinoid cycle due to the lack of retinoid isomerase Rpe65, the measured fluorescence is only from retinosomes containing retinyl esters (Orban *et al.*, 2011). Thus, the location of phasor points corresponding to retinyl esters was defined. The RPE of *Abca4*$^{PV/PV}$*Rdh8*$^{-/-}$ mice, which have a mutations in the ABCA4 transporter and lack retinol dehydrogenase 8 (Zhang et al., 2015c) and display many of the features of human Stargardt disease, is shown in Fig. 7B. These mice over-accumulate bisretinoids. Thus, with 730- nm excitation, contributions from bisretinoidst such as A2E are visible in the phasor plot, in addition to the retinyl esters. By assigning graded colors from red to blue to clusters of phasor points, image pixels with variable content from predominantly retinyl esters to predominantly bisretinoids can be visualized. Moreover, with 850-nm excitation, only bisretinoids such as A2E can be visualized by 2P microscopy (Fig. 7C), thereby establishing their position on the phasor plot obtained by FLIM analysis of the intact mouse eye *ex vivo*.

Complementary to FLIM, phasor approach-based spectral analysis of the 2PE fluorescence data (Fereidouni *et al.*, 2012) can provide information about distribution of endogenous fluorophores in the retina. This information is extremely valuable when assessing progress of retinal disease or efficacy of the therapy aimed at arresting the disease. This application is especially important now, considering advances in gene therapy technologies. A recent example, Suh *et al.* showed that after successful adenine base-editing in mouse models with a pathogenic mutation in the *Rpe65* gene, restoration of visual function was concomitant with reduction in the over-accumulation of retinyl esters (Suh *et al.*, 2021). Furthermore, in a Stargardt-disease mouse model, namely *Abca4*$^{-/-}$*Rdh8*$^{-/-}$, accumulation of A2E was reduced, and the outer nuclear layer was preserved after 3 months of daily treatment with pharmaceuticals containing a primary amine (Maeda *et al.*, 2011). Thus, noninvasive assessment of the contents and distribution of these fluorescent molecules in the eyes is important not only for screening the relative efficacy of drug candidates but also for longitudinal studies of the effectiveness of the drugs.

To form a spectral phasor plot, the fluorescence emission spectrum (Fig. 8A) for each pixel is converted into a phasor point on a Cartesian graph, as previously described (Golfetto et al., 2015b; Palczewska et al., 2020); x and y coordinates have values from −1 to 1 (Fig. 8B), such that a point at *(1,0)*, or a φ angle equal to 0 degrees, corresponds to the start and end of the measured spectral span. The angular position of the phasor point correlates with the center of mass of the spectrum of the corresponding image pixel, such that increasing φ corresponds to longer wavelength. Furthermore, the radial position of the phasor point is related to the spectral full width half maximum (FWHM) of the image pixel, such that image pixels with larger FWHM values are located closer to the origin of the graph (0,0). Image pixels with similar spectral properties form clouds of phasor points located nearby. By comparing data from artificial standards with those obtained from the tissue, identity of the fluorescing species can be deduced, and their distribution can be visualized. By selecting

groups of phasor points and assigning them arbitrary colors, image pixels with various spectral features can be differentiated.

With 850-nm 2PE of the RPE in *Abca4*$^{PV/PV}$*Rdh8*$^{-/-}$ mice (Fig. 8C), retinyl esters cannot be efficiently excited; thus, the red circle corresponding to the location where retinyl ester phasor points were expected is empty, and the cluster of phasor points highlighted by the teal circle is localized in the vicinity of the A2E spectral phasor points (Palczewska *et al.*, 2020). With 730-nm excitation both retinyl esters and bisretinoids could be visualized. Thus, the relative distribution of these molecules in the RPE could be distinguished (Fig. 8D). Consistent with FLIM data, retinosomes were located predominantly near the cell membranes, whereas biretinoids were localized within the cell body.

3.3. *In vivo* mouse imaging

The functional and structural information obtained with 2P imaging of *ex vivo* eyes and tissue has proven to be very valuable for evaluations of experimental therapies (Maeda et al., 2013), for studies of the biochemical pathways supporting vision (Imanishi and Palczewski, 2010), and for elucidation of changes leading to retinal degeneration after exposure to bright light (Maeda et al., 2014). However, several inventions and technological developments needed to be accomplished before the benefits of 2P imaging could be applied safely to evaluation and diagnosis of retinal health in the clinic. A first necessary step was to devise the delivery mode for short-pulse IR light through the pupil of the eye in a living animal and an efficient method of collection of fluorescence photons (Fig. 9A). In 2P imaging, it is critical to control the quality (size and intensity) of the excitation beam to maximize 2P fluorescence and to optimize the achievable spatial resolution (Fig. 3). This optimization was accomplished by using a sensorless adaptive optics system with an adaptive element, namely a deformable mirror situated only in the excitation-beam path. In this approach, the shape of the deformable mirror, is adjusted according to quality metrics for the 2P image, using a software algorithm based on either sequential optimization of Zernike modes (Thibos et al., 2002), or stochastic parallel gradient descent, without the need for a wavefront sensor or an additional associated light source (Palczewska et al., 2014a; Vorontsov and Sivokon, 1998). Using this approach and 730-nm light, the distribution of retinosomes could be discerned in the RPE of the eye of a live *Rpe65*$^{-/-}$ mouse (Fig. 9B). Likewise, quantities and localization of fluorescent granules formed after illumination with bright visible light, and responses to 850-nm light can be assessed and measured in a live *Abca4*$^{-/-}$*Rdh8*$^{-/-}$ mouse. Lastly, fluorescence emission spectra (Fig. 9C) were consistent with the expected identities of the fluorescent species; namely, retinyl esters in *Rpe65* $^{-/-}$ mice and bisretinoids in *Abca4*$^{-/-}$*Rdh8*$^{-/-}$ mice.

Safety considerations—To realize the potential of two-photon excitation imaging for early detection of retinal disease before pathological changes occur in living human eye, two barriers needed to be overcome: 1) concerns about the safety of retinal imaging with 2PE; and 2) interpretation of 2P imaging data in correlation with retinal disease. To minimize the potential for melanin-mediated interference with imaging the eye structures and to address safety concerns, fine modulation of spatial, temporal, and spectral properties of the excitation light were harnessed to maximize the signal while minimizing exposure to laser

light (Delori et al., 2007). These experiments were carried out with a custom periscope objective, which efficiently coupled the excitation light and collected photons emitted from the RPE and the retina (Palczewska et al., 2018). Reducing IR-light pulse duration from 75 fs to 20 fs and pre-compensating for the high-order spectral dispersion introduced by optical components and the eye itself resulted in a signal increase of 300% for the same average laser light power incident on the eye. Increased efficiency of two-photon excitation using 20 fs pulses enabled visualization of retinal layers from RPE to GCL in unstained intact $Abca4^{PV/PV}Rdh8^{-/-}$ mouse eye (Movie 1). Furthermore, extensive safety studies did not detect any changes in the mouse eyes after exposure to 2P imaging conditions with short pulse infrared light. These safety studies included: *in vivo* imaging with SLO and OCT; retinal function assessment by ERG; measurements of rhodopsin and 11-*cis*-retinal; *ex vivo* microscopic imaging of retinal sections immuno-labelled for glial fibrillary acidic protein (GFAP); and histology and 2P imaging of the RPE. These results were consistent with a 1 mW exposure during the imaging, which was well below the calculated maximum permissible exposure of 3.6 mW (Palczewska et al., 2018). However, a greater safety margin was desired for translating 2P imaging to humans. This was achieved by incorporating a laser-pulse selection system, enabling reduction of PRF from the typically used 80 MHz. Extensive modeling of imaging conditions using a PRF reduced to 8 MHz ruled out plasma-mediated effects and nonlinear chemical effects as potential sources of photodamage, and documented that melanin-related thermally induced damage can be mitigated by a reduction of PRF. With pure compounds for the same average laser power fluorescence increased 10-fold when decreasing PRF from 80 MHz to 8 MHz (Palczewska et al., 2020).

With this approach it was possible to image live pigmented animals and characterize the distribution and spectral and fluorescence lifetime properties not only of retinyl esters and bisretinoids, but also of melanin (Palczewska *et al.*, 2020). The fluorescence lifetime of choroid melanin was found to be 0.15 ns, and the corresponding cluster of phasor points was located near the *(1,0)* coordinate on the universal circle phasor plot. The RPE mosaic and subcellular distribution of retinosomes are distinctly visible in 2PE fluorescence intensity-based images of the RPE of pigmented $Rpe65^{-/-}$ mice (Fig. 10A). In this mouse model, only retinyl esters in retinosomes and melanin contribute to RPE fluorescence; thus phasor points (Fig. 10B) with greater contribution from melanin than retinyl esters are located closer to the *(1,0)* coordinate. The gradient of colors from blue to red, representing increasing contribution from retinyl esters after selection of phasor points, was used as an arbitrary color scale bar for FLIM images (Fig. 10C). Furthermore, when shifting the focal position of the excitation beam by 20 μm from the outer retina towards the choroid, the quantity and size of red-colored pixels was decreased, indicating increased contribution of melanin. As a side note, under the effective imaging conditions, the numerical aperture (NA) was equal to 0.35, and the estimated 1/e axial squared intensity beam width was 11 μm (Zipfel et al., 2003b). When the excitation wavelength was increased from 740 nm to 760 nm, the contribution of melanin to the pixel phasor points was even more pronounced, as can be seen by even less red-colored image pixels and more dark-blue pixels. This result is consistent with the fact that the 2P action spectra of RPE retinosomes (retinyl esters) show a steep decrease in a range from 740 nm to 760 nm (Palczewska *et al.*, 2018). Taking advantage of the fact that melanin has a very short fluorescence lifetime as compared with retinyl

esters, the clarity of images of RPE-retinosomes could be improved by rejecting photons with very short detector arrival times (Fig. 10D). Here we found that the optimal setting for this stop-gating was 0.09 ns after the decay maximum (Fig. 10D graph and inset).

3D reconstructions of multilayer retinal structure in the intact eye—Conversion of images, formed on the retina by combined focusing by the cornea and lens, into nerve impulses requires cooperative functions of all of the retinal cell types and the RPE. Thus, 3D reconstructions of the retina and RPE based on 2P images obtained from the intact eye provides information about the processes that sustain vision, any pathological changes, and the structural integrity of a system composed of the multilayer retinal structures and interdigitated RPE cells. Mutations in human MERTK have been linked to autosomal recessive retinitis pigmentosa that can result in complete blindness (Gal *et al.*, 2000). Loss of the *Mertk* gene in mice causes complete loss of the process of phagocytosis of photoreceptors by the RPE and results in a build-up of cellular material at the photoreceptor-RPE interface and ultimately retinal degeneration (Duncan *et al.*, 2003). *Ex vivo* assays using primary RPE cells and isolated photoreceptor outer segments are important parts of a comprehensive strategy to study RPE phagocytosis (Law *et al.*, 2015); however, an ideal study would include a non-destructive imaging method that allows imaging of phagocytic events within the intact eye. To study the progression of retinal degeneration in mice lacking MERTK, 2PE was used to image the retina and the RPE in the intact eyes of these mice (Palczewska *et al.*, 2016). Enlarged photoreceptors and macrophages were observed already in two-month-old animals, whereas no such structures were detectable in the eyes of control BALB/cJ mice (Fig. 11A, B). Images of neuronal retina in WT animals based on 2PE of endogenous fluorophores in the intact eye lack sufficient contrast, so intraocular injections with fluorescent dye-tagged peanut agglutinin were used to obtain low noise images over the 200 μm thick retina, from the outer segments to the ganglion cell layer (Fig. 11C), and to visualize details of the photoreceptors interdigitating with the RPE (Movie 2) The details of such intraocular injections were previously described (Palczewska *et al.*, 2018).

3.4. Drug impact and mechanism of drug action

2PE- microscopy imaging can offer insight into pathological changes in the retina and RPE, as well as facilitate study of the mechanistic aspects of degeneration. Here, we provide an example of this approach (Fig. 12). A long-standing observation is that intense illumination leads to destruction of the photoreceptors and the RPE (Organisciak *et al.*, 1998). One mechanism for this pathology is related to bisretinoids(Sparrow *et al.*, 2003; Sparrow *et al.*, 2012). Alternatively, and not mutually exclusive, free all-*trans*-retinal also is very toxic to the retina/RPE (Chen *et al.*, 2012). Using 2PEF microscopy and pharmacological agents could provide additional information on these two mechanisms. The all-*trans*-retinal released during bleaching is primarily toxic to photoreceptor cells rather than to the RPE, as shown by 2PEF microscopy (Maeda *et al.*, 2014).

With $Abca4^{-/-}Rdh8^{-/-}$ mice a 30–60 min intense light results in formation of enlarged photoreceptor outer segments in their retinas (Fig. 12). Thus, there were 43,242 enlarged photoreceptors per mm^2 in the eyes of mice exposed to light and treated with vehicle only (soybean oil). The dramatic protective impact of treatments was observed with potent

inhibitors of RPE65 such as Emixustat ((Fig. 12), about 400 enlarged photoreceptors per mm^2 in mice); and many other RPE65 inhibitors containing an amine functional group were also effective (Blum *et al.*, 2021; Golczak *et al.*, 2005; Yu *et al.*, 2021; Zhang *et al.*, 2015a). Indeed, simple primary amino-containing drugs were also protective (Maeda et al., 2011). Moreover, it was demonstrated that Emixustat and other primary amino-containing compounds form Schiff-base adducts transiently with all-*trans*-retinal *in vitro*, and that these retinylidene adducts can be trapped *in vivo* (Zhang et al., 2015b). The protective effects of Emixustat against light-induced retinal damage appears to be critically dependent on its ability to sequester all-*trans*-retinal; however, it cannot be *excluded* that inhibition of RPE65 plays a contributing protective role for some of the compounds tested. Clearly sequestration appears to be the primary protective mechanism, as reflected by the failure of MB-002, the diol derivative of Emixustat that lacks a reactive amino group, to protect against light-induced retinopathy in mice (Fig. 12); and by the effectiveness of amino compounds that do not inhibit RPE65 (Maeda et al., 2011). In short, 2PEF microscopy can document pathological events in retinal degeneration, probe the protective effectiveness of pharmacological agents, and provide evidence related to the mechanism of action of the drugs.

The undisturbed flow of nutrients, retinoids and metabolic products between the RPE and the photoreceptor cells is essential for sustaining eyesight (Hurley, 2021). Volumetric 3D visualization of these cells in the intact eye can provide information about the sequence of steps leading to retinal degeneration, and identify which cell type is impacted first. To gain insights about the initiation of retinal pathology after exposure to bright light the *Abca4* $^{-/-}$*Rdh8* $^{-/-}$ mouse model was used. This model was chosen because it is light sensitive, and defective ABCA4 function has been associated with Stargardt disease (Allikmets *et al.*, 1997). To make these mice more sensitive to light-induced degeneration, the Rdh8 gene from the chromophore recycling pathway was eliminated also (Kolesnikov et al., 2013; Kolesnikov et al., 2015; Maeda et al., 2009a; Shiose et al., 2010).

Using 2PEF imaging of intact mouse eyes before exposure to bright light (Fig. 13A), and after exposure to 10,000 lux for 60 min on day 1, 3 and 7, it was found that the first indication of ensuing pathology, noticeable already at day 1, was enlargement of the photoreceptor outer segments (Maeda *et al.*, 2014). Nearly 3-fold enlarged photoreceptors were abundant on day 3 after the exposure (Fig. 13B). Moreover, at day 3 macrophages infiltrated the photoreceptor space. The quantity of macrophages was highest at day 7, and at that time the photoreceptors were all gone (Fig. 13C) and only large fluorescent granules were detected in the subretinal space. Furthermore, increased fluorescence from RPE-retinosomes was observed at day 1 and 3; and that fluorescence decreased by day 7, in agreement with changes in content of retinyl esters in these animals, measured by HPLC. By day 11 multiple large fluorescent granules were present in the RPE (Maeda *et al.*, 2014). These larger fluorescent granules were clearly visible in the RPE with both 730-nm and 850-nm excitation light. Thus, by using 2PEF imaging with 3D reconstruction, it was determined that after exposure to bright light degeneration of photoreceptors occurred first and was followed by changes to the RPE. The methodology described above can be used also to study the impact of drug candidates on retinal preservation.

Advancing the application of non-invasive imaging is essential for visualizing biochemical pathways at subcellular resolution as they occur *in vivo*, thereby revealing details about natural biological processes, and how they are impacted by disease and therapeutics. Knowing the distribution of therapeutic agents is critical to elucidating their mechanism of action, bioavailability, clearance, and duration of action to determine the appropriate frequency of treatment. Triamcinolone, administered *via* intravitreal injection, was one of the first steroids used for the treatment of intraocular proliferation (Tano *et al.*, 1980). However, it was not until ganciclovir was used as an intravitreal implant to save the vision of HIV patients with severely compromised immune systems that intravitreal drug delivery was considered seriously as a major avenue for administering drugs for ocular diseases (Martin *et al.*, 1999). As the incidence of cytomegalovirus disease was reduced and the progression of the retinitis was delayed in a dramatic way, the number of intravitreal injections for drug delivery grew robustly (10,000 in 2003 to 25 million in 2018; https://www.retinalphysician.com/). Intravitreal delivery of steroids such as fluocinolone (Jaffe *et al.*, 2000) and anti-VEGF treatments for the wet-form of AMD soon followed (Rosenfeld *et al.*, 2005). Today, intravitreal injection of anti-angiogenic drugs has emerged as the most effective therapy for AMD; and placement of sustained-release drug-delivery devices in the vitreous chamber theoretically could further decrease the burden of frequent treatment, but for some drugs this approach remains elusive. Nonetheless, active development of such devices remains an objective in both academia and industry.

Due to the success of anti-VEGF treatments (Ferrara and Adamis, 2016; Kovach et al., 2012), intravitreal injection remains a viable means of drug delivery. However, challenges associated with intravitreal drug delivery persist, especially when considering accurate determinations of drug bioavailability and pharmacokinetics. This is acutely problematic when attempting to develop new drugs for common disorders that cause blindness; *e.g.*, the dry form of AMD, for which no effective therapy is currently available. Non-invasive imaging has the potential to determine the distribution of a drug, and provide insights about the pharmacokinetics and pharmacodynamics of drug candidates introduced into the eye.

The anti-neovascular agents ranibizumab (Lucentis), bevacizumab (Avastin), and aflibercept (Eylea), are injected intravitreally to reduce neovascularization associated with the wet form of AMD, and to diminish visual symptoms. This treatment is effective for numerous retinal and choroidal vasculopathies (Amoaku et al., 2012; Artunay et al., 2009; Cheung et al., 2017; Diabetic Retinopathy Clinical Research et al., 2015; Gulati et al., 2011; Kovach et al., 2012; Pe'er et al., 1998; Semeraro et al., 2013a). These anti-VEGF drugs appear to be efficacious and safe for chronic use *via* monthly injections into the vitreal space. Bevacizumab is a recombinant humanized monoclonal-IgG1 antibody that binds to vascular endothelial growth factor (VEGF), preventing receptor binding and inhibiting endothelial cell proliferation and vessel formation. Ranibizumab is a monoclonal-antibody fragment created from the same parent mouse antibody as bevacizumab, but without the FcRn binding domain. Aflibercept, sometimes referred to as VEGF-TRAP, is a fusion protein which includes binding sequences of VEGF receptors R1 and R2 and the Fc portion of human IgG1 (Semeraro et al., 2013b; Stewart, 2011). Although these three therapeutic biologics differ in molecular structure, they all help to reduce formation of new blood vessels, and to minimize vascular leakage. However, assessment of their distribution in the eye, and

whether each agent has reached its target, is not possible with existing technologies like OCT and scanning laser ophthalmoscopy (SLO). The concern is whether such drugs are compartmentalized in specific areas of the eye, which would limit their action and the ability to measure their pharmacodynamics and pharmacokinetics. Furthermore, intravitreal administration of ranibizumab has been associated with renal damage in some patients (Morales *et al.*, 2017).

. All three agents rapidly moved into the bloodstream, but ranibizumab was cleared very quickly, whereas bevacizumab and aflibercept displayed greater systemic exposure, and produced a marked reduction in plasma free VEGF. Thus, these drugs can penetrate into the blood circulation and alter systemic VEGF with unknown clinical consequences (reviewed in (Fogli *et al.*, 2018; Garcia-Quintanilla *et al.*, 2019)). More direct pharmacokinetics studies were undertaken by Mayer *et al.* (Meyer *et al.*, 2016). These authors used a rodent model to assess fluorescent probes linked to antibodies against VEGF for *in vivo* imaging. Importantly, fluorescently tagged antibody-conjugates retained target-binding affinity and showed no toxicity.

As noted, all three anti-VEGF drugs are retained in the eye in different compartments and they clear with different kinetics. Non-invasive 2PE imaging of mouse eyes at different time points after intraocular administration of these fluorescein-labeled drugs was used to assess their distribution, identify binding sites and monitor their clearance (Fig. 14). This methodology can be used for many drugs that are either intrinsically fluorescent or can be tagged with a fluorescent moiety. Such methods are surprisingly underutilized to study *pharmacokinetics* and *pharmacodynamics* of ocular drugs.

3.5. Retinal imaging of primates

In addition to 2P imaging of the eyes (Imanishi and Palczewski, 2010; Palczewska et al., 2014b), we tested whether two-photon excitation imaging could be used to assesses the two types of retinoids in primate eyes also. Thus, 2PE imaging, along with high-performance liquid chromatography (HPLC) and mass spectrometry (MS), was used to measure the contents of A2E, and distribution of 11-*cis*-retinyl esters, all-*trans*-retinyl esters, 11-*cis*-retinal oxime, all-*trans*-retinal oxime, 11-*cis*-retinol, and all-*trans*-retinol in macaque and human eyes. Significant amounts of retinyl esters were found in macaque and human eyes, and the highest total amount of ocular retinoids was in the macula, a finding consistent throughout the studies of macaque eyes (Jacobson *et al.*, 2007). Especially prominent were 11-*cis*-retinyl esters. The 11-*cis* esters are not detectable in WT mouse eyes; however, they contribute to the fluorescence signal from monkey and human retinas. These data indicated that there were sufficient amounts of retinyl esters in the human eye to obtain two-photon excitation images. The results of A2E analysis revealed that in primate eyes A2E content was ~0.2 pmol per mm^2 of fundus area, comparable to ~0.3 pmol per mm^2 in 6-month-old WT mice (Maeda *et al.*, 2008).

A regular mosaic of RPE cells was revealed by two-photon excitation studies with 730-nm imaging of human eyes. The macular RPE exhibited the highest fluorescence, whereas the equatorial and foveal RPE showed reduced fluorescence (Imanishi and Palczewski, 2010). In macaque eyes imaged *ex vivo* with 2PE, cone to cone distance decreased with the

eccentricity (Fig. 15); consistent with other reports, at 1, 6, and 10 mm away from the fovea the corresponding distances were 7.4 ± 0.5 μm, 12.8 ± 2 μm, and 18.3 ± 3 μm, respectively. Thus, 2PE provided informative images of the RPE and retina in the primate eye. Altogether these studies documented that the benefits of 2PE imaging of the RPE/retina in mice could be extended to primates.

4. Two-photon imaging of the human eye *in vivo*

4.1. Two-photon ophthalmoscope (2PO)

An illustration of the 2PO optical system is shown schematically in Fig. 16. The detailed rationale for choosing this configuration has been described (Boguslawski *et al.*, 2022). Several key features of the design enabled imaging under conditions that are well below safety limits, including: a) incorporation of a fiber laser with adjustable PRF; b) a wide field of view, providing for efficient collection of fluorescent photons, and averaging of signals from multiple frames. By decreasing the number of optical components and the total thickness of the glass, compact chromatic dispersion compensation was sufficient to minimize pulse duration in the retina. In 2PEF, photons are generated only in the focal volume (Fig. 3); f

In detail, the short-pulse Er:fiber laser delivered 40-fs pulses with a central wavelength of 1560 nm and was coupled to a second harmonic generation (SHG) module, which in turn produced 76-fs pulses of light with a wavelength of 780 nm. It was possible to set the PRF of the laser within a range of 1–12 MHz. Laser light was then routed through the galvanometric scanners that deflect the beam so that an X_Y scanning pattern was traced on the retina. It was found that optimal small beam size was produced on the retina when the incident beam size on the pupil was at 3 mm ($1/e^2$) (Donnelly and Roorda, 2003). As a safety measure, a shutter on a motorized flip mount was incorporated, and closed whenever the beam was not scanned. Furthermore, the position of the last lens in front of the eye was adjustable, so that it compensated for variations in the refractive properties of the eye. In this configuration, the maximum field of view (FOV) of the system was 17.6°. There were two signal recording channels in the 2PO instrument. One was a 2P-fluorescence channel with a minimal number of optical elements, and the other channel allowed the recording of backscattered signals from the retina by an avalanche photodiode in near-infrared SLO (NIR-SLO). The same light source was used in both signal recording channels; however, the detection spectral bandwidths were different between the two channels using dichroic mirrors. As a result of the placement of an additional set of bandpass filters in front of the photomultiplier tube, it was possible to completely remove excitation and scattered light from the 2PEF channel.

To obtain spectral information about the retinal fluorophores, bandpass filters were exchanged. The NIR-SLO images were used to position the eye before imaging, to correct for motion artifacts within the frame, and to correct for motion artifacts within the NIR-SLO images. With the implementation of the raster scanning protocol, 256×256-pixels images were collected at a rate of 0.76 frames per second. Lateral resolution was 21 μm, and the axial resolution was 130 μm. With the help of an ophthalmic chinrest, the subject's head was stabilized to arrest Its motion. An imaging experiment was conducted in a dark room

in which the volunteers' heads were covered with a black cloth without any adaptation to darkness, and without dilation of their pupils during the experiment. A total of thirty frames were acquired over the course of 40 seconds, followed by a pause of at least 60 seconds. After repeating the procedure, a total of 90–1000 frames were collected, and they were used for further processing and analysis.

4.2. 2PEF Imaging of healthy volunteers

Fig. 17 displays representative results of the first imaging study of a human eye *in vivo*, showing recognizable features. Images shown in Fig. 17 (A–C) were recorded in the spectral band from 400 to 700 nm. The images containing a reconstruction of a significant portion of the optic nerve disc were captured at approximately 8° of nasal eccentricity from the fovea. To obtain a 2PE-based 2PO image, the average of 100 2PE measurements were obtained (Fig. 17 A). In turn, averaging of 1,000 measurements yielded a 2PE image with SNR and quality comparable to the corresponding SLO image (Fig. 17 E). Averaging the 1P SLO measurements improved the dynamic range; however, averaging 1000 frames *versus* 100 frames did not make a significant difference in the quality of the reconstructed 1P SLO image (Fig 17 D–F). A noise level observed in the 2PO channel (Fig. 17 I) was at least 10-times lower than the 2PEF signal. A comparison was made between the fluorescence imaging results obtained with the short-pulse laser and those obtained with continuous wave (CW) excitation at 825 nm (Fig. 17 C, F). The images obtained by the NIR-SLO channel were comparable to those produced by the pulsed laser (Fig. 17 E, F) while the signal in 2PO channel was at a noise level for the CW laser. As a confirmation that no changes had occurred in the measured eyes, reference measurements were made using two other methods for measuring retinal autofluorescence, the B-FAF (blue light-induced one-photon fluorescence) method and the NIR-FAF (infrared light-induced one-photon fluorescence) method (Fig 17 G, H). The B-FAF technique is limited to imaging the distribution of bisretinoids (Delori *et al.*, 1995) while the NIR-FAF technique *enables detection of RPE melanin and to a lesser extent choroidal melanin* (Cideciyan *et al.*, 2015). If the fluorescence of other retinal chromophores were to be detectable, one would have to employ an excitation wavelength shorter than 473 nm; but this is not possible, due to increased phototoxicity and absorption in the anterior segment of the human eye. Additionally, excitation of RPE by short wavelengths in the blue range can lead to toxicity from bisretinoids, which can have a deleterious effect on the RPE (Cideciyan *et al.*, 2007). Using 2PE, these limitations are circumvented.

One of the most challenging aspects of fluorescence imaging is identifying fluorophores and their roles in biochemical processes. In the case of imaging retinal fluorescence with one-photon excitation, a great deal of effort has been made to identify potential dyes using FLIM methods (Dysli *et al.*, 2017). However, the acquired information from one-photon excitation fluorescence measurements does not include the data associated with endogenous fluorophores that are involved in the visual cycle (Delori *et al.*, 1995). With 2PEF imaging, this type of information can be obtained by shifting the excitation toward the ultraviolet, as shown with mice (Fig. 10). At this stage of 2PO development it is prohibitive to obtain high quality, spatially resolved FLIM data from human eyes *in vivo*. However, it is possible to perform spectral analysis of fluorescence signals from the eye by using spectral analysis

software. The result of imaging in five different spectral windows can be seen in Fig. 18 A, which is based on aligning and averaging over 1000 frames. A total of ten imaging sessions were performed over a period of several days at intervals of several days. In each of the five sessions, a set of five spectral filters was used. This study found that the majority of fluorescence signals were recorded in the spectral range above 500 nm, indicating that bisretinoids signals were dominant (Fig. 18 B). The spectral human data are consistent with those obtained from mouse models of Stargardt disease (Boguslawski *et al.*, 2022).

A study in 16 healthy volunteers was carried out to evaluate the feasibility of the use of 2PO imaging measurements in a clinical setting. It was found that even with the use of a laboratory device that was not optimized and prepared for routine use in patients, 2PEF signals could be obtained in all cases. Thus, once the method is modified further and the device is equipped with automatic measurement control systems, it will be possible to introduce the method into clinical practice.

5. Two-photon vision

A 2P absorption effect can be readily observed in chromophores when they are illuminated with high energy flux. Furthermore, despite the fact that the near-infrared radiation emitted by the sun reaches the Earth, only a portion of the radiation spectrum of the sun, extending from about 400 nm to 730 nm is actually considered to be visible to humans. There are evolutionary reasons for this restricted range, as it is related to the combination of the absorption spectra of the Earth's atmosphere and water (Rodieck, 1998). It was thus baffling whether visual pigments would respond to IR by 2P activation when illuminated with IR light (Fig. 19A). To answer this question a system for safe delivery of short-pulse IR light to the eye was designed and 2P vision was tested.

As early as the 1940s, Wald and his colleagues began exploring this topic in depth. In their study, they found that as wavelengths increase from ~500 nm, the relative spectral sensitivity decreases almost exponentially (Fig. 19B). And for 1000 nm wavelengths, the sensitivity is 12 orders of magnitude lower as compared with the peak sensitivity recorded around the wavelength maximum of 500 nm in the periphery (Griffin et al., 1947). In the spectral range 700 nm – 800 nm, the limit of traditional 1P vision, rod photoreceptors become more sensitive than cones (Fu and Yau, 2007). Pigments with a maximum wavelength of 700 nm or higher can also be excited but, because of the level of noise that is generated by spontaneous thermal activation, they are not practical (Luo et al., 2011). Accordingly, the criterion for the range of visible wavelengths for the eye is more a determinant of the ability to perceive color than it is of the light reception itself (Griffin et al., 1947).

Publications during the period 1960–2010 did not fully explain the mechanism responsible for the occurrence of human infrared vision (Dmitriev et al., 1979; Sliney et al., 1976; Walraven and Leebeek, 1963; Zaidi and Pokorny, 1988). A number of possible mechanisms have been suggested, including 2PEF absorption as well as SHG in the eye (Zaidi and Pokorny, 1988) (Masters and So, 2008).

5.1. Two-photon absorption is responsible for IR vision

These earlier reports about perceiving IR as visible light were intriguing. Thus, through detailed systematic studies, it was shown that the sensitivity of observing this effect increased with wavelengths above 900 nm and displayed a quadratic dependence on laser power, which indicated that a nonlinear optical process is at play (Palczewska et al., 2014c) (Fig. 19C). Two-photon vision (2P vision) is the name given to this phenomenon. Although different methods and light sources were used in these experiments, the results agreed with the Wald curve (Fig. 19B) for wavelengths shorter than 950 nm. It also turned out that for wavelengths shorter than 900 nm, one-photon excitation was dominant even when using very short 10^{-12} s (ps) pulses. However, for wavelengths longer than 1000 nm, NIR was perceived as light with color in a visible range. (Palczewska et al., 2014c). To study and test repeatability of the observed effect, the wavelength of visible radiation that was perceived by the subjects in response to IR stimulation was recorded in 30 volunteers. (Fig. 19C). In all subjects, IR light was perceived as visible with an impression of color. The wavelength changes of the IR-light stimuli correlated directly with the change in color perception. A linear function was fitted to the data, and it was found that the frequency doubling relationship, between visible light perception and IR stimulus wavelength, deviated for longer IR wavelengths (Fig 19C). Considering these data, and the fact that the rhodopsin fluorescence quantum yield is ~10^{-5}, as compared to its 0.6 quantum yield for isomerization, it was hypothesized that the photoreceptors additionally may respond to the weak fluorescence emitted by visual pigment with a maximum wavelength at 560 nm, consistent with findings by Walraven *et al* (Walraven and Leebeek, 1963).

Human psycho-physical studies of two-photon excitation-mediated vision were supported by measurements of the *ex vivo* transretinal electroretinogram (ERG) responses to pulsed IR in isolated retinas from mice and primates. In this configuration the impact of second harmonic (SH) generation in the sclera was excluded. Mouse rod responses were relatively easy to measure; however, smaller responses of mammalian cones, as compared to rods, required refinement of the specimen holder. A new device was designed and constructed to enable simultaneous imaging and electrophysiological recording *in situ* (Fig. 20A) (Vinberg *et al*., 2019). To minimize IR light-beam distortions, a thin 1.5 VWR coverslip was used to maintain a 0.2-mm layer above the retina of perfusion solution (Ames solution heated to 37ºC and continuously bubbled with carbogen (95% O_2 and 5% CO_2)). Using this holder and transretinal ERG recording, the sensitivity to different wavelengths was determined for rods in WT mice and cones in isolated retinas of macaque monkeys and in transducin-α-subunit-knockout *Gnat1*$^{-/-}$ mice (Fig. 20B). Furthermore, the WT mouse responses were clearly slower than those recorded from the *Gnat1*$^{-/-}$ mice and from macaque macula retina samples, indicating that the macaque recordings were dominated by cone photoreceptors. The WT rod data followed the predicted 1P spectral-sensitivity template accurately up to 800 nm, but for longer wavelengths the sensitivity started to increase. The *Gnat1*$^{-/-}$ mouse data demonstrated higher than expected sensitivities at wavelengths above 730 nm. Furthermore, transretinal ERG recordings were reduced by broadening the pulse duration, resulting from dispersion by the optical components of the system. The macaque data were fitted best by assuming a mixture of 85% M and 15% L pigments, and divergence from the 1P pigment template; namely, increases in responses were evident for wavelengths ≥

800 nm. These data confirmed that mouse cones and rods, and primate cones are responsive to short-pulse IR light *via* two-photon excitation of their visual pigments. The effect of IR pulse duration, energy and focal spot size on the ERG responses in live mice was also proposed by Gaulier and colleagues (Gaulier et al., 2022). This work showed how the nonlinear intensity dependence of the photon absorption process carries over to the amplitude of the ERG signals. The possibility of manipulating the spectral phase of IR pulses (Gaulier et al., 2021) and its effect on the predictable change in the two-photon-induced response under physiological excitation was also pointed out in this work.

Furthermore, biochemical experiments were performed, using the model chromophore 11-*cis*-retinyl-propylamine, crystalline rhodopsin, and rod and cone pigments. It was found that the rhodopsin crystal responded identically to irradiation with white light and 1000 nm IR. The 2P process resulted in the same reaction products as those produced under visible light; after incubation with 11-*cis*- or 9-*cis*-retinal, the green pigment and the rhodopsin were returned to their basal state, demonstrating no detrimental changes to the protein after exposure to IR. The photo-isomerization of the protonated 11-*cis*-retinal-propylamine Schiff base also yielded a similar distribution of retinoid isomers to that resulting from the visible light photo-isomerization.

As additional confirmation that the 2P isomerization of visual pigments is responsible for the 2P vision effect, hybrid quantum-mechanical calculations together with molecular dynamics simulations (QM/MM) were performed, to determine the energetics of rhodopsin activation by IR light (Palczewska et al., 2014c). Using quadratic time-dependent density functional theory (Salek *et al.*, 2003) to calculate the 2P absorption cross-section for rhodopsin, a maximum value for the cross section was determined to be at 950 nm. This result agrees with the data obtained from psychophysical experiments (Fig. 19C) and electrophysiological experiments (Fig. 20); and it supports the hypothesis that the simultaneous absorption of two low-energy photons induces an excited state that leads to the rapid *cis-trans* isomerization of the visual chromophore.

5.2. Applications of 2P vision

One way to research 2P vision in more detail is through subjective psychophysical testing. By comparing the sensitivity of 2P vision of IR light to that of visible light, researchers were able to detect similarities and differences between these two mechanisms of vision and thereby learn more about how they are related to each other. To study these two mechanisms, procedures similar to 1P microperimetry were used. The term microperimetry refers to the specific localization of the light stimulus on the fundus image (Crossland *et al.*, 2012). A perimetry examination is an essential part of ophthalmic diagnosis (Markowitz and Reyes, 2013), but it can also be used for conducting research in the field of vision science. The methods in common practice use visible light from 400 to 700 nm. However, one may be prompted to use the same methods for psychophysical testing of retinal function, using infrared light. Thus, a microperimeter for 2P vision was developed (Ruminski *et al.*, 2019; Zielinska *et al.*, 2019). In terms of diagnostic utility, 2P microperimetry has the potential to improve the diagnosis of age-related conditions. Transmission of IR is much less impaired than visible light in aging eyes suffering from increased optical opacities. Additionally, it

was hypothesized that 2PE can enhance the critical localization, as the 2P absorption effect occurs above a certain level of light intensity, so it is not impacted by secondary reflections within eye structures.

The system and results of several psychophysical tests including visual sensitivity-threshold values and a retinal preview of the SLO, with superimposition of the position of the macula probed with visible (VIS) and IR light are shown in Fig. 21. In addition, spatially interpolated contour maps of visual sensitivity for VIS and IR were generated (Fig. 21B). Ruminski *et al.* used a sub-picosecond laser as the source of the IR stimulus. Later, it was pointed out by Marzejon *et al.* that picosecond lasers could be used instead of femtosecond lasers for 2P vision experiments, which would drastically reduce the cost and complexity of future devices that employ this process (Marzejon *et al.*, 2021).

One of the findings demonstrated by Ruminski *et al.* was that 2P vision is mediated by both cones and rods (Ruminski *et al.*, 2019). In these experiments, one of the primary tests was to examine the spatial distribution of macular sensitivity under conditions of scotopic illumination. The visual thresholds for VIS and IR in forty-five locations were determined in a healthy volunteer, after a 30-min dark adaptation period. For both IR and VIS, the lowest visual sensitivity was in the cone-rich fovea, and the highest sensitivity in the rod-dominated locations farthest from the fovea (Fig. 21B). The most important finding, however, was that the differences in response between cones and rods in 2P vision were almost 10 times smaller than in 1P vision. These findings were supported by tracking recovery of 1P and 2P visual thresholds after exposure to bright light.

There was a quadratic relationship between the visual sensitivity thresholds to VIS and IR light, as measured for the same photoreceptors in psychophysical experiments using a 2P microperimeter. It was, therefore, possible to show that the process of 2P vision was a result of a nonlinear optical process, as shown in a log-log plot (Fig. 22A). The slopes of the curves for three individual test subjects all are in the range of 1.7–2, indicating that there was a near-squared relationship between the two variables. Manzanera *et al.* provided additional biophysical support for the hypothesis that IR vision is governed by a two-photon absorption mechanism (Manzanera et al., 2020) by using two different PRFs and by developing a corresponding theoretical model. Experimental analyses and calculations indicated that with such a parameterized experiment the only possible explanation for the phenomenon is a nonlinear absorption process. This result confirmed earlier work (Palczewska et al., 2014c).

The accuracy of localization of the stimulating light is another key property of the 2P vision system (Ruminski *et al.*, 2019). This fact was demonstrated through the use of a psychometric function to describe the relationship between the level of stimulus power and the level of response (the visual threshold, as described previously (Treutwein and Strasburger, 1999; Watson, 2017)). This observation led to the conclusion that the psychometric function of retinal stimulation with visible light is twice as wide as for IR vision measurements (Fig. 22B), which has the effect of halving the statistical spread of measurement points when IR light is used to stimulate the retina. Consequently, the accuracy of threshold determination for 2P vision is greatly improved. This last observation

leads directly to the hypothesis that the 2P perimetry method is more appropriate for distinguishing disease cases than classical perimetry.

This advantage was demonstrated in a study (Labuz *et al.*, 2020), where the mean IR sensitivity values as a function of age in a normal population were compared to groups of patients with AMD or diabetic retinopathy (Fig. 22C). In addition, these results showed that 2P microperimetry is less affected by lens opacity, as the measurement points of sensitivity thresholds for eyes with cataracts aligned similarly to those for healthy eyes, and separated clearly from AMD and diabetic retinopathy cases. Subsequent work has shown that the high accuracy of 2P microperimetry can offer an additional diagnostic parameter in conditions such as glaucomatous neuropathy (Labuz et al., 2022a; Zielinska et al., 2021), diabetic retinopathy (Labuz et al., 2021a), and AMD (Labuz et al., 2022b). A number of studies have confirmed that 2P microperimetry offers high-accuracy measurements (Labuz et al., 2022a; Zielinska et al., 2019) in diabetic retinopathy (Labuz et al., 2021b), and AMD (Labuz *et al.*, 2022b).

Several publications followed, with the purpose of comparing the results obtained by 2P microperimetry with conventional visual function tests among healthy subjects of different ages, both with and without simulated central opacification (Wei *et al.*, 2021). These studies showed that retinal sensitivity measured by 2P microperimetry had less variability than devices using stimuli in the visible spectrum. In addition, significant differences in test results between young and older patients were again indicated for instruments using visible light. As a further demonstration of the potential of 2P microperimetry, another study compared the results of the IR tests with conventional tests of visual function before and after cataract surgery for a patient with nuclear sclerotic brown cataracts and posterior sub-capsular cataracts (Mehta *et al.*, 2022). With IR stimulation, it was confirmed that the effects of opaque optical media were minimized, thus assisting in the early diagnosis of macular degeneration. However, it has been shown that despite the reduction in scattering of IR light in the eye and the presence of optical confinement, the use of two-photon vision has not improved spatial resolution (Artal *et al.*, 2017a; Artal *et al.*, 2017b). There was also a study published by Zielinska *et al.* that compared the responses of human pupils to two-photon infrared stimuli *versus* visible light stimuli (Zielinska *et al.*, 2021). The study showed that two-photon vision causes a weaker pupil response to stimuli of the same brightness, the same color, and the same spot size compared to one-photon vision. These are very important findings showing the differences in the mechanisms of one-photon and two-photon vision, which may point to potential applications of this phenomenon in the future.

6. Using two-photon excitation in crystallography X-ray crystallography can provide detailed, information about the sequence and spatial arrangements of individual amino acids of a protein structure. Insights obtained from such studies can elucidate the impact of gene mutations on protein misfolding that contribute to retinal degeneration and loss of sight, and consequently accelerate the development of drugs aimed at restoring or preserving eyesight. One example is understanding at the molecular level the mechanism of inhibition of the retinoid cycle by binding of the drug Emixustat to the RPE65 protein (Zhang et al., 2015b). Crystallographic studies often require thousands of screenings to find optimal conditions to grow protein crystals and thus may take years to complete. Typically, such

trials are evaluated using optical microscope equipped with crossed-polarizers to identify crystals by their birefringence. However, crystal-growing media could be opaque or exhibit birefringence as well; hence, an alternative technique for early identification of appropriate protein crystals was developed (Padayatti et al., 2012; Wampler et al., 2008). Irradiation with low-power IR combined with fluorescence and second harmonic imaging can be used to identify crystals as small as 10 μm, early in the crystallization phase. Furthermore, through a series of experiments a guideline was developed, correlating protein crystal systems with their TP fluorescence or SH signature (FIG. 23). Thus, most protein crystals could be imaged by a combination of 2PEF and SH detection.

7. Conclusions

The purpose of this review is to describe a new approach and associated technology for the assessment of retinal function based on a nonlinear excitation of visual pigments and retinal fluorophores in the retina *in vivo*. The review is based on a wealth of published data, obtained in the laboratories of the authors and their collaborators, culminating in the validation of its application in humans and implementation of new instruments for clinical practice (Boguslawski et al., 2022; Imanishi et al., 2004b; Imanishi et al., 2004c; Palczewska et al., 2014a; Palczewska et al., 2010; Palczewska et al., 2018). The transparency of the anterior segment of the eye provides a unique opportunity for identifying vital molecular events within the retina and the RPE. These molecular events can then serve as biomarkers for healthy versus diseased retinas. Non-invasive optical imaging not only can reveal these important molecular mechanisms, but also can help to accelerate the development of therapies against the blinding diseases. Furthermore, potentially blinding diseases need to be arrested before irreversible damage to retinal neurons has occurred, but detection of early disease onset has not been possible using current imaging technologies. Thus, there is a need for non-invasive imaging of the eye that can assess biochemical processes, so that the earliest changes in the retina can be detected before irreversible damage occurs, and then preventative therapy can be applied. Combining SLO and OCT can provide information about the size and approximate location of retinal lesions as well as their progression; but they cannot probe changes in retinoids and their derivatives during phototransduction and their transformation throughout the retinoid cycle. In contrast, 2PE ophthalmoscopy utilizing near IR light overcomes these obstacles. 2PE ophthalmoscopy can be used to excite endogenous fluorophores to detect aberrant biochemical events. Furthermore, 2PO coupled with FLIM and spectral-data collection offers a unique opportunity to construct 3D maps of the endogenous fluorophores within the retina and RPE, and determine how they change with environmental insult, disease, or therapy. Further refinement of high-resolution functional imaging techniques, such as employing artificial intelligence (AI) to data analyses will improve diagnostic capabilities in the clinic and accelerate the development of new treatments for blinding diseases

Acknowledgements

We would like to thank Akiko Maeda, Andrew Browne, Tadao Maeda, Yoshi Imanishi, Philip Kiser, Susie Suh, Marcin Golczak, Nathan Alexander, David Salom, Jianye Zhang, Zhiqian Dong, Jakub Bogusławski, Michał Dąbrowski, Kasia Komar, Patrycjusz Stremplewski, Sławomir Tomczewski, Marcin Marzejon, Lukasz Kornaszewski, Piotr Kasprzycki and Grzegorz Soboń, and numerous other collaborators for their support. Financial

support is acknowledged from the International Centre for Translational Eye Research (MAB/2019/12) project carried out within the International Research Agendas Programme of the Foundation for Polish Science co-financed by the European Union under the European Regional Development Fund. The authors also acknowledge financial support from the National Institutes of Health (NIH) to K.P. (EY009339, EY027283) and from a RPB unrestricted grant to the Department of Ophthalmology, University of California, Irvine.

Abbreviations:

1P	one-photon
1PEF	one-photon excited fluorescence
2P	two-photon
2PE	two-photon excitation
2PEF	two-photon excited fluorescence
2PI	two-photon isomerization
2PO	two-photon ophthalmoscope
11-*cis*-RAL	11-*cis*-retinal
Abca4$^{-/-}$Rdh8$^{-/-}$	double knockout mouse
A2E	diretinoid-pyridiniumethanolamine
all-*trans*-RAL	all-*trans*-retinal
all-*trans*-ROL	all-*trans*-retinol
AMD	age-related macular degeneration
FDA	Food and Drug Administration
FLIM	fluorescence lifetime imaging microscopy
IR	infrared
LRAT	lecithin:retinol acyltransferase
MIIPS	multiphoton intrapulse interference phase scan
NIR	near infrared
OCT	optical coherence tomography
PRF	pulse repetition frequency
RDH	retinol dehydrogenase
RPE	retinal pigment epithelium
RPE65	retinoid isomerase
SHG	second harmonic generation

SLO	scanning laser ophthalmoscopy
VEGF	vascular endothelial growth factor
WT	wild-type

12. References

Alexander NS, Palczewska G, Stremplewski P, Wojtkowski M, Kern TS, Palczewski K, 2016. Image registration and averaging of low laser power two-photon fluorescence images of mouse retina. Biomed Opt Express 7, 2671–2691. [PubMed: 27446697]

Allikmets R, Singh N, Sun H, Shroyer NF, Hutchinson A, Chidambaram A, Gerrard B, Baird L, Stauffer D, Peiffer A, Rattner A, Smallwood P, Li Y, Anderson KL, Lewis RA, Nathans J, Leppert M, Dean M, Lupski JR, 1997. A photoreceptor cell-specific ATP-binding transporter gene (ABCR) is mutated in recessive Stargardt macular dystrophy. Nat. Genet. 15, 236–246. [PubMed: 9054934]

Amoaku W, Blakeney S, Freeman M, Gale R, Johnston R, Kelly SP, McLaughlan B, Sahu D, Varma D, Action on AMDG, 2012. Action on AMD. Optimising patient management: act now to ensure current and continual delivery of best possible patient care. Eye (Lond) 26 Suppl 1, S2–21. [PubMed: 22302094]

Andrews JS, Futterman S, 1964. Metabolism of the Retina. V. The Role of Microsomes in Vitamin a Esterification in the Visual Cycle. J. Biol. Chem. 239, 4073–4076. [PubMed: 14247650]

Artal P, Manzanera S, Komar K, Gambin-Regadera A, Wojtkowski M, 2017a. Visual acuity in two-photon infrared vision. Optica 4, 1488–1491.

Artal P, Manzanera S, Komar K, Gambin A, Wojtkowski M, 2017b. Visual acuity and optical resolution in two-photon infrared vision. Invest Ophth Vis Sci 58.

Artunay O, Rasier R, Yuzbasioglu E, Sengul A, Bahcecioglu H, 2009. Intravitreal bevacizumab injection in patients with choroidal neovascularization due to choroid rupture after blunt-head trauma. Int. Ophthalmol. 29, 289–291. [PubMed: 18825317]

Batten ML, Imanishi Y, Maeda T, Tu DC, Moise AR, Bronson D, Possin D, Van Gelder RN, Baehr W, Palczewski K, 2004. Lecithin-retinol acyltransferase is essential for accumulation of all-trans-retinyl esters in the eye and in the liver. J. Biol. Chem. 279, 10422–10432. [PubMed: 14684738]

Batten ML, Imanishi Y, Tu DC, Doan T, Zhu L, Pang J, Glushakova L, Moise AR, Baehr W, Van Gelder RN, Hauswirth WW, Rieke F, Palczewski K, 2005. Pharmacological and rAAV gene therapy rescue of visual functions in a blind mouse model of Leber congenital amaurosis. Plos Med 2, e333. [PubMed: 16250670]

Betzig E, Patterson GH, Sougrat R, Lindwasser OW, Olenych S, Bonifacino JS, Davidson MW, Lippincott-Schwartz J, Hess HF, 2006. Imaging intracellular fluorescent proteins at nanometer resolution. Science 313, 1642–1645. [PubMed: 16902090]

Biss DP, Sumorok D, Burns SA, Webb RH, Zhou YP, Bifano TG, Cote D, Veilleux I, Zamiri P, Lin CP, 2007. In vivo fluorescent imaging of the mouse retina using adaptive optics. Opt. Lett. 32, 659–661. [PubMed: 17308593]

Blum E, Zhang J, Zaluski J, Einstein DE, Korshin EE, Kubas A, Gruzman A, Tochtrop GP, Kiser PD, Palczewski K, 2021. Rational Alteration of Pharmacokinetics of Chiral Fluorinated and Deuterated Derivatives of Emixustat for Retinal Therapy. J Med Chem 64, 8287–8302. [PubMed: 34081480]

Blumenkranz MS, Haller JA, Kuppermann BD, Williams GA, Ip M, Davis M, Weinberg DV, Chou C, Whitcup SM, 2010. Correlation of visual acuity and macular thickness measured by optical coherence tomography in patients with persistent macular edema. Retina 30, 1090–1094. [PubMed: 20616686]

Boettner EA, Wolter JR, 1962. Transmission of the Ocular Media. Invest. Ophthalmol. 1, 776–783.

Boguslawski J, Palczewska G, Tomczewski S, Milkiewicz J, Kasprzycki P, Stachowiak D, Komar K, Marzejon MJ, Sikorski BL, Hudzikowski A, Gluszek A, Laszczych Z, Karnowski K, Sobon G, Palczewski K, Wojtkowski M, 2022. In vivo imaging of the human eye using a 2-photon-excited fluorescence scanning laser ophthalmoscope. J. Clin. Invest. 132.

Chen Y, Okano K, Maeda T, Chauhan V, Golczak M, Maeda A, Palczewski K, 2012. Mechanism of all-trans-retinal toxicity with implications for stargardt disease and age-related macular degeneration. J. Biol. Chem. 287, 5059–5069. [PubMed: 22184108]

Chen Y, Palczewska G, Mustafi D, Golczak M, Dong Z, Sawada O, Maeda T, Maeda A, Palczewski K, 2013. Systems pharmacology identifies drug targets for Stargardt disease-associated retinal degeneration. J. Clin. Invest. 123, 5119–5134. [PubMed: 24231350]

Cheung CMG, Arnold JJ, Holz FG, Park KH, Lai TYY, Larsen M, Mitchell P, Ohno-Matsui K, Chen SJ, Wolf S, Wong TY, 2017. Myopic Choroidal Neovascularization: Review, Guidance, and Consensus Statement on Management. Ophthalmology 124, 1690–1711. [PubMed: 28655539]

Cideciyan AV, Swider M, Aleman TS, Roman MI, Sumaroka A, Schwartz SB, Stone EM, Jacobson SG, 2007. Reduced-illuminance autofluorescence imaging in ABCA4-associated retinal degenerations. J. Opt. Soc. Am. A Opt. Image Sci. Vis. 24, 1457–1467. [PubMed: 17429493]

Cideciyan AV, Swider M, Jacobson SG, 2015. Autofluorescence imaging with near-infrared excitation:normalization by reflectance to reduce signal from choroidal fluorophores. Invest Ophthalmol Vis Sci 56, 3393–3406. [PubMed: 26024124]

Croce AC, Bottiroli G, 2014. Autofluorescence spectroscopy and imaging: a tool for biomedical research and diagnosis. Eur. J. Histochem. 58, 2461. [PubMed: 25578980]

Crossland M, Jackson M-L, Seibel WH, 2012. Microperimetry: a review of fundus related perimetry. Optometry Rep. 2, 2.

Cua M, Wahl DJ, Zhao Y, Lee S, Bonora S, Zawadzki RJ, Jian Y, Sarunic MV, 2016. Coherence-Gated Sensorless Adaptive Optics Multiphoton Retinal Imaging. Sci Rep 6, 32223. [PubMed: 27599635]

Delori FC, Dorey CK, Staurenghi G, Arend O, Goger DG, Weiter JJ, 1995. In vivo fluorescence of the ocular fundus exhibits retinal pigment epithelium lipofuscin characteristics. Invest Ophthalmol Vis Sci 36, 718–729. [PubMed: 7890502]

Delori FC, Webb RH, Sliney DH, American National Standards I, 2007. Maximum permissible exposures for ocular safety (ANSI 2000), with emphasis on ophthalmic devices. J. Opt. Soc. Am. A Opt. Image Sci. Vis. 24, 1250–1265. [PubMed: 17429471]

Denk W, Strickler JH, Webb WW, 1990. Two-photon laser scanning fluorescence microscopy. Science 248, 73–76. [PubMed: 2321027]

Diabetic Retinopathy Clinical Research N, Wells JA, Glassman AR, Ayala AR, Jampol LM, Aiello LP, Antoszyk AN, Arnold-Bush B, Baker CW, Bressler NM, Browning DJ, Elman MJ, Ferris FL, Friedman SM, Melia M, Pieramici DJ, Sun JK, Beck RW, 2015. Aflibercept, bevacizumab, or ranibizumab for diabetic macular edema. N. Engl. J. Med. 372, 1193–1203. [PubMed: 25692915]

Diaspro A, Bianchini P, Vicidomini G, Faretta M, Ramoino P, Usai C, 2006. Multi-photon excitation microscopy. Biomed. Eng. Online 5, 36. [PubMed: 16756664]

Dmitriev VG, Emel'yanov V, Kashintsev M, Kulikov V, Solov'ev A, Stel'makh M, Cherednichenko OB, 1979. Nonlinear perception of infrared radiation in the 800–1355 nm range with human eye. Sov. J. Quantum Electron. 9, 475.479.

Donnelly WJ, Roorda A, 2003. Optimal pupil size in the human eye for axial resolution. Journal of the Optical Society of America a-Optics Image Science and Vision 20, 2010–2015. [PubMed: 14620328]

Dowling JE, 1960. Chemistry of visual adaptation in the rat. Nature 188, 114–118. [PubMed: 13724150]

Duncan JL, LaVail MM, Yasumura D, Matthes MT, Yang HD, Trautmann N, Chappelow AV, Feng W, Earp HS, Matsushima GK, Vollrath D, 2003. An RCS-like retinal dystrophy phenotype in Mer knockout mice. Invest Ophth Vis Sci 44, 826–838.

Dysli C, Wolf S, Berezin MY, Sauer L, Hammer M, Zinkernagel MS, 2017. Fluorescence lifetime imaging ophthalmoscopy. Prog Retin Eye Res 60, 120–143. [PubMed: 28673870]

Entenberg D, Wyckoff J, Gligorijevic B, Roussos ET, Verkhusha VV, Pollard JW, Condeelis J, 2011. Setup and use of a two-laser multiphoton microscope for multichannel intravital fluorescence imaging. Nat. Protoc. 6, 1500–1520. [PubMed: 21959234]

Fereidouni F, Bader AN, Gerritsen HC, 2012. Spectral phasor analysis allows rapid and reliable unmixing of fluorescence microscopy spectral images. Opt. Express 20, 12729–12741. [PubMed: 22714302]

Ferrara N, Adamis AP, 2016. Ten years of anti-vascular endothelial growth factor therapy. Nat. Rev. Drug Discov. 15, 385–403. [PubMed: 26775688]

Fogli S, Del Re M, Rofi E, Posarelli C, Figus M, Danesi R, 2018. Clinical pharmacology of intravitreal anti-VEGF drugs. Eye (Lond) 32, 1010–1020. [PubMed: 29398697]

Fu Y, Yau KW, 2007. Phototransduction in mouse rods and cones. Pflugers Arch. 454, 805–819. [PubMed: 17226052]

Gal A, Li Y, Thompson DA, Weir J, Orth U, Jacobson SG, Apfelstedt-Sylla E, Vollrath D, 2000. Mutations in MERTK, the human orthologue of the RCS rat retinal dystrophy gene, cause retinitis pigmentosa. Nat. Genet. 26, 270–271. [PubMed: 11062461]

Garcia-Quintanilla L, Luaces-Rodriguez A, Gil-Martinez M, Mondelo-Garcia C, Maronas O, Mangas-Sanjuan V, Gonzalez-Barcia M, Zarra-Ferro I, Aguiar P, Otero-Espinar FJ, Fernandez-Ferreiro A, 2019. Pharmacokinetics of Intravitreal Anti-VEGF Drugs in Age-Related Macular Degeneration. Pharmaceutics 11.

Garwin GG, Saari JC, 2000. High-performance liquid chromatography analysis of visual cycle retinoids. Methods Enzymol 316, 313–324. [PubMed: 10800683]

Gaulier G, Dietschi Q, Bhattacharyya S, Schmidt C, Montagnese M, Chauvet A, Hermelin S, Chiodini F, Bonacina L, Herrera PL, Rothlisberger U, Rodriguez I, Wolf JP, 2021. Ultrafast pulse shaping modulates perceived visual brightness in living animals. Science Advances 7.

Gaulier G, Dietschi Q, Djorovic A, La Volpe L, Rodrigues T, Bonacina L, Rodriguez I, Wolf JP, 2022. Control of the Two-photon Visual Process in ex vivo Retinas and in Living Mice. Chimia 76, 570–574.

Geng Y, Dubra A, Yin L, Merigan WH, Sharma R, Libby RT, Williams DR, 2012. Adaptive optics retinal imaging in the living mouse eye. Biomedical Optics Express 3, 715–734. [PubMed: 22574260]

Goeppert-Mayer M, 1931. Über Elementarakte mit zwei Quantensprüngen. Annals of Physics 9, 273–295.

Golczak M, Kuksa V, Maeda T, Moise AR, Palczewski K, 2005. Positively charged retinoids are potent and selective inhibitors of the trans-cis isomerization in the retinoid (visual) cycle. Proc Natl Acad Sci U S A 102, 8162–8167. [PubMed: 15917330]

Golczak M, Sears AE, Kiser PD, Palczewski K, 2015. LRAT-specific domain facilitates vitamin A metabolism by domain swapping in HRASLS3. Nat Chem Biol 11, 26–32. [PubMed: 25383759]

Golfetto O, Hinde E, Gratton E, 2015a. The Laurdan Spectral Phasor Method to Explore Membrane Micro-heterogeneity and Lipid Domains in Live Cells. Methods in Membrane Lipids, Second Edition 1232, 273–290.

Golfetto O, Hinde E, Gratton E, 2015b. The Laurdan spectral phasor method to explore membrane micro-heterogeneity and lipid domains in live cells. Methods Mol Biol 1232, 273–290. [PubMed: 25331141]

Griffin DR, Hubbard R, Wald G, 1947. The sensitivity of the human eye to infra-red radiation. J. Opt. Soc. Am. 37, 546–554. [PubMed: 20256359]

Gulati N, Forooghian F, Lieberman R, Jabs DA, 2011. Vascular endothelial growth factor inhibition in uveitis: a systematic review. Br. J. Ophthalmol. 95, 162–165. [PubMed: 20494915]

Hell SW, Wichmann J, 1994. Breaking the diffraction resolution limit by stimulated emission: stimulated-emission-depletion fluorescence microscopy. Opt. Lett. 19, 780–782. [PubMed: 19844443]

Hillmann D, Spahr H, Pfaffle C, Sudkamp H, Franke G, Huttmann G, 2016. In vivo optical imaging of physiological responses to photostimulation in human photoreceptors. Proc Natl Acad Sci U S A 113, 13138–13143. [PubMed: 27729536]

Hong JD, Salom D, Kochman MA, Kubas A, Kiser PD, Palczewski K, 2022. Chromophore hydrolysis and release from photoactivated rhodopsin in native membranes. Proc Natl Acad Sci U S A 119, e2213911119. [PubMed: 36322748]

Hubbard R, Wald G, 1952. Cis-trans isomers of vitamin A and retinene in the rhodopsin system. J. Gen. Physiol. 36, 269–315. [PubMed: 13011282]

Hunter JJ, Masella B, Dubra A, Sharma R, Yin L, Merigan WH, Palczewska G, Palczewski K, Williams DR, 2010. Images of photoreceptors in living primate eyes using adaptive optics two-photon ophthalmoscopy. Biomed Opt Express 2, 139–148. [PubMed: 21326644]

Hurley JB, 2021. Retina Metabolism and Metabolism in the Pigmented Epithelium: A Busy Intersection. Annu Rev Vis Sci 7, 665–692. [PubMed: 34102066]

Imanishi Y, Baehr W, Palczewski K, 2004a. Two-photon imaging of vitamin A in the eye: identification of retinosomes. Invest Ophth Vis Sci 45, U475–U475.

Imanishi Y, Batten ML, Piston DW, Baehr W, Palczewski K, 2004b. Noninvasive two-photon imaging reveals retinyl ester storage structures in the eye. J Cell Biol 164, 373–383. [PubMed: 14745001]

Imanishi Y, Gerke V, Palczewski K, 2004c. Retinosomes: new insights into intracellular managing of hydrophobic substances in lipid bodies. J Cell Biol 166, 447–453. [PubMed: 15314061]

Imanishi Y, Palczewski K, 2010. Visualization of retinoid storage and trafficking by two-photon microscopy. Methods Mol Biol 652, 247–261. [PubMed: 20552433]

Jacobson SG, Aleman TS, Cideciyan AV, Heon E, Golczak M, Beltran WA, Sumaroka A, Schwartz SB, Roman AJ, Windsor EA, Wilson JM, Aguirre GD, Stone EM, Palczewski K, 2007. Human cone photoreceptor dependence on RPE65 isomerase. Proc Natl Acad Sci U S A 104, 15123–15128. [PubMed: 17848510]

Jaffe GJ, Yang CH, Guo H, Denny JP, Lima C, Ashton P, 2000. Safety and pharmacokinetics of an intraocular fluocinolone acetonide sustained delivery device. Invest. Ophthalmol. Vis. Sci. 41, 3569–3575. [PubMed: 11006254]

Jin M, Li S, Moghrabi WN, Sun H, Travis GH, 2005. Rpe65 is the retinoid isomerase in bovine retinal pigment epithelium. Cell 122, 449–459. [PubMed: 16096063]

Jonnal RS, 2021. Toward a clinical optoretinogram: a review of noninvasive, optical tests of retinal neural function. Ann Transl Med 9, 1270. [PubMed: 34532407]

Kiser PD, Golczak M, Palczewski K, 2014. Chemistry of the retinoid (visual) cycle. Chem Rev 114, 194–232. [PubMed: 23905688]

Kiser PD, Palczewski K, 2021. Pathways and disease-causing alterations in visual chromophore production for vertebrate vision. J. Biol. Chem. 296, 100072. [PubMed: 33187985]

Kolesnikov A, Tang P, Maeda A, Byrne L, Flannery J, Palczewski K, Kefalov V, 2013. Mouse Cone Dark Adaptation Relies on Two Visual Cycles and Is Substantially Retarded in Mice Lacking RDH8 and ABCA4. Invest Ophth Vis Sci 54.

Kolesnikov AV, Maeda A, Tang PH, Imanishi Y, Palczewski K, Kefalov VJ, 2015. Essential Roles of RDH8, ABCA4, and Rods in Modulating Dark Adaptation of Mammalian Cones. Invest Ophth Vis Sci 56.

Kovach JL, Schwartz SG, Flynn HW Jr., Scott IU, 2012. Anti-VEGF Treatment Strategies for Wet AMD. J Ophthalmol 2012, 786870. [PubMed: 22523653]

Labuz G, Rayamajhi A, Khoramnia R, Palczewska G, Palczewski K, Holschbach A, Auffarth GU, 2021a. The loss of infrared light sensitivity of photoreceptor cells measured with two-photon excitation as an indicator of diabetic retinopathy. A Pilot Study. Retina 41, 1302–1308. [PubMed: 33323904]

Labuz G, Rayamajhi A, Khoramnia R, Palczewska G, Palczewski K, Holschbach A, Auffarth GU, 2021b. THE LOSS OF INFRARED LIGHT SENSITIVITY OF PHOTORECEPTOR CELLS MEASURED WITH TWO-PHOTON EXCITATION AS AN INDICATOR OF DIABETIC RETINOPATHY: A Pilot Study. Retina 41, 1302–1308. [PubMed: 33323904]

Labuz G, Rayamajhi A, Komar K, Khoramnia R, Auffarth GU, 2022a. Infrared- and white-light retinal sensitivity in glaucomatous neuropathy. Sci Rep 12, 1961. [PubMed: 35121766]

Labuz G, Rayamajhi A, Usinger J, Komar K, Merz P, Khoramnia R, Palczewska G, Palczewski K, Auffarth GU, 2020. Clinical Application of Infrared-Light Microperimetry in the Assessment of Scotopic-Eye Sensitivity. Transl Vis Sci Technol 9, 7.

Labuz G, Zielinska A, Kessler LJ, Rayamajhi A, Komar K, Khoramnia R, Auffarth GU, 2022b. Two-photon vision in age-related macular degeneration: A translational study. Diagnostics (Basel) 12.

Lakowicz JR, Szmacinski H, Nowaczyk K, Johnson ML, 1992. Fluorescence lifetime imaging of free and protein-bound NADH. Proc. Natl. Acad. Sci. U. S. A. 89, 1271–1275. [PubMed: 1741380]

Law AL, Parinot C, Chatagnon J, Gravez B, Sahel JA, Bhattacharya SS, Nandrot EF, 2015. Cleavage of Mer tyrosine kinase (MerTK) from the cell surface contributes to the regulation of retinal phagocytosis. J. Biol. Chem. 290, 4941–4952. [PubMed: 25538233]

Lin B, McLelland BT, Aramant RB, Thomas BB, Nistor G, Keirstead HS, Seiler MJ, 2020. Retina Organoid Transplants Develop Photoreceptors and Improve Visual Function in RCS Rats With RPE Dysfunction. Invest Ophthalmol Vis Sci 61, 34.

Luo DG, Yue WW, Ala-Laurila P, Yau KW, 2011. Activation of visual pigments by light and heat. Science 332, 1307–1312. [PubMed: 21659602]

Maeda A, Golczak M, Chen Y, Okano K, Kohno H, Shiose S, Ishikawa K, Harte W, Palczewska G, Maeda T, Palczewski K, 2011. Primary amines protect against retinal degeneration in mouse models of retinopathies. Nat Chem Biol 8, 170–178. [PubMed: 22198730]

Maeda A, Golczak M, Maeda T, Palczewski K, 2009a. Limited roles of Rdh8, Rdh12, and Abca4 in all-trans-retinal clearance in mouse retina. Invest Ophthalmol Vis Sci 50, 5435–5443. [PubMed: 19553623]

Maeda A, Maeda T, Golczak M, Chou S, Desai A, Hoppel CL, Matsuyama S, Palczewski K, 2009b. Involvement of all-trans-retinal in acute light-induced retinopathy of mice. J. Biol. Chem. 284, 15173–15183. [PubMed: 19304658]

Maeda A, Maeda T, Golczak M, Palczewski K, 2008. Retinopathy in mice induced by disrupted all-trans-retinal clearance. J. Biol. Chem. 283, 26684–26693. [PubMed: 18658157]

Maeda A, Palczewska G, Golczak M, Kohno H, Dong Z, Maeda T, Palczewski K, 2014. Two-photon microscopy reveals early rod photoreceptor cell damage in light-exposed mutant mice. Proc Natl Acad Sci U S A 111, E1428–1437. [PubMed: 24706832]

Maeda T, Lee MJ, Palczewska G, Marsili S, Tesar PJ, Palczewski K, Takahashi M, Maeda A, 2013. Retinal pigmented epithelial cells obtained from human induced pluripotent stem cells possess functional visual cycle enzymes in vitro and in vivo. J. Biol. Chem. 288, 34484–34493. [PubMed: 24129572]

Malacrida L, Astrada S, Briva A, Bollati-Fogolin M, Gratton E, Bagatolli LA, 2016. Spectral phasor analysis of LAURDAN fluorescence in live A549 lung cells to study the hydration and time evolution of intracellular lamellar body-like structures. Bba-Biomembranes 1858, 2625–2635. [PubMed: 27480804]

Malacrida L, Ranjit S, Jameson DM, Gratton E, 2021. The Phasor Plot: A Universal Circle to Advance Fluorescence Lifetime Analysis and Interpretation. Annu Rev Biophys 50, 575–593. [PubMed: 33957055]

Manzanera S, Sola D, Khalifa N, Artal P, 2020. Vision with pulsed infrared light is mediated by nonlinear optical processes. Biomedical Optics Express 11, 5603–5617. [PubMed: 33149974]

Markowitz SN, Reyes SV, 2013. Microperimetry and clinical practice: an evidence-based review. Canadian Journal of Ophthalmology-Journal Canadien D Ophtalmologie 48, 350–357. [PubMed: 24093179]

Martin DF, Kuppermann BD, Wolitz RA, Palestine AG, Li H, Robinson CA, 1999. Oral ganciclovir for patients with cytomegalovirus retinitis treated with a ganciclovir implant. Roche Ganciclovir Study Group. N. Engl. J. Med. 340, 1063–1070. [PubMed: 10194235]

Marzejon MJ, Kornaszewski L, Boguslawski J, Ciacka P, Martynow M, Palczewska G, Mackowski S, Palczewski K, Wojtkowski M, Komar K, 2021. Two-photon microperimetry with picosecond pulses. Biomed Opt Express 12, 462–479. [PubMed: 33659083]

Masters BR, So PTC, 2008. Handbook of biomedical nonlinear optical microscopy. Oxford University Press, New York.

McBee JK, Palczewski K, Baehr W, Pepperberg DR, 2001. Confronting complexity: the interlink of phototransduction and retinoid metabolism in the vertebrate retina. Prog Retin Eye Res 20, 469–529. [PubMed: 11390257]

Mehta U, Palczewska G, Lin KY, Browne AW, 2022. Seeing invisible light: 2-photon microperimetry to measure visual function. Am J Ophthalmol Case Rep 28, 101724. [PubMed: 36324628]

Meyer JH, Cunea A, Licha K, Welker P, Sonntag-Bensch D, Wafula P, Dernedde J, Fimmers R, Holz FG, Schmitz-Valckenberg S, 2016. In Vivo Imaging of Fluorescent Probes Linked to Antibodies

Against Human and Rat Vascular Endothelial Growth Factor. Invest. Ophthalmol. Vis. Sci. 57, 759–770. [PubMed: 26927569]

Moerner WE, 2006. Single-molecule mountains yield nanoscale cell images. Nat. Methods 3, 781–782. [PubMed: 16990808]

Moiseyev G, Chen Y, Takahashi Y, Wu BX, Ma JX, 2005. RPE65 is the isomerohydrolase in the retinoid visual cycle. Proc. Natl. Acad. Sci. U. S. A. 102, 12413–12418. [PubMed: 16116091]

Morales E, Moliz C, Gutierrez E, 2017. Renal damage associated to intravitreal administration of ranibizumab. Nefrologia 37, 653–655. [PubMed: 29122213]

O'Connor DV, Phillips D, 1984. Time-correlated single photon counting. Academic Press, London; Orlando.

Orban T, Palczewska G, Palczewski K, 2011. Retinyl ester storage particles (retinosomes) from the retinal pigmented epithelium resemble lipid droplets in other tissues. J. Biol. Chem. 286, 17248–17258. [PubMed: 21454509]

Organisciak DT, Darrow RM, Darrow RA, Lininger LA, 1998. Environmental light and age-related changes in retinal proteins. Photostasis and Related Phenomena, 79–92.

Padayatti P, Palczewska G, Sun W, Palczewski K, Salom D, 2012. Imaging of protein crystals with two-photon microscopy. Biochemistry-Us 51, 1625–1637.

Palczewska G, Boguslawski J, Stremplewski P, Kornaszewski L, Zhang J, Dong Z, Liang XX, Gratton E, Vogel A, Wojtkowski M, Palczewski K, 2020. Noninvasive two-photon optical biopsy of retinal fluorophores. Proc Natl Acad Sci U S A 117, 22532–22543. [PubMed: 32848058]

Palczewska G, Dong Z, Golczak M, Hunter JJ, Williams DR, Alexander NS, Palczewski K, 2014a. Noninvasive two-photon microscopy imaging of mouse retina and retinal pigment epithelium through the pupil of the eye. Nat Med 20, 785–789. [PubMed: 24952647]

Palczewska G, Golczak M, Williams DR, Hunter JJ, Palczewski K, 2014b. Endogenous fluorophores enable two-photon imaging of the primate eye. Invest Ophthalmol Vis Sci 55, 4438–4447. [PubMed: 24970255]

Palczewska G, Maeda A, Golczak M, Arai E, Dong Z, Perusek L, Kevany B, Palczewski K, 2016. Receptor MER Tyrosine Kinase Proto-oncogene (MERTK) Is Not Required for Transfer of Bis-retinoids to the Retinal Pigmented Epithelium. J. Biol. Chem. 291, 26937–26949. [PubMed: 27875314]

Palczewska G, Maeda T, Imanishi Y, Sun W, Chen Y, Williams DR, Piston DW, Maeda A, Palczewski K, 2010. Noninvasive multiphoton fluorescence microscopy resolves retinol and retinal condensation products in mouse eyes. Nat Med 16, 1444–1449. [PubMed: 21076393]

Palczewska G, Stremplewski P, Suh S, Alexander N, Salom D, Dong Z, Ruminski D, Choi EH, Sears AE, Kern TS, Wojtkowski M, Palczewski K, 2018. Two-photon imaging of the mammalian retina with ultrafast pulsing laser. JCI Insight 3.

Palczewska G, Vinberg F, Stremplewski P, Bircher MP, Salom D, Komar K, Zhang J, Cascella M, Wojtkowski M, Kefalov VJ, Palczewski K, 2014c. Human infrared vision is triggered by two-photon chromophore isomerization. Proc Natl Acad Sci U S A 111, E5445–5454. [PubMed: 25453064]

Palczewski K, 2006. G protein-coupled receptor rhodopsin. Annu Rev Biochem 75, 743–767. [PubMed: 16756510]

Palczewski K, Kiser PD, 2020. Shedding new light on the generation of the visual chromophore. Proc Natl Acad Sci U S A 117, 19629–19638. [PubMed: 32759209]

Pandiyan VP, Maloney-Bertelli A, Kuchenbecker JA, Boyle KC, Ling T, Chen ZC, Park BH, Roorda A, Palanker D, Sabesan R, 2020. The optoretinogram reveals the primary steps of phototransduction in the living human eye. Sci Adv 6.

Pang S, Yeh AT, Wang C, Meissner KE, 2009. Beyond the 1/T-p limit: two-photon-excited fluorescence using pulses as short as sub-10-fs. J. Biomed. Opt. 14.

Pe'er J, Folberg R, Itin A, Gnessin H, Hemo I, Keshet E, 1998. Vascular endothelial growth factor upregulation in human central retinal vein occlusion. Ophthalmology 105, 412–416. [PubMed: 9499769]

Rahim MK, Zhao JH, Patel HV, Lagouros HA, Kota R, Fernandez I, Gratton E, Haun JB, 2022. Phasor Analysis of Fluorescence Lifetime Enables Quantitative Multiplexed Molecular Imaging of Three Probes. Anal. Chem. 94, 14185–14194. [PubMed: 36190014]

Redmond TM, Poliakov E, Yu S, Tsai JY, Lu Z, Gentleman S, 2005. Mutation of key residues of RPE65 abolishes its enzymatic role as isomerohydrolase in the visual cycle. Proc. Natl. Acad. Sci. U. S. A. 102, 13658–13663. [PubMed: 16150724]

Redmond TM, Yu S, Lee E, Bok D, Hamasaki D, Chen N, Goletz P, Ma JX, Crouch RK, Pfeifer K, 1998. Rpe65 is necessary for production of 11-cis-vitamin A in the retinal visual cycle. Nat. Genet. 20, 344–351. [PubMed: 9843205]

Rodieck RW, 1998. The first steps in seeing. Sinauer Associates, Sunderland, Mass.

Rosenfeld PJ, Schwartz SD, Blumenkranz MS, Miller JW, Haller JA, Reimann JD, Greene WL, Shams N, 2005. Maximum tolerated dose of a humanized anti-vascular endothelial growth factor antibody fragment for treating neovascular age-related macular degeneration. Ophthalmology 112, 1048–1053. [PubMed: 15885778]

Rossi EA, Rangel-Fonseca P, Parkins K, Fischer W, Latchney LR, Folwell MA, Williams DR, Dubra A, Chung MM, 2013. In vivo imaging of retinal pigment epithelium cells in age related macular degeneration. Biomed Opt Express 4, 2527–2539. [PubMed: 24298413]

Ruiz A, Winston A, Lim YH, Gilbert BA, Rando RR, Bok D, 1999. Molecular and biochemical characterization of lecithin retinol acyltransferase. J. Biol. Chem. 274, 3834–3841. [PubMed: 9920938]

Ruminski D, Palczewska G, Nowakowski M, Zielinska A, Kefalov VJ, Komar K, Palczewski K, Wojtkowski M, 2019. Two-photon microperimetry: sensitivity of human photoreceptors to infrared light. Biomed Opt Express 10, 4551–4567. [PubMed: 31565509]

Salek P, Vahtras O, Guo JD, Luo Y, Helgaker T, Agren H, 2003. Calculations of two-photon absorption cross sections by means of density-functional theory. Chem. Phys. Lett. 374, 446–452.

Sauer L, Andersen KM, Dysli C, Zinkernagel MS, Bernstein PS, Hammer M, 2018. Review of clinical approaches in fluorescence lifetime imaging ophthalmoscopy (Erratum). J. Biomed. Opt. 23, 1.

Sauer L, Komanski CB, Vitale AS, Hansen ED, Bernstein PS, 2019. Fluorescence Lifetime Imaging Ophthalmoscopy (FLIO) in Eyes With Pigment Epithelial Detachments Due to Age-Related Macular Degeneration. Invest. Ophthalmol. Vis. Sci. 60, 3054–3063. [PubMed: 31348823]

Schweitzer D, Haueisen J, Brauer JL, Hammer M, Klemm M, 2020. Comparison of algorithms to suppress artifacts from the natural lens in fluorescence lifetime imaging ophthalmoscopy (FLIO). Biomed Opt Express 11, 5586–5602. [PubMed: 33149973]

Schweitzer D, Schenke S, Hammer M, Schweitzer F, Jentsch S, Birckner E, Becker W, Bergmann A, 2007. Towards metabolic mapping of the human retina. Microsc. Res. Tech. 70, 410–419. [PubMed: 17393496]

Semeraro F, Morescalchi F, Duse S, Parmeggiani F, Gambicorti E, Costagliola C, 2013a. Aflibercept in wet AMD: specific role and optimal use. Drug Des. Devel. Ther. 7, 711–722.

Semeraro F, Morescalchi F, Duse S, Parmeggiani F, Gambicorti E, Costagliola C, 2013b. Aflibercept in wet AMD: specific role and optimal use. Drug Des Dev Ther 7, 711–722.

Shiose S, Okano K, Maeda T, Tang J, Palczewski K, Maeda A, 2010. Role of Toll-Like Receptor 3 in Retinal Pigment Epithelial Cell Death in Rdh8−/−Abca4−/− Mice. Invest Ophth Vis Sci 51.

Sliney DH, Wangemann RT, Franks JK, Wolbarsht ML, 1976. Visual sensitivity of the eye to infrared laser radiation. J. Opt. Soc. Am. 66, 339–341. [PubMed: 1262982]

Sparrow JR, Fishkin N, Zhou J, Cai B, Jang YP, Krane S, Itagaki Y, Nakanishi K, 2003. A2E, a byproduct of the visual cycle. Vision Res 43, 2983–2990. [PubMed: 14611934]

Sparrow JR, Gregory-Roberts E, Yamamoto K, Blonska A, Ghosh SK, Ueda K, Zhou J, 2012. The bisretinoids of retinal pigment epithelium. Prog Retin Eye Res 31, 121–135. [PubMed: 22209824]

Sparrow JR, Wu Y, Kim CY, Zhou J, 2010. Phospholipid meets all-trans-retinal: the making of RPE bisretinoids. J Lipid Res 51, 247–261. [PubMed: 19666736]

Stewart MW, 2011. Aflibercept (VEGF-TRAP): the next anti-VEGF drug. Inflamm Allergy Drug Targets 10, 497–508. [PubMed: 21999177]

Stremplewski P, Komar K, Palczewski K, Wojtkowski M, Palczewska G, 2015. Periscope for noninvasive two-photon imaging of murine retina in vivo. Biomed Opt Express 6, 3352–3361. [PubMed: 26417507]

Suh S, Choi EH, Leinonen H, Foik AT, Newby GA, Yeh WH, Dong Z, Kiser PD, Lyon DC, Liu DR, Palczewski K, 2021. Restoration of visual function in adult mice with an inherited retinal disease via adenine base editing. Nat Biomed Eng 5, 169–178. [PubMed: 33077938]

Tano Y, Chandler D, Machemer R, 1980. Treatment of intraocular proliferation with intravitreal injection of triamcinolone acetonide. Am. J. Ophthalmol. 90, 810–816. [PubMed: 7446668]

Thibos LN, Applegate RA, Schwiegerling JT, Webb R, Members VST, 2002. Standards for reporting the optical aberrations of eyes. J. Refract. Surg. 18, S652–S660. [PubMed: 12361175]

Tomczewski S, Wegrzyn P, Borycki D, Auksorius E, Wojtkowski M, Curatolo A, 2022. Light-adapted flicker optoretinograms captured with a spatio-temporal optical coherence-tomography (STOC-T) system. Biomed Opt Express 13, 2186–2201. [PubMed: 35519256]

Treutwein B, Strasburger H, 1999. Fitting the psychometric function. Percept. Psychophys. 61, 87–106. [PubMed: 10070202]

Vinberg F, Palczewska G, Zhang J, Komar K, Wojtkowski M, Kefalov VJ, Palczewski K, 2019. Sensitivity of Mammalian Cone Photoreceptors to Infrared Light. Neuroscience 416, 100–108. [PubMed: 31400484]

Vogel CR, Arathorn DW, Roorda A, Parker A, 2006. Retinal motion estimation in adaptive optics scanning laser ophthalmoscopy. Opt. Express 14, 487–497. [PubMed: 19503363]

Vorontsov MA, Sivokon VP, 1998. Stochastic parallel-gradient-descent technique for high-resolution wave-front phase-distortion correction. Journal of the Optical Society of America a-Optics Image Science and Vision 15, 2745–2758.

Wald G, 1968. The molecular basis of visual excitation. Nature 219, 800–807. [PubMed: 4876934]

Walraven PL, Leebeek HJ, 1963. Foveal sensitivity of the human eye in the near infrared. J. Opt. Soc. Am. 53, 765–766. [PubMed: 13998626]

Wampler RD, Kissick DJ, Dehen CJ, Gualtieri EJ, Grey JL, Wang HF, Thompson DH, Cheng JX, Simpson GJ, 2008. Selective detection of protein crystals by second harmonic microscopy. J. Am. Chem. Soc. 130, 14076–14077. [PubMed: 18831587]

Wang BG, Konig K, Halbhuber KJ, 2010. Two-photon microscopy of deep intravital tissues and its merits in clinical research. J. Microsc. 238, 1–20. [PubMed: 20384833]

Watson AB, 2017. QUEST+: A general multidimensional Bayesian adaptive psychometric method. J. Vis. 17, 10.

Wei A, Mehta UV, Palczewska G, Palma AM, Hussey VM, Hoffmann LE, Diep A, Nguyen K, Le B, Chang SYS, Browne AW, 2021. Two-Photon Microperimetry: A Media Opacity-Independent Retinal Function Assay. Transl Vis Sci Techn 10.

Xu C, Webb WW, 1996. Measurement of two-photon excitation cross sections of molecular fluorophores with data from 690 to 1050 nm. J Opt Soc Am B 13, 481–491.

Yu G, Gao SQ, Dong Z, Sheng L, Sun D, Zhang N, Zhang J, Margeivicus S, Fu P, Golczak M, Maeda A, Palczewski K, Lu ZR, 2021. Peptide Derivatives of Retinylamine Prevent Retinal Degeneration with Minimal Side Effects on Vision in Mice. Bioconjug. Chem. 32, 572–583. [PubMed: 33677964]

Yung M, Klufas MA, Sarraf D, 2016. Clinical applications of fundus autofluorescence in retinal disease. Int J Retina Vitreous 2, 12. [PubMed: 27847630]

Zaidi Q, Pokorny J, 1988. Appearance of pulsed infrared light: second harmonic generation in the eye. Appl. Opt. 27, 1064–1068. [PubMed: 20531520]

Zhang F, Kurokawa K, Lassoued A, Crowell JA, Miller DT, 2019a. Cone photoreceptor classification in the living human eye from photostimulation-induced phase dynamics. Proc Natl Acad Sci U S A 116, 7951–7956. [PubMed: 30944223]

Zhang J, Choi EH, Tworak A, Salom D, Leinonen H, Sander CL, Hoang TV, Handa JT, Blackshaw S, Palczewska G, Kiser PD, Palczewski K, 2019b. Photic generation of 11-cis-retinal in bovine retinal pigment epithelium. J. Biol. Chem. 294, 19137–19154. [PubMed: 31694912]

Zhang J, Dong Z, Mundla SR, Hu XE, Seibel W, Papoian R, Palczewski K, Golczak M, 2015a. Expansion of first-in-class drug candidates that sequester toxic all-trans-retinal and prevent light-induced retinal degeneration. Mol Pharmacol 87, 477–491. [PubMed: 25538117]

Zhang J, Kiser PD, Badiee M, Palczewska G, Dong Z, Golczak M, Tochtrop GP, Palczewski K, 2015b. Molecular pharmacodynamics of emixustat in protection against retinal degeneration. J. Clin. Invest. 125, 2781–2794. [PubMed: 26075817]

Zhang N, Tsybovsky Y, Kolesnikov AV, Rozanowska M, Swider M, Schwartz SB, Stone EM, Palczewska G, Maeda A, Kefalov VJ, Jacobson SG, Cideciyan AV, Palczewski K, 2015c. Protein misfolding and the pathogenesis of ABCA4-associated retinal degenerations. Hum Mol Genet 24, 3220–3237. [PubMed: 25712131]

Zhao J, Ueda K, Riera M, Kim HJ, Sparrow JR, 2018. Bisretinoids mediate light sensitivity resulting in photoreceptor cell degeneration in mice lacking the receptor tyrosine kinase Mer. J. Biol. Chem. 293, 19400–19410. [PubMed: 30352873]

Zielinska A, Ciacka P, Szkulmowski M, Komar K, 2021. Pupillary Light Reflex Induced by Two-Photon Vision. Invest Ophthalmol Vis Sci 62, 23.

Zielinska A, Kiluk K, Wojtkowski M, Komar K, 2019. System for psychophysical measurements of two-photon vision. Photonics Lett Pol 11, 1–3.

Zipfel WR, Williams RM, Christie R, Nikitin AY, Hyman BT, Webb WW, 2003a. Live tissue intrinsic emission microscopy using multiphoton-excited native fluorescence and second harmonic generation. P Natl Acad Sci USA 100, 7075–7080.

Zipfel WR, Williams RM, Webb WW, 2003b. Nonlinear magic: multiphoton microscopy in the biosciences. Nat. Biotechnol. 21, 1369–1377. [PubMed: 14595365]

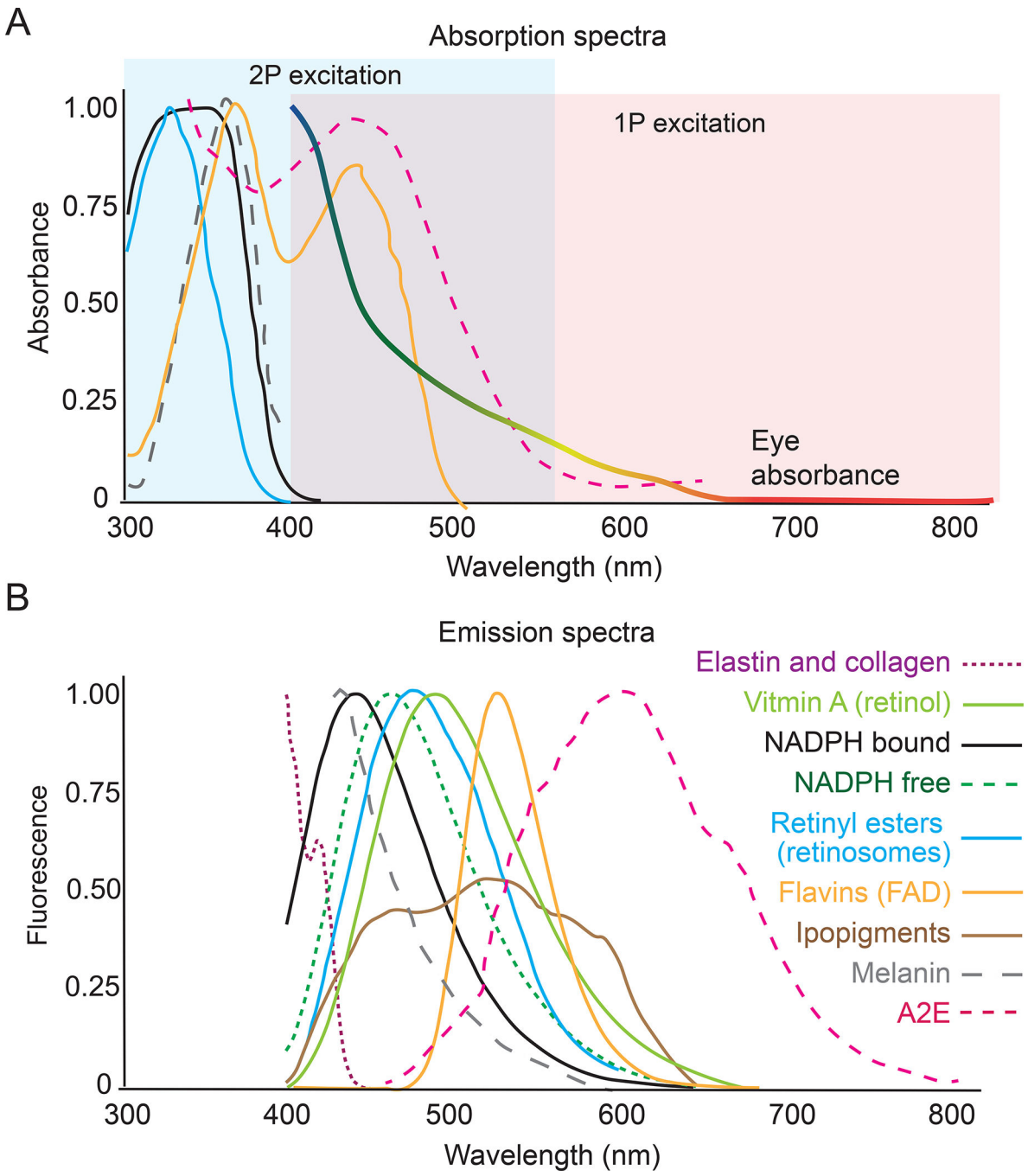

Fig. 1. Spectral characterization of the fluorescence properties of retinal pigments.

(**A**) Normalized absorption spectra of selected fluorophores showing the excitation spectral ranges of eye fluorophores in one- and two-photon processes. Absorption curve of the eyeball is depicted in rainbow; colors and line type for shown fluorophores are the same in (A) and (B). The red and blue rectangles depict the approximate spectral ranges in which effective in vivo excitation is possible by one-photon (1P) and two-photon (2P), respectively. A limitation of the excitation of 1P and 2P in the long-wavelength side is the absorption of water increasing for wavelengths longer than 1100 nm. Human crystalline

lens, absorbs almost all incident energy at wavelengths shorter than 400 nm, limiting the ability to excite 1P with the short-wavelengths (Sliney, 2002). (**B**) Normalized emission spectra of endogenous fluorophores present in the retina. The graphs are based on published data (Croce and Bottiroli, 2014; Garwin and Saari, 2000; Schweitzer et al., 2007; Zipfel et al., 2003a).

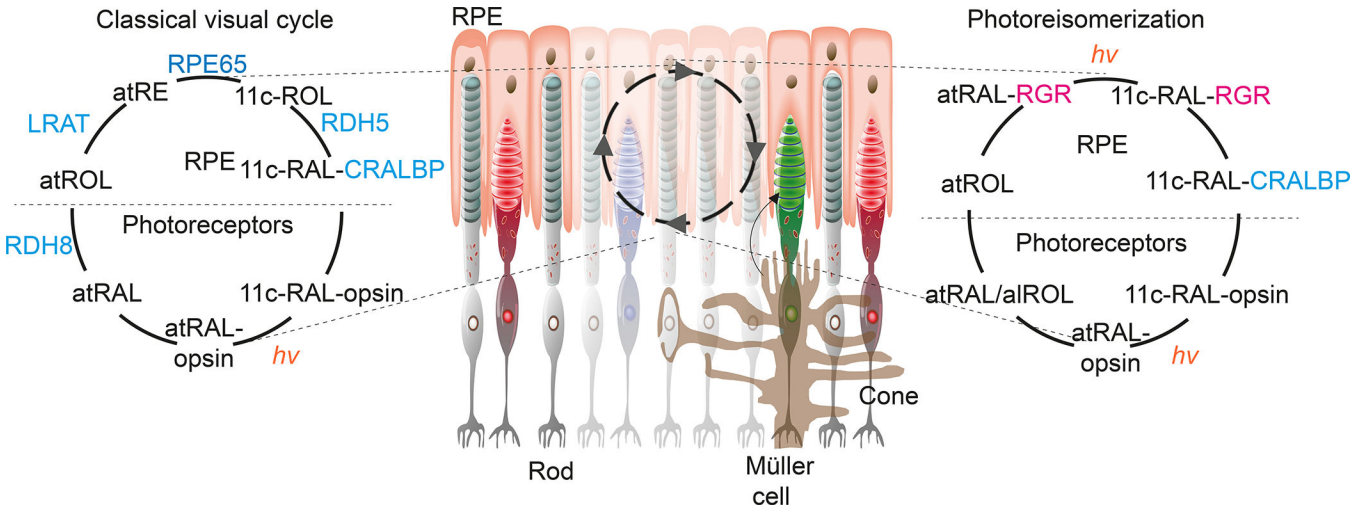

Fig. 2. Mechanisms of chromophore regeneration.

A key step in visual pigment regeneration is the isomerization of all-*trans*-RAL to 11-*cis*-RAL. While the classical visual cycle regenerates 11-*cis*-RAL through a series of enzyme-catalyzed steps (in blue) independently of light, retinal G protein-coupled receptor (RGR) additionally contributes to the regeneration of 11-*cis*-RAL under photopic conditions (in red). More detailed information can be found in (Kiser and Palczewski, 2021; Palczewski and Kiser, 2020). Adapted from Zhang *at al.*(Zhang et al., 2019b). Fig. 3. **1PEF *versus* 2PEF.** 2PEF results in greater selectivity in the excitation region, while penetration in turbid media is enhanced by half-energy infrared radiation (1/2 ω_0). Photographs and rendering were inspired by an original photo made by Steve Ruzin and Holly Aaron, UC Berkeley.

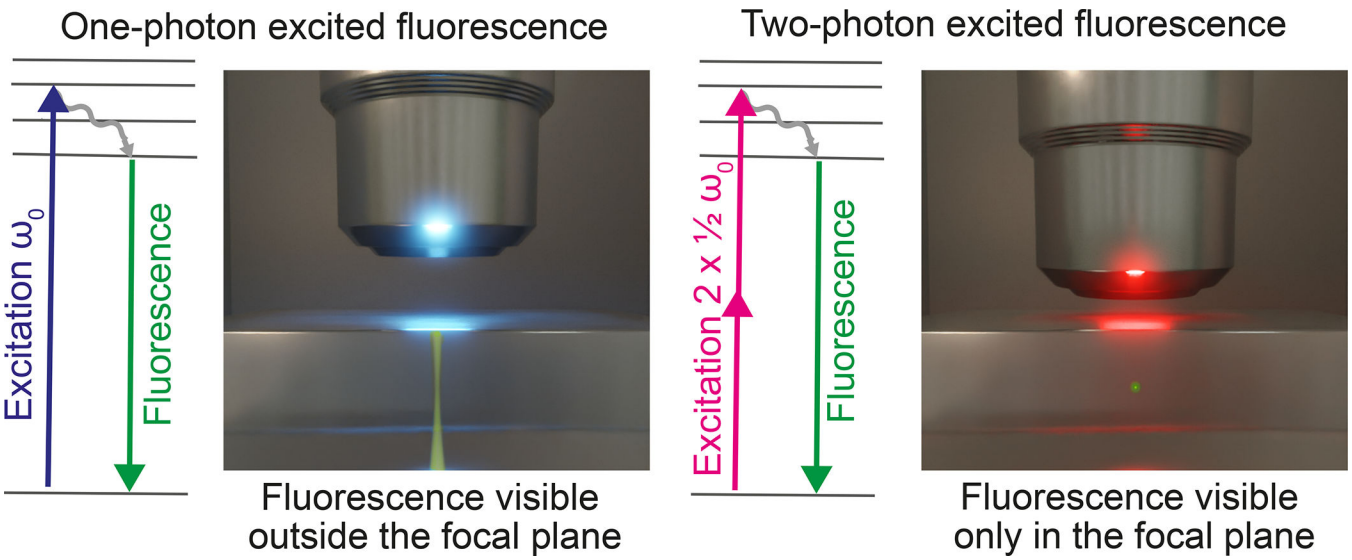

Fig. 3. 1PEF *versus* 2PEF.

Diagrams show the energy levels of the fluorophore molecules for one-photon (1P) and two-photon (2P) excitation on the left and right, respectively. The energy (corresponding to radiation frequency ω_0) provided by the excitation light in the 1P process is marked in blue, while the energy in the 2P process (1/2 ω_0) is marked in red, energy transition of fluorescence photons are shown in green, and vibrational relaxation in gray. Spread of green fluorescence light in renderings demonstrates that 2PE results in greater selectivity in the excitation region (optical confinement). Photographs and rendering were inspired by an original photo made by Steve Ruzin and Holly Aaron, UC Berkeley.

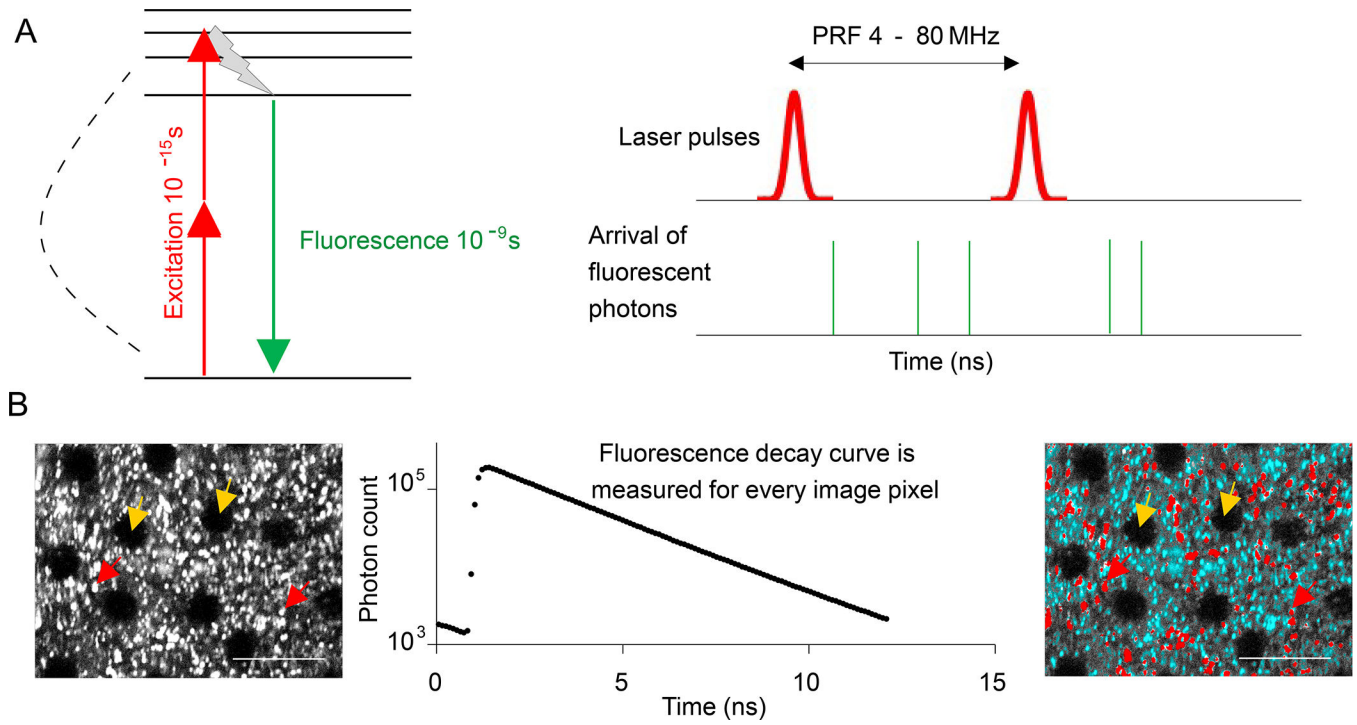

Fig. 4. Short-pulse lasers enable 2PE imaging based on fluorescence intensity and fluorescence lifetime measurements.

(**A**) Diagram of 2PE. Laser pulses are depicted in red, fluorescence photons in green, vibrational relaxation in gray, and non-radiative energy release in black (intermittent line). Photon arrival times with respect to exciting laser pulses at variable pulse repetition frequency (PRF) are measured for every pixel. (**B**) Images of an RPE in the intact eye of an albino mouse. Left, gray scale image based on the 2PEF intensity; right, image in pseudo color scale based on fluorescence lifetime for each pixel; exemplary fluorescence decay is shown in the middle. In both image panels: nuclei, lacking fluorescence are indicated with yellow arrows; red arrows indicate exemplary retinosomes, shown in red pseudo-color. Teal color indicates bisretinoids. Scale bars 25 μm.

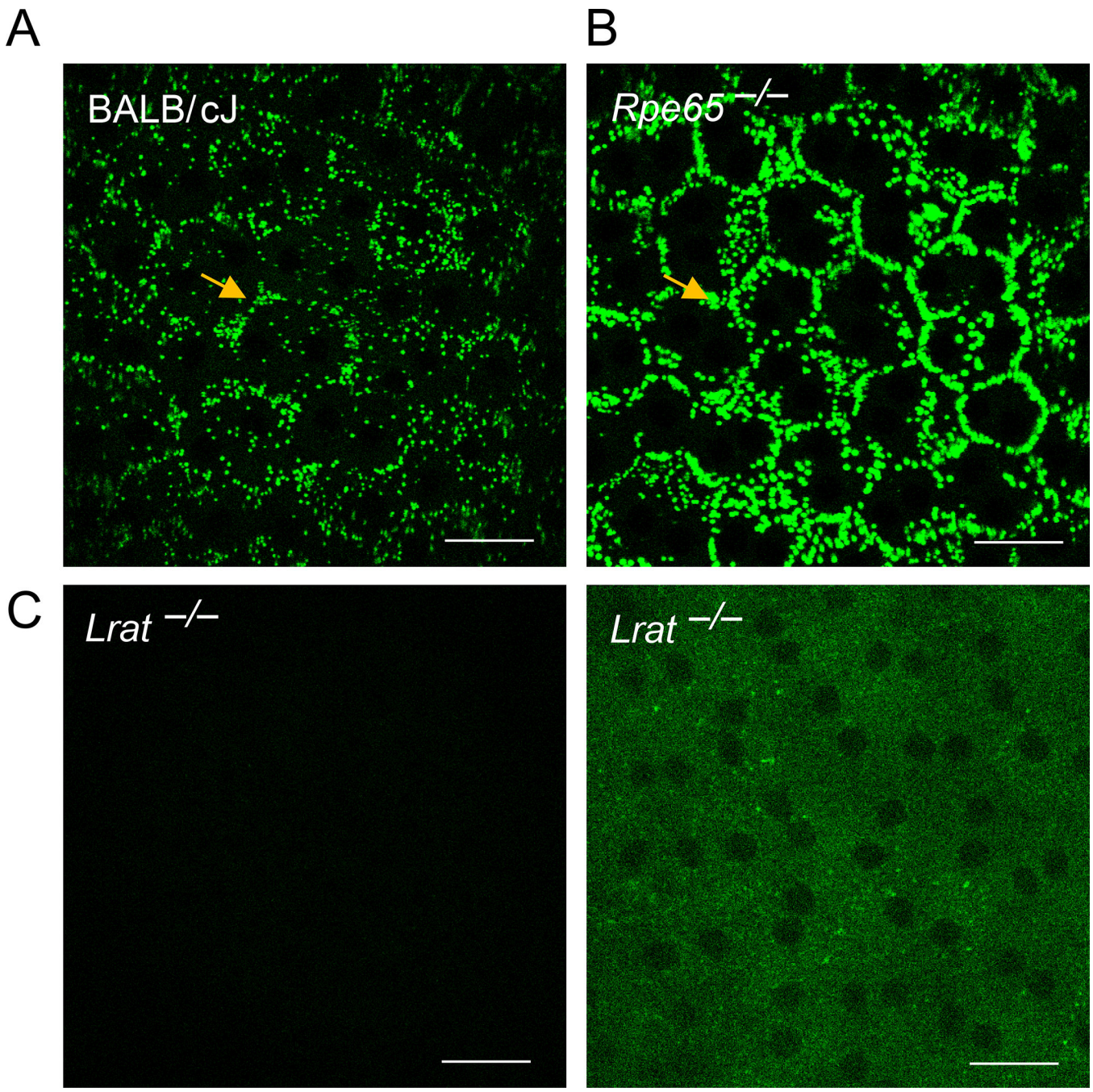

Fig. 5. Aberrant function of the retinoid cycle detected by 2P imaging

(Palczewska et al., 2010). Retinyl esters storage compartments called retinosomes are located next to RPE cell membranes in WT mice (**A**). Brighter and larger retinosomes are present in the *Rpe65* $^{-/-}$ mice (**B**). For the same imaging conditions as used in A and B no RPE fluorescence was measured in *Lrat* $^{-/-}$ mice (**C**, left panel). With increased excitation power and detector gain, double nuclei (dark circles) and membranes of RPE cells became visible (C, right panel). Yellow arrows indicate exemplary retinosomes; genotypes are indicated in the upper left corners; scale bars, 25 μm.

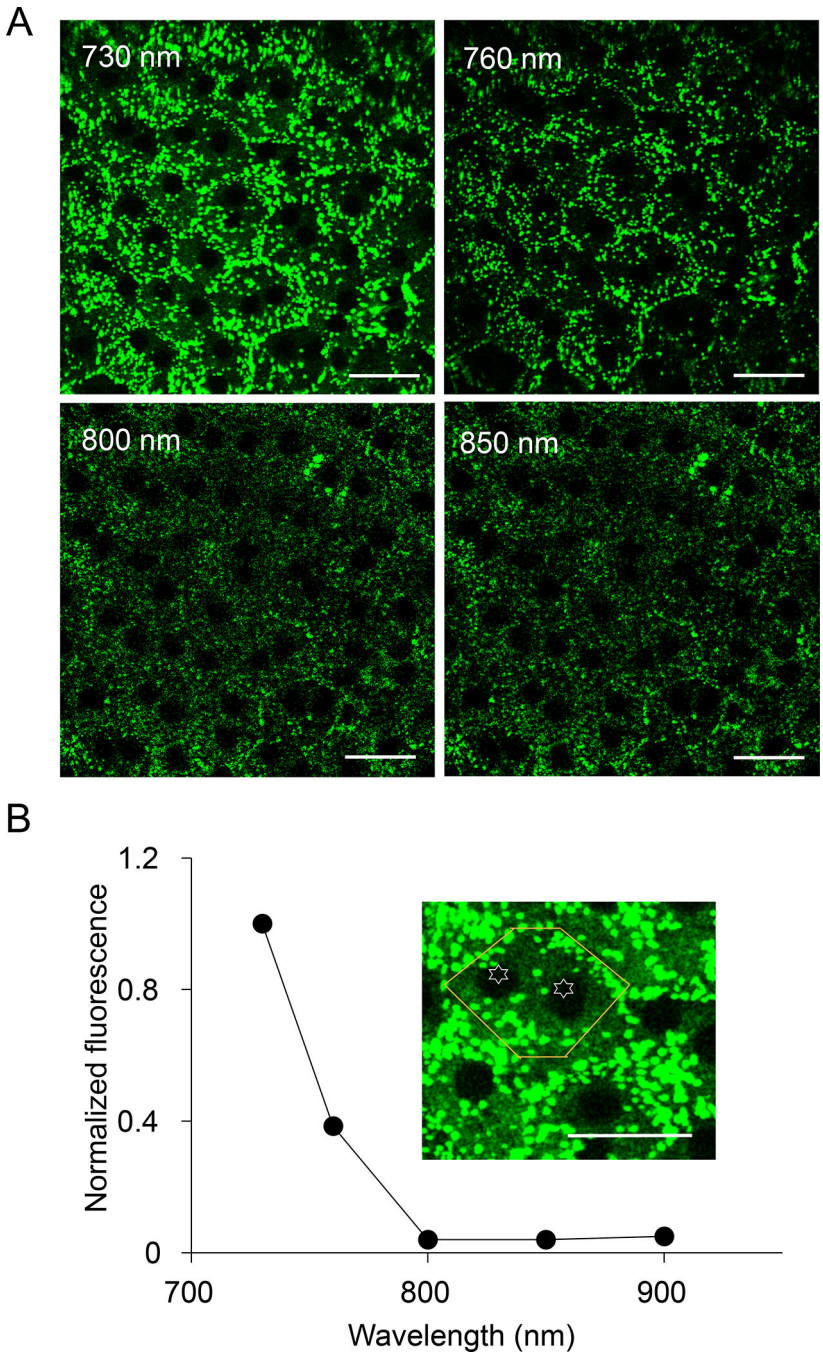

Fig. 6. The pattern and intensity of fluorescence in RPE cells of a 3-month-old WT mouse vary with changes in 2PE wavelength.

(**A**) Bright retinosomes located predominantly along cell membranes are visible with 730-nm and 760-nm excitation. For the same excitation power, retinosomes fluoresce weakly with excitation wavelengths longer than 760 nm. (**B**). The graph shows RPE fluorescence as a function of excitation wavelength normalized to that at 730 nm. Inset: Magnified image of the RPE cell. Orange lines outline a single RPE cell, with dual nuclei indicated by white-outlined stars. Scale bars correspond to 25 μm in all panels (Palczewska et al., 2010).

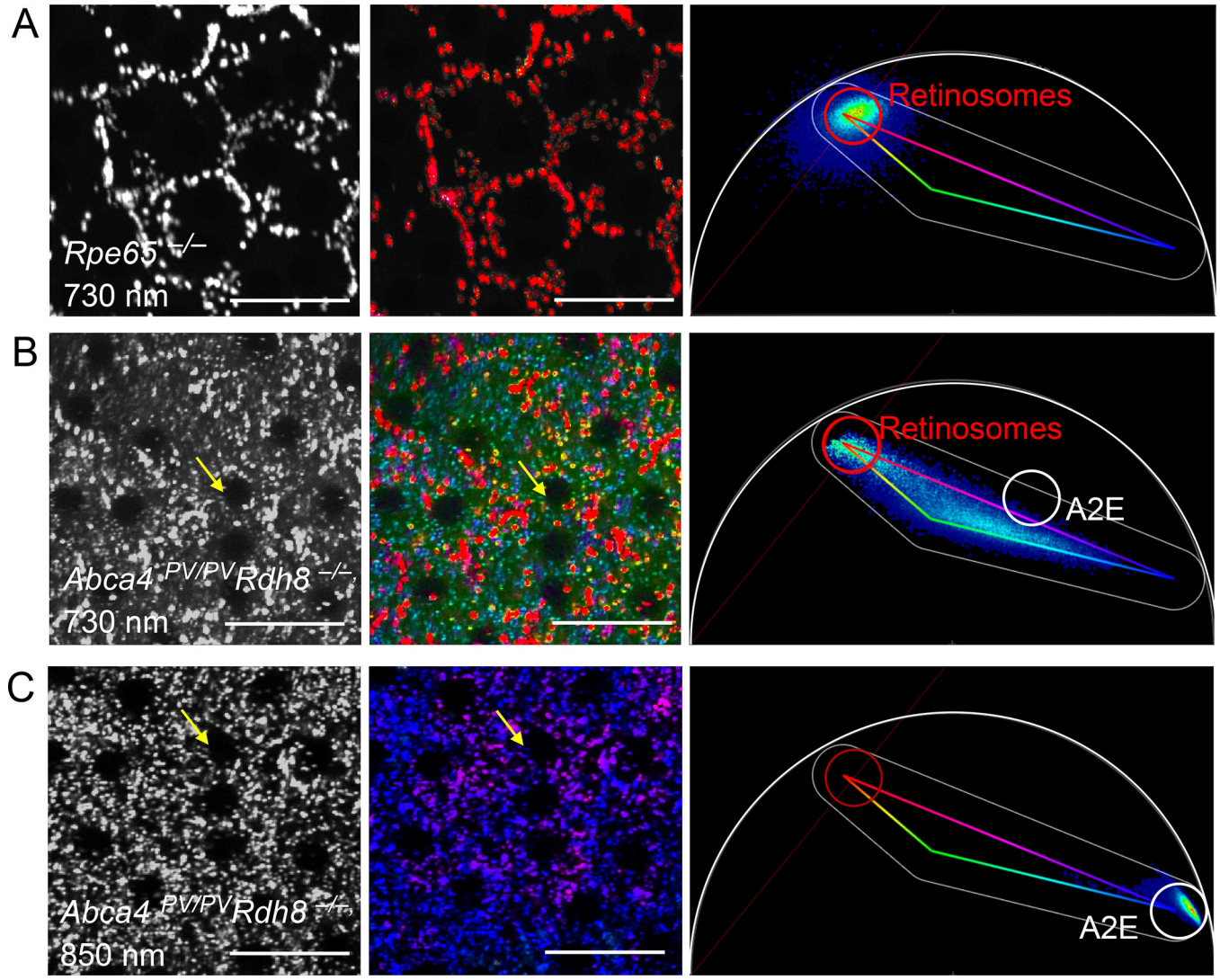

Fig. 7. Subcellular distribution of retinyl esters and bisretinoids in the RPE of intact mouse eyes.

Left column, fluorescence intensity images; center column, corresponding FLIM, based on the phasor plots shown in the right column; Excitation wavelengths and genotypes are indicated on the images in the left column. (**A**) Data from albino *Rpe65* $^{-/-}$ mice; (**B**) and (**C**) are data from *Abca4*$^{PV/PV}$*Rdh8*$^{-/-}$ mice. Yellow arrows indicate the same nucleus. The red circle in A surrounds phasor points corresponding to retinyl ester-containing retinosomes in the *Rpe65* $^{-/-}$ mouse; and the red circle on the phasor plot in B identifies retinosomes in a *Abca4*$^{PV/PV}$*Rdh8*$^{-/-}$ mouse eye illuminated with 730-nm short-pulse light. White circles indicate the location of phasor points corresponding to 10 mM synthetic A2E (Palczewska *et al.*, 2020). Scale bars, 25 μm.

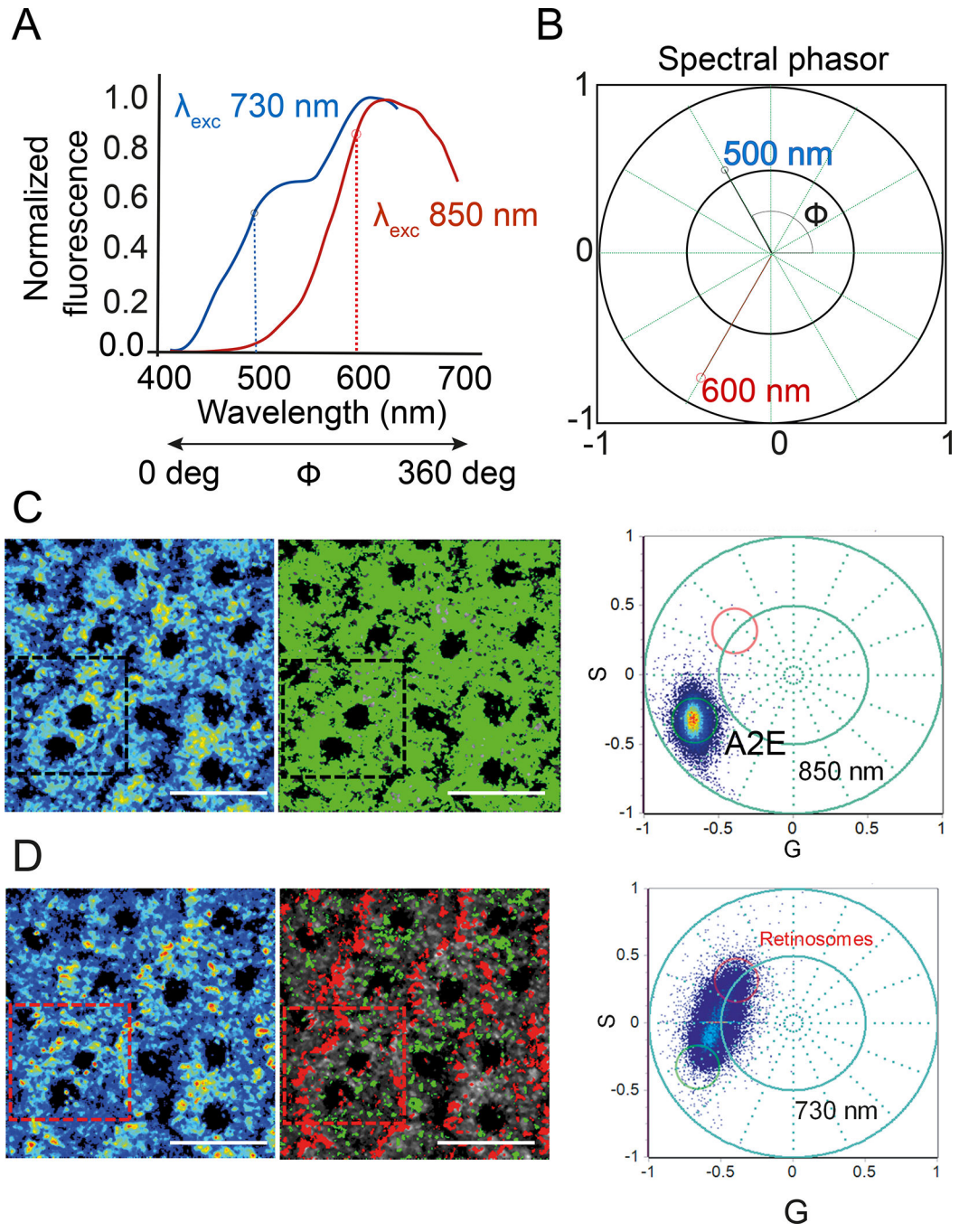

Fig. 8. Spectral phasor analysis can distinguish between retinosomes and A2Es within RPE cells of the eye of an albino *Abca4*$^{PV/PV}$*Rdh8*$^{-/-}$ mouse, without staining.

(**A**) Fluorescence emission spectra from the RPE for 850-nm and 730-nm excitation. (**B**) Schematic diagram showing the construction of the spectral phasor, with the marked points corresponding to the fluorescence values for 500 nm and 600 nm from panel (A). (**C**) Data obtained with the 850-nm excitation wavelength. (**D**) Data obtained with 730-nm excitation. (C and D, Left) 2PE fluorescence intensity-based images. (C and D, Center) Pseudocolor images obtained by applying the red and green cursor selections shown in the spectral

phasor plots. (C and D, Right) Spectral phasor plots. Scale bars 25 μm. Adapted from Fig. 3 of Palczewska G, Boguslawski J, Stremplewski P, Kornaszewski L, Zhang J, Dong Z, *et al.* Noninvasive two-photon optical biopsy of retinal fluorophores. *Proc. Natl. Acad. Sci. U. S. A.* 2020;117(36):22532–43 (Palczewska et al., 2020).

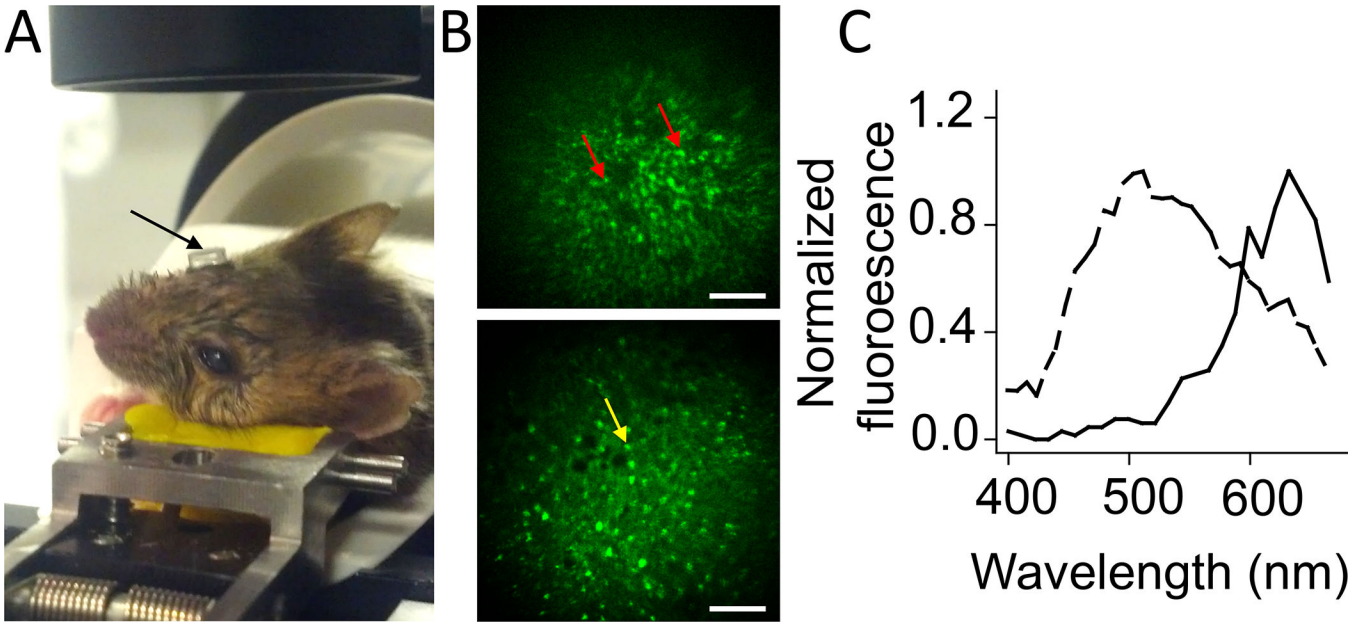

Fig. 9. 2P imaging of live mouse RPE *in vivo* with sensorless adaptive optics (Palczewska et al., 2014a).

(**A**) A *Abca4*$^{-/-}$*Rdh8*$^{-/-}$ mouse is shown. For imaging, the mouse is placed on a heated stage with two rotational and three translational axes. A contact lens, indicated with black arrow, covers the eye facing the objective. (**B**) Top panel, 2PO image of the RPE in a live 6-month-old albino *Rpe65* $^{-/-}$ mouse, obtained with 730-nm IR light. Enlarged retinosomes are indicated with red arrows. Bottom panel, 2PO image of the RPE in a live *Abca4*$^{-/-}$*Rdh8*$^{-/-}$ mouse, obtained with 850-nm IR light. Yellow arrow indicates fluorescent granules that accumulated in the RPE 10 days after exposure to bright visible light. Scale bars 100 μm. (**C**) Fluorescence emission spectra from the RPE of a *Rpe65* $^{-/-}$ mouse (black dashed line), and from a *Abca4*$^{-/-}$*Rdh8*$^{-/-}$ mouse (solid black line).

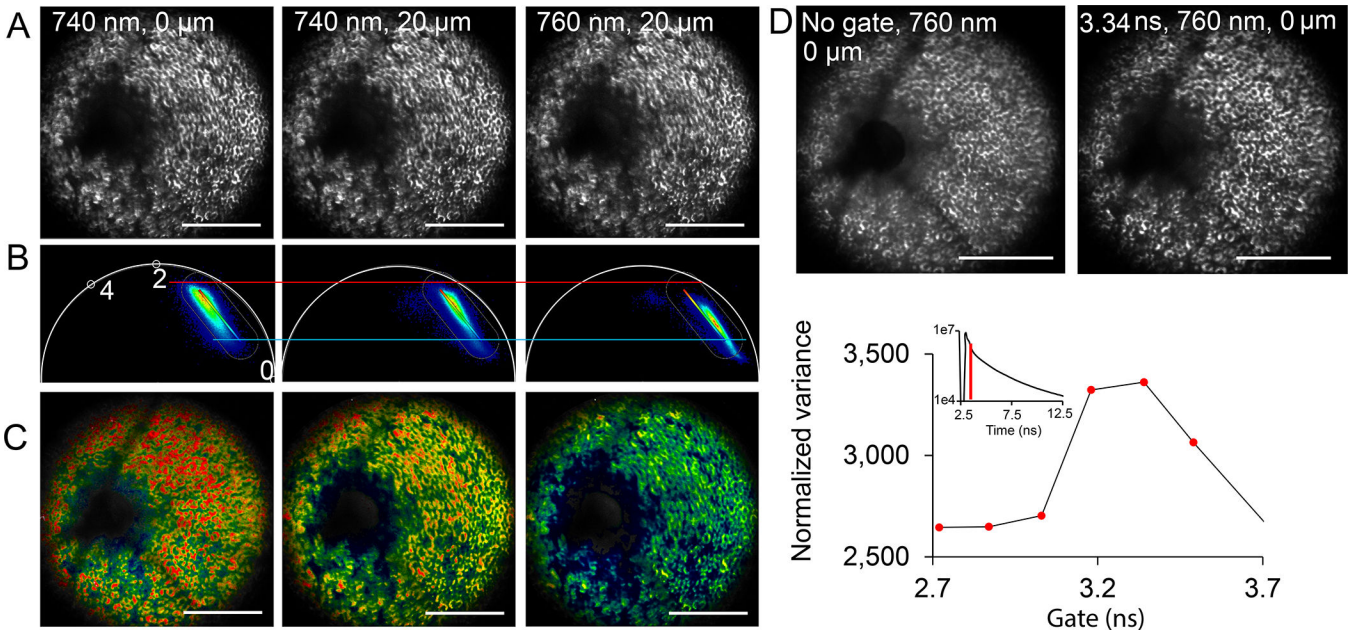

Fig. 10. Overcoming the impact of melanin on imaging retinosomes in live pigmented animals (Palczewska et al., 2020).

(**A**) Fluorescence intensity-based images of the RPE in *Rpe65* $^{-/-}$ mice. Excitation wavelengths (740 nm or 760 nm) and axial location shifts (0 or 20 μm) are indicated in each panel. (**B**) Fluorescence-lifetime universal-semicircle phasor plots of the data, as collected in A. Red and blue lines through all three panels indicate relocation of the groupings of phasor points towards shorter lifetimes, after the following changes: 1) shifting focal position 20 μm towards the choroid (middle panel); and 2) increasing excitation wavelength from 740 nm to 760 nm. Numbers along the outline of the semicircle indicate 0, 2, and 4 ns. (**C**) Fluorescence lifetime images (FLIM), with colors assigned based on the rainbow bars in the corresponding phasor plots (directly above). The dark blue color indicates image pixels with melanin as the major component, and the red color indicates pixels where the larger contribution is from retinyl esters (Palczewska et al., 2020). (**D**) By stop-gating photons with very short arrival times, image quality is improved. Top-left panel, no gate; top-right panel, gate at 3.34 ns, corresponding to 0.19 ns after the peak of the fluorescence decay. The normalized variance sharply increased with the gate at 3.18 ns and further increased with the gate at 3.34 ns. The red vertical line in the insert indicates one of the gate positions for which the normalized variance was calculated. Scale bars 250 μm in all.

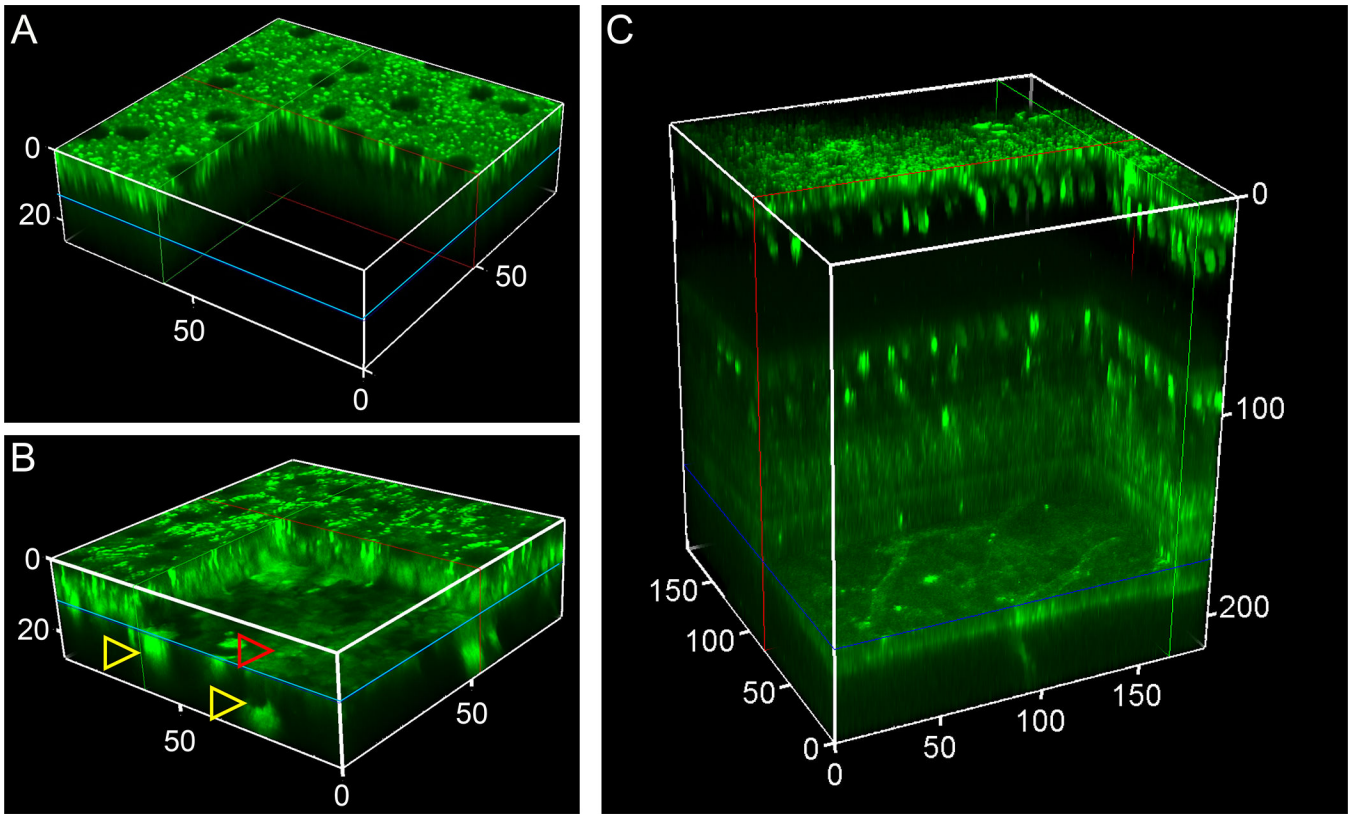

Fig. 11. Identification of healthy and degenerated retinal cells by two-photon fluorescence imaging, based on endogenous fluorophores or fluorescent labeling.

Imaging based on endogenous fluorophores enables 3D reconstruction of the RPE and photoreceptor interface in a WT mouse (**A**), and in a phagocytosis-deficient *Mertk*$^{-/-}$*Abca4*$^{-/-}$*Rdh8*$^{-/-}$ mouse (**B**) (Palczewska et al., 2016). Exemplary degenerating photoreceptor is indicated with a red-arrow point (recognized by location and morphology), and macrophages (having larger size and shape) are indicated with yellow-arrow points. (**C**) 3D reconstruction of the entire retina, ranging from the RPE to the ganglion cell layer (GCL). Two-photon images from a BALB/cJ mouse eye were obtained 72 hr after intraocular injection with rhodamine-tagged peanut agglutinin. In all panels, X,Y,Z-axis scales are in μm and the RPE is located at Z=0 μm.

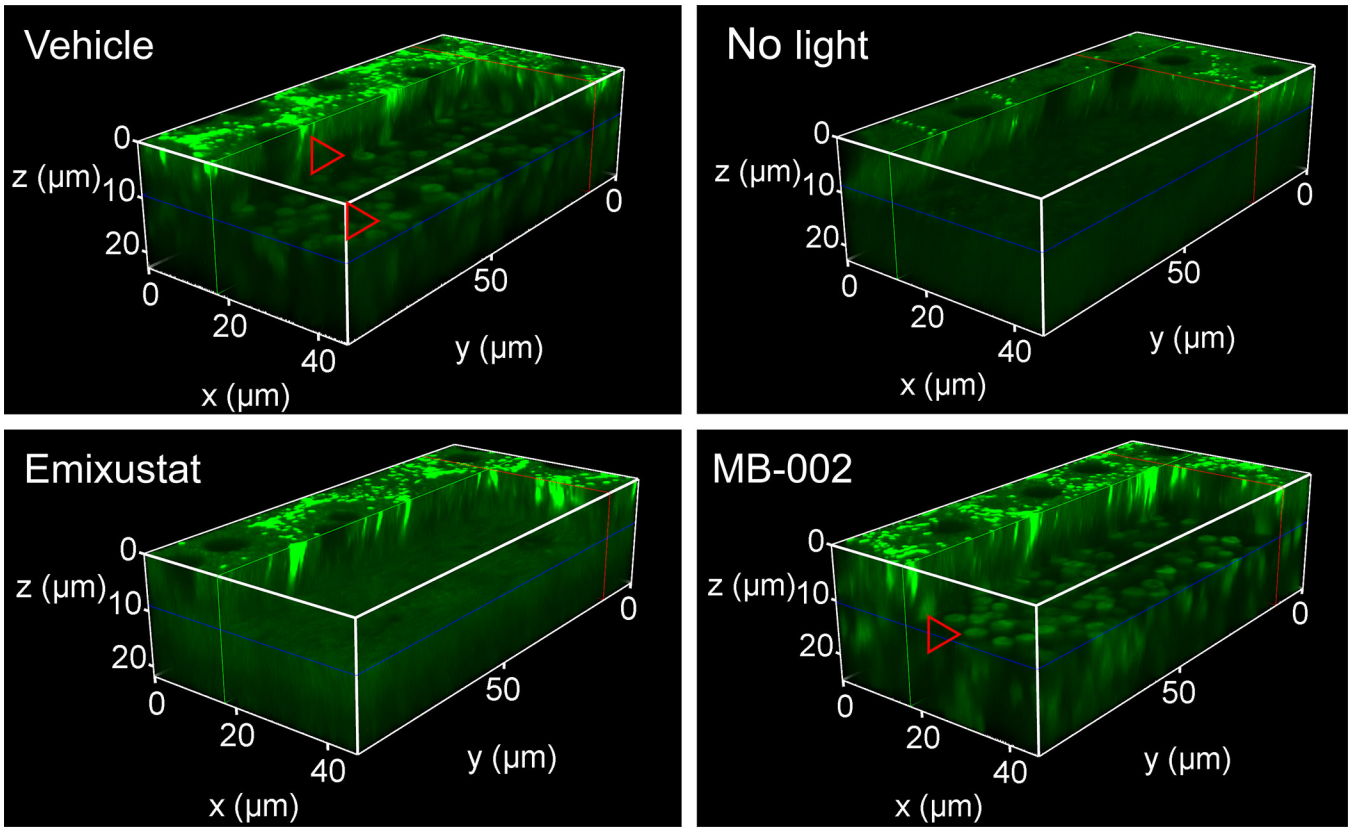

Fig. 12. Treatment with retinoid-cycle modulators protects photoreceptors in BALB/c mice from bright light-induced retinal degeneration.

Enlarged photoreceptors, an early indication of bright light-induced retinal degeneration, are present in mice that were treated either with vehicle (oil) or with MB-002, a compound that lacks a primary amine (Zhang *et al.*, 2015b); but not in mice that were treated with Emixustat, or in mice that were not exposed to bright light. In each 3D reconstruction, treatment is indicated in the upper left corner; the RPE is at the top, z=0 μm; a section through the photoreceptors is shown 8–12 μm below the RPE, and enlarged photoreceptors are indicated with red-outlined arrow points (Zhang *et al.*, 2015b).

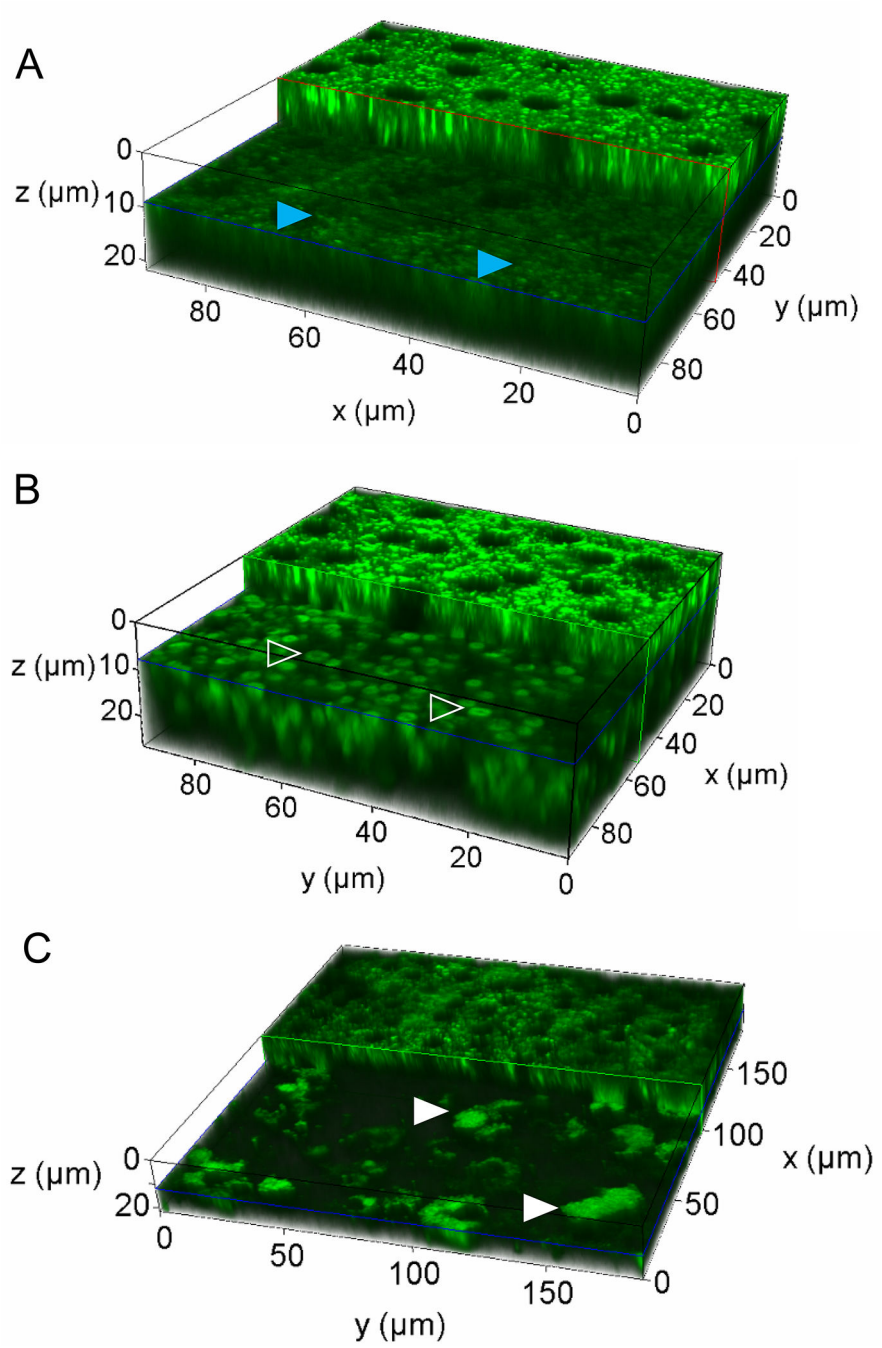

Fig. 13. 3D reconstructions revealing retinal degeneration (Palczewska et al., 2020).

The sequence of steps leading to retinal degeneration in *Abca4* $^{-/-}$*Rdh8* $^{-/-}$ mice after exposure to bright light was elucidated, based on 3D reconstructions from the z-stack of TPM images (Maeda *et al.*, 2014). (**A**) In mouse eyes unexposed to bright light, photoreceptor outer segments are faintly visible under the RPE. Exemplary photoreceptors are indicated with blue arrow-points. (**B**) At day 3 after the exposure to bright light, a multitude of enlarged, donut-shape photoreceptors are present under the RPE. Exemplary enlarged photoreceptors are indicated with white-outlined arrow-points. (**C**) No

photoreceptors, but large quantities of macrophages are visible under the RPE at day 7 after exposure to bright light. Exemplary macrophages are indicated with white arrow-points. The RPE is at the top in A, B, and C, z=0 μm.

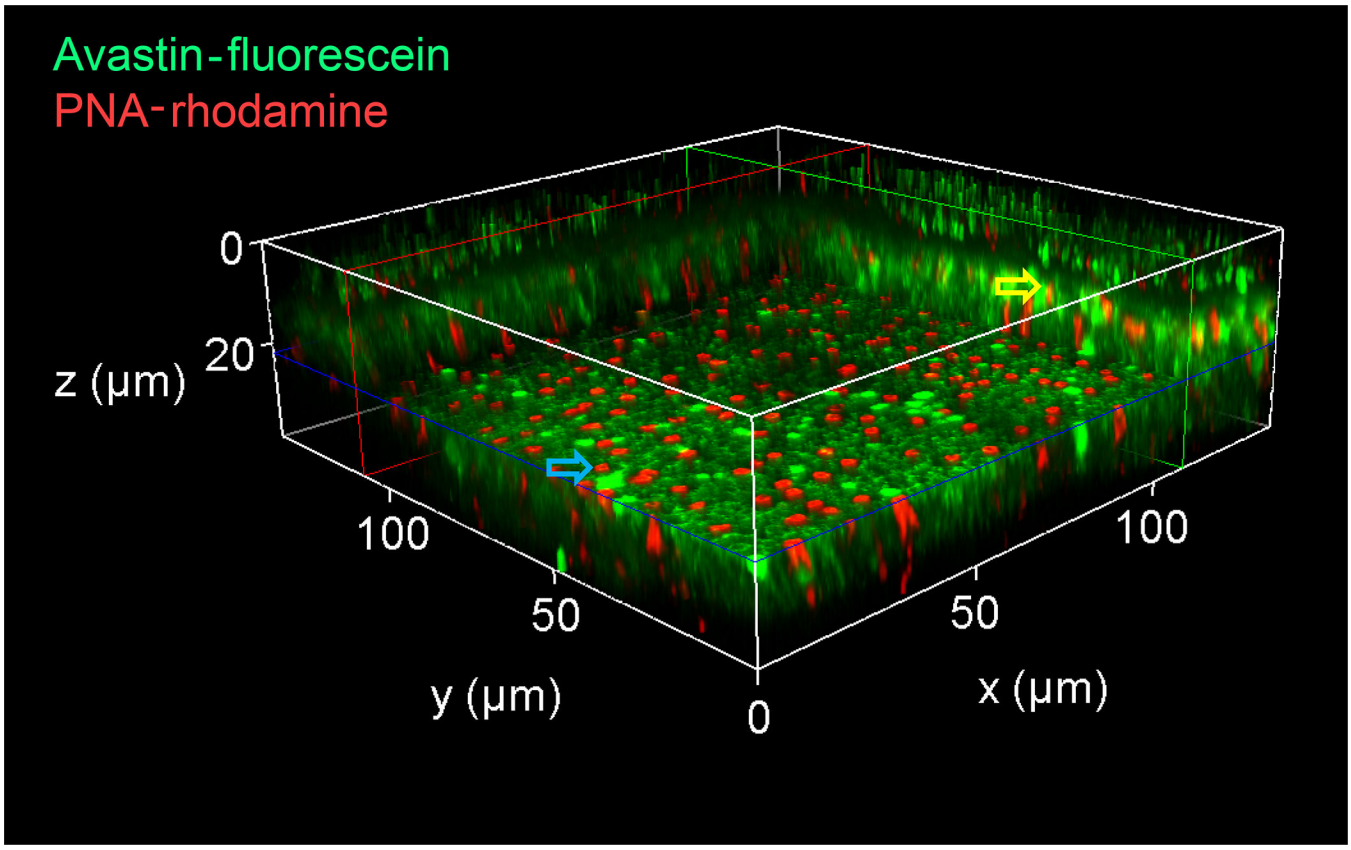

Fig. 14. 2PEF imaging of the intact mouse eye after intra-ocular injection with fluorescein-labeled Avastin and rhodamine-labeled PNA.

Shown is the 3D reconstruction from z-stack images, with a section through the inner segments at 20 μm; the RPE is at 0 μm. Blue- and yellow-outlined arrows indicate exemplary inner and outer segments, respectively

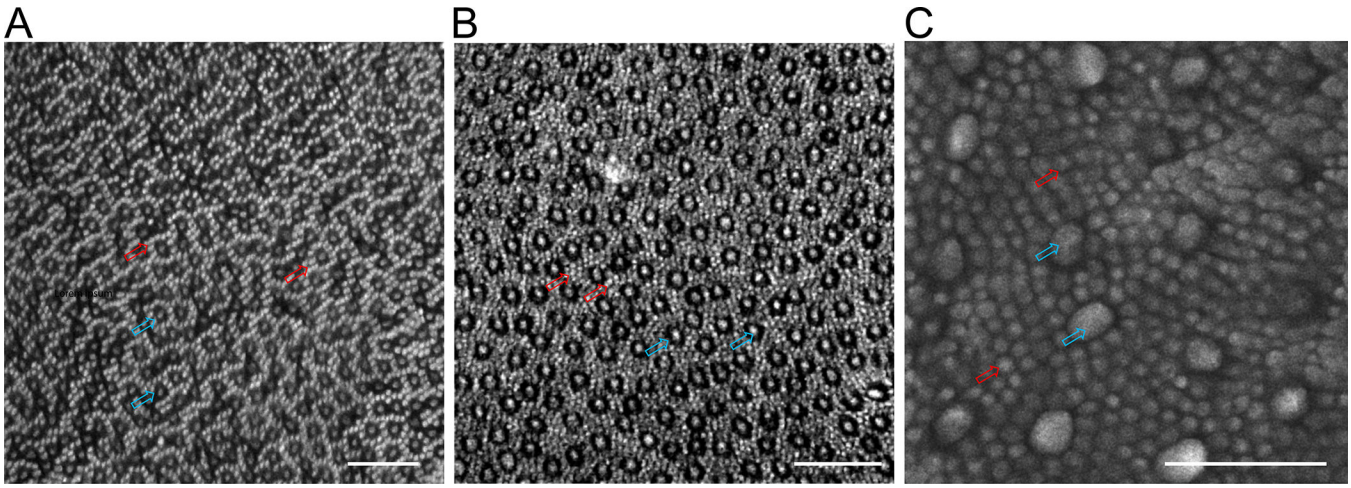

Fig. 15. Two-photon fluorescence imaging of monkey retina at different eccentricities.

Images of the outer segments at: (**A**) 1 mm and (**B**) 6 mm away from the fovea. (**C**) Image of the inner segments at 10 mm from the fovea. Red arrows point to examples of rod photoreceptors; blue arrows indicate examples of cone photoreceptors. Scale bars = 25 μm.

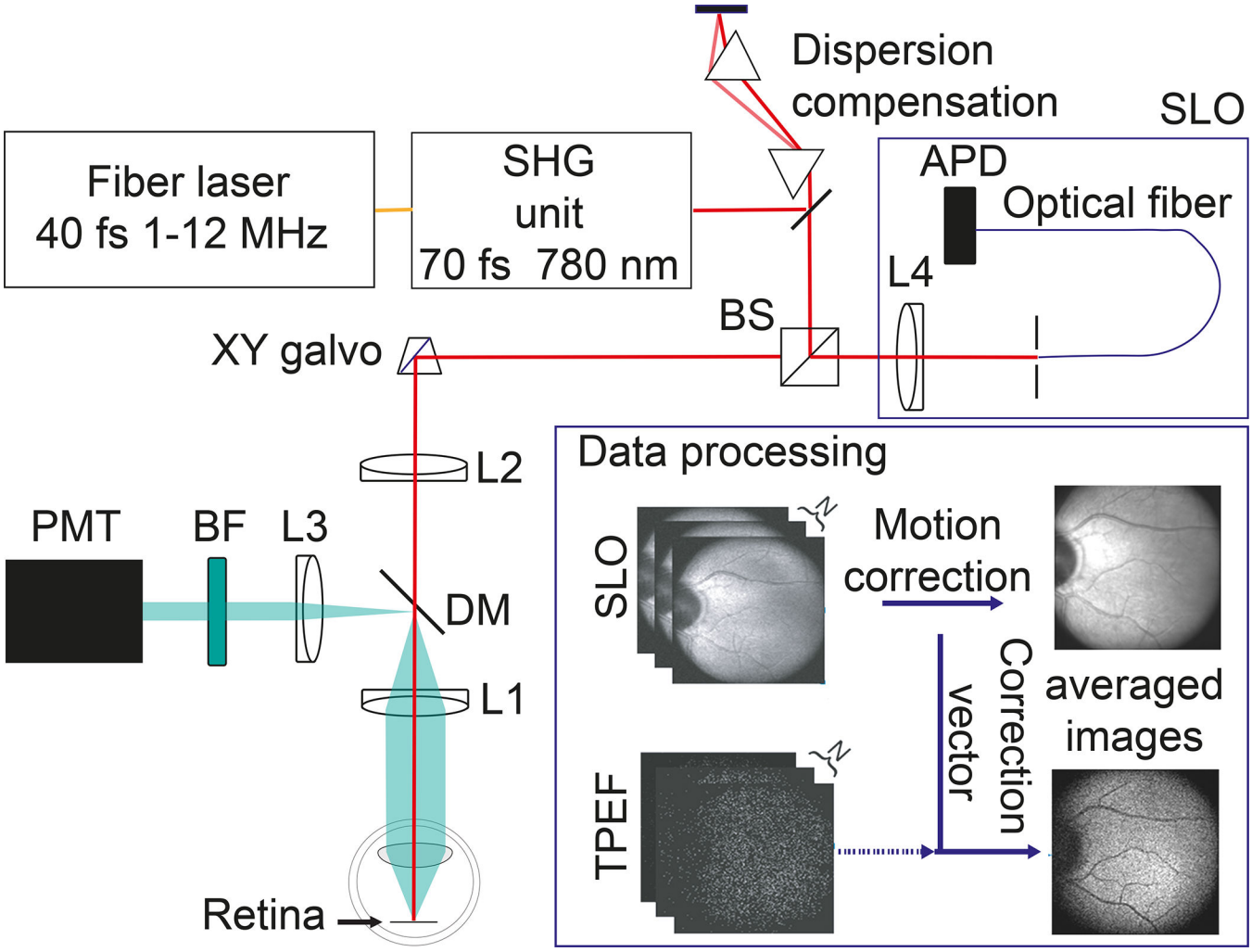

Fig. 16. Schematic diagram of the optical system of a 2PO.

APD, avalanche photodiode; BF, set of bandpass filters; BS, beam splitter; DM, dichroic mirror; L, lens; PMT, photomultiplier tube. The inset depicts image processing. Thus, images obtained with the SLO module are used to identify a motion-correction vector that can be used to eliminate motion from 2PEF images and average them to obtain sufficient contrast for the fluorescence signal. Adapted from Figure 1 of Boguslawski J, Palczewska G, Tomczewski S, Milkiewicz J, Kasprzycki P, Stachowiak D, Komar K, Marzejon MJ, Sikorski BL, Hudzikowski A, Głuszek A, Łaszczych Z, Karnowski K, Soboń G, Palczewski K, Wojtkowski M. In vivo imaging of the human eye using a 2-photon-excited fluorescence scanning laser ophthalmoscope. *J Clin Invest.* 2022;132(2):e154218.

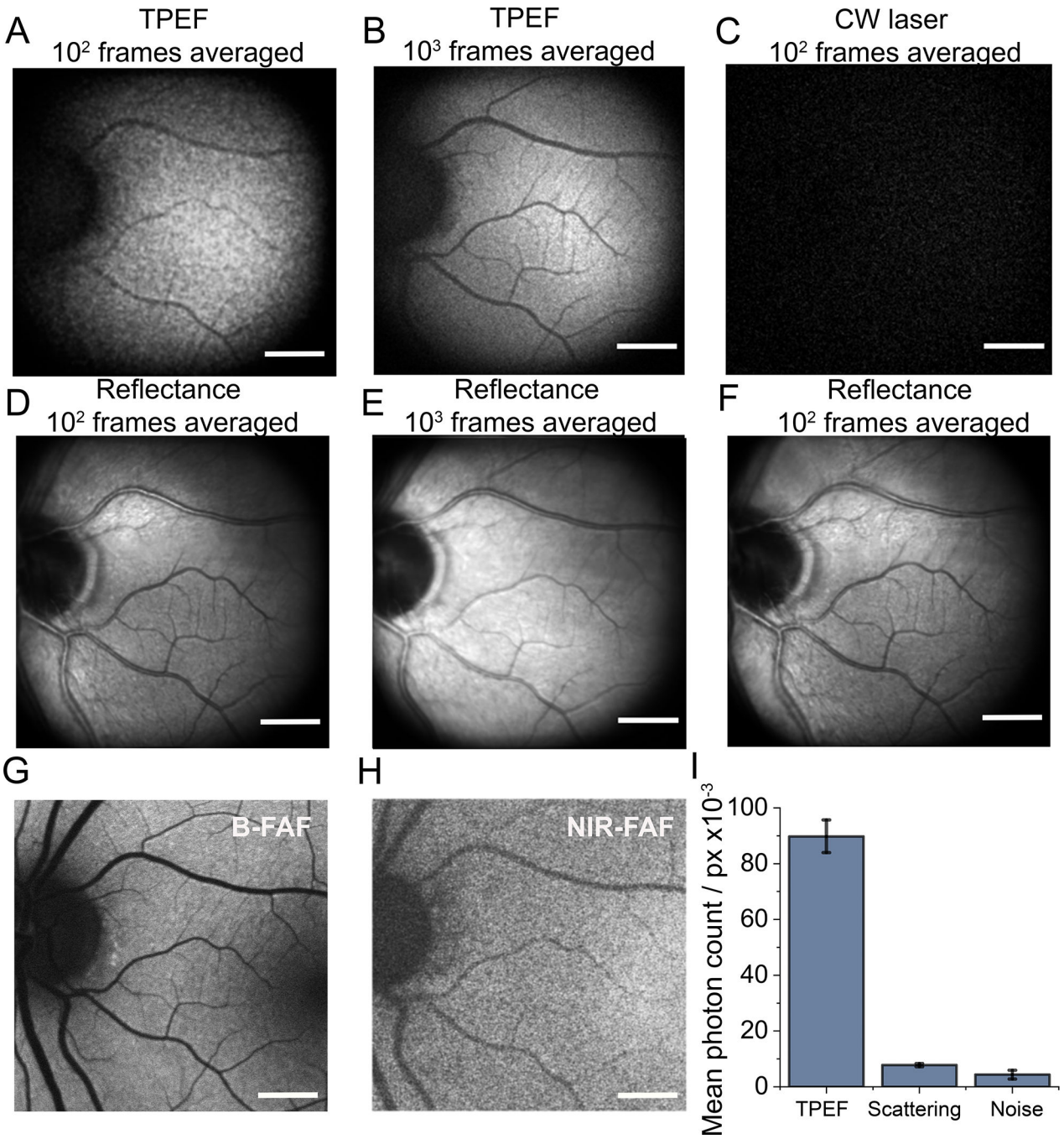

Fig. 17. Two-photon excited fluorescence (2PEF) light coming from the human retina *in vivo*.

Averaging of 100 (**A**) or 1000 (**B**) 2PEF images enables fluorescence imaging of the fundus. Compensation for eye movements is realized by using SLO images based on near IR (NIR) light scattered on the retina (corresponding images in panels D - F). When continuous-wave (CW) NIR laser light at 825 nm was used, a significant reduction in 2PEF signal intensity was demonstrated (**C**), with comparable quality of the reference reflectance image (**F**). Images obtained by a one-photon excitation autofluorescence (FAF) system with blue light-FAF (488-nm excitation) (**G**), and near-infrared autofluorescence

(NIR-FAF) (**H**) are shown for reference. A comparison of fluorescence intensities including noise and backscattered light leakage (**I**) is shown to quantify the process performance. The average number of photon counts per pixel (pc/px) within the field of view (FOV) of the device is plotted. Scale bars, 1 mm. Adapted from Figure 2 of Boguslawski J, Palczewska G, Tomczewski S, Milkiewicz J, Kasprzycki P, Stachowiak D, Komar K, Marzejon MJ, Sikorski BL, Hudzikowski A, Głuszek A, Łaszczych Z, Karnowski K, Soboń G, Palczewski K, Wojtkowski M. In vivo imaging of the human eye using a 2-photon-excited fluorescence scanning laser ophthalmoscope. *J Clin Invest.* 2022;132(2):e154218.

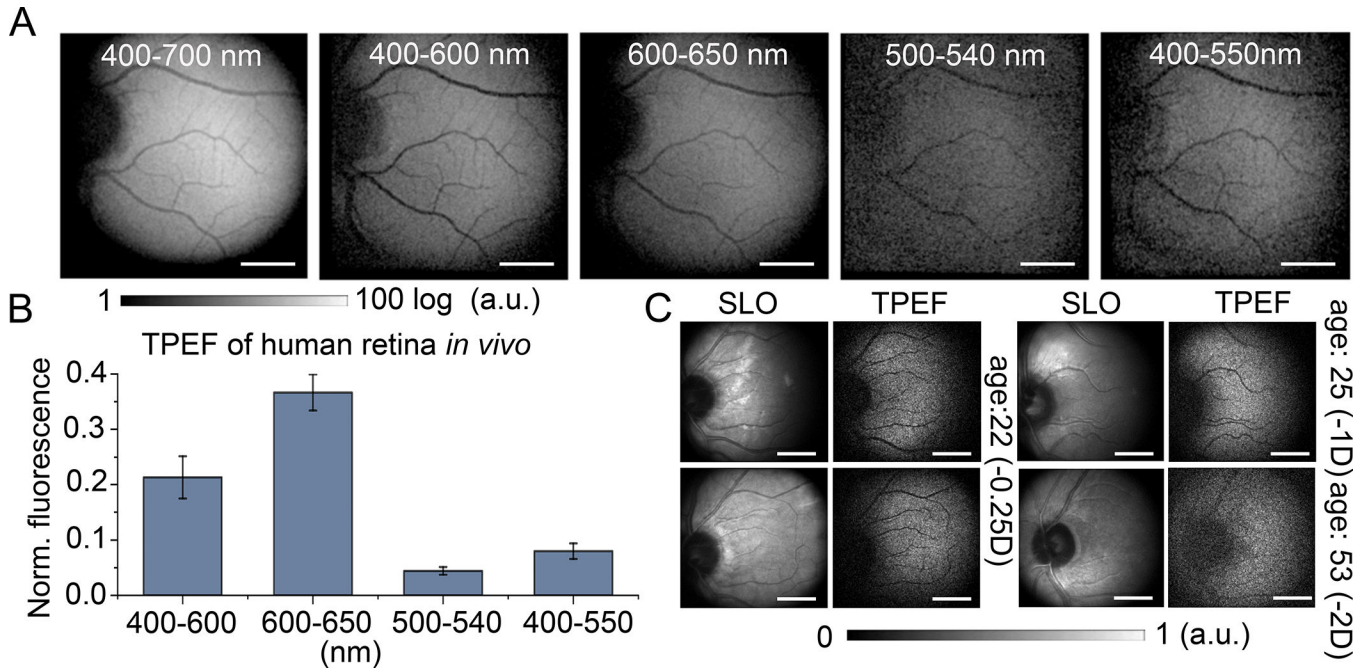

Fig. 18. Spectrally resolved 2PO imaging performance.

(A) Spectral properties of the 2PEF of human fundus recorded in spectral ranges of 400–700 nm, 400–600 nm, 600–650 nm, 500–540 nm, and 400–550 nm; 1000 frames were used in each case. (**B**) Plot showing relative fluorescence change in four spectral ranges normalized with respect to the 400–700 nm range for human 2PEF imaging (n = 10). (**C**) Examples of eye imaging results from sixteen healthy volunteers of different age groups. Despite differences in contrast due to the limited ergonomics of the system, the 2PEF signal from the fundus of the eye was recorded in all cases. Scale bars, 1.5 mm. Adapted from Figure 3 of Boguslawski J, Palczewska G, Tomczewski S, Milkiewicz J, Kasprzycki P, Stachowiak D, Komar K, Marzejon MJ, Sikorski BL, Hudzikowski A, Głuszek A, Łaszczych Z, Karnowski K, Soboń G, Palczewski K, Wojtkowski M. *In vivo* imaging of the human eye using a 2-photon-excited fluorescence scanning laser ophthalmoscope. *J Clin Invest*. 2022;132(2):e154218.

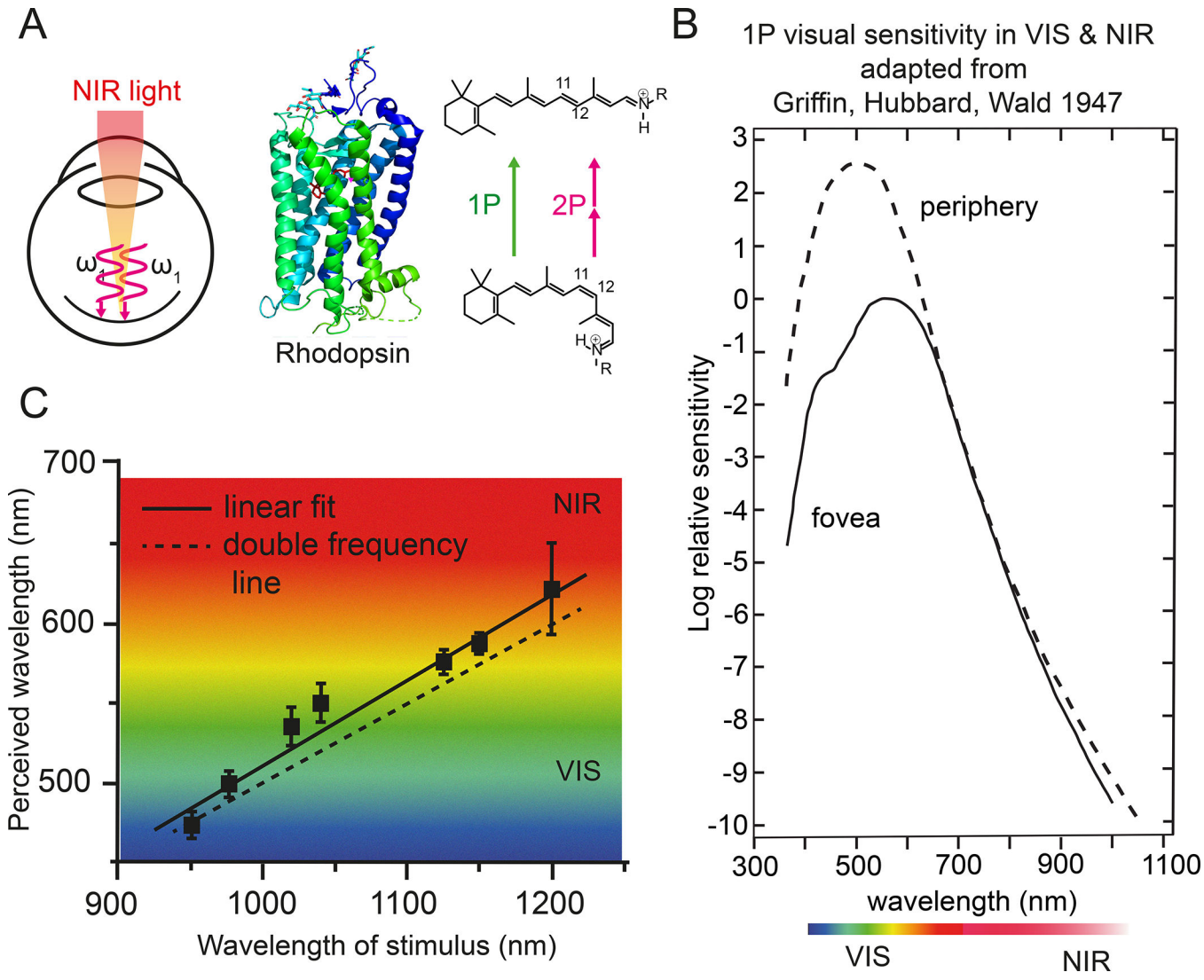

Fig 19. Two-Photon vision.

Two-Photon vision is the process by which the eye is sensitive to infrared light and perceives it as light from the visible range of the spectrum. (**A**). Absorption of short pulses of near-infrared (NIR) light by rhodopsin leads to the initiation of phototransduction. (**B**). Adaptation of the original chart from 1947 (Griffin et al., 1947), showing one-photon human visual spectral sensitivity. The sensitivity threshold for the fovea at maximum visual sensitivity at λ=580 nm relative to sensitivity at λ=1060 nm (extrapolated) is 10 orders of magnitude larger. (**C**). Graph showing the results of measuring the perceived wavelength *versus* the retinal stimulation wavelength with pulsing light (Palczewska et al., 2018). For reference, the diagram shows a dashed line corresponding to the frequency doubling of the incident radiation. Panel C was adapted with permission from Optica Publishing Group. Donald R. Griffin, Ruth Hubbard, and George Wald, “The sensitivity of the human eye to infra-red radiation,” *J. Opt. Soc. Am.* 37, 546–554 (1947). © The Optical Society.

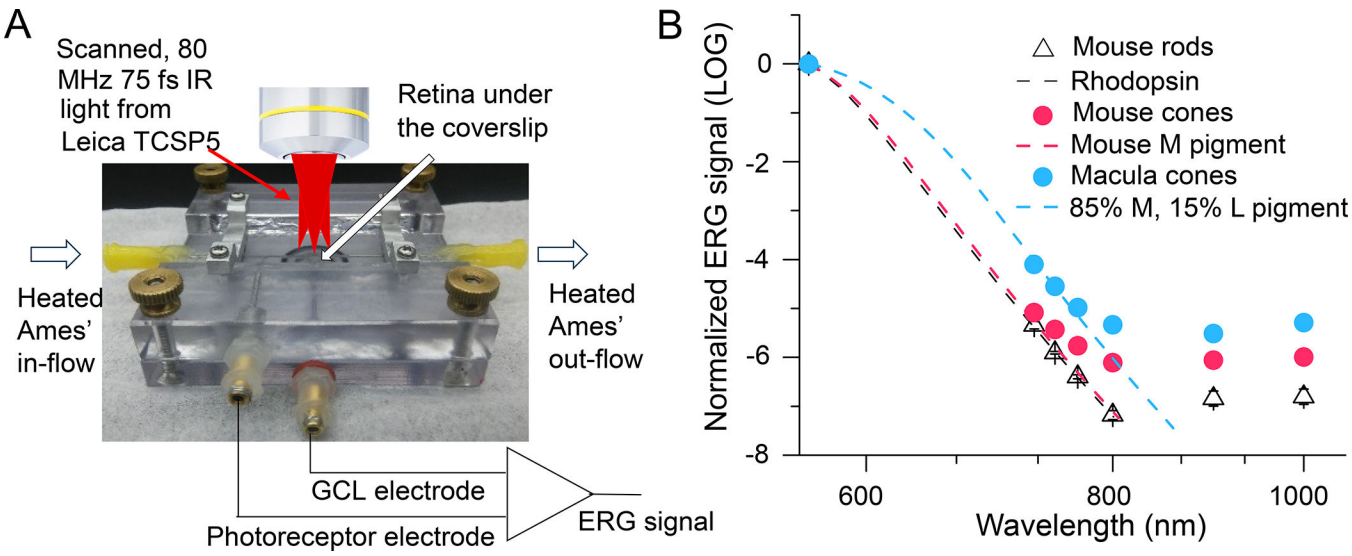

Fig. 20. Two-photon stimulation of mammalian photoreceptors.

(**A**) Apparatus for simultaneous two-photon imaging and *ex vivo* ERG recording (Palczewska *et al.*, 2014c; Vinberg *et al.*, 2019). In this device 2P microscopic imaging enabled precise focusing of stimulus light on the photoreceptor layer. Retinas were continuously perfused with heated Ames' medium. Pulsed, 80-MHz infrared (IR) light stimuli were generated by a tunable Ti:Saphire laser; and for the reference, visible 561-nm light was generated by a diode-pumped solid-state laser. The same objective, 0.25 NA, 10x, was used for both delivery and imaging. (**B**) Two-photon sensitivities are plotted as a function of stimulus wavelength. Data were normalized relative to the sensitivity to 561-nm visible light, and are indicated as follows: mouse rods, open black triangles; mouse cones, filled red circles; primate parafoveal photoreceptors, filled blue circles. Dashed lines represent the expected one-photon ERG result for the following: rhodopsin, black; mouse-cone M pigment, red; and a mix of 85% macaque M and 15% L pigments. Adapted from: Neuroscience, volume 416, Frans Vinberg, Grazyna Palczewska, Jianye Zhang, Katarzyna Komar, Maciej Wojtkowski, Vladimir J. Kefalov, Krzysztof Palczewski, Sensitivity of Mammalian Cone Photoreceptors to Infrared Light, 100–108, Copyright 2012, with permission from Elsevier.

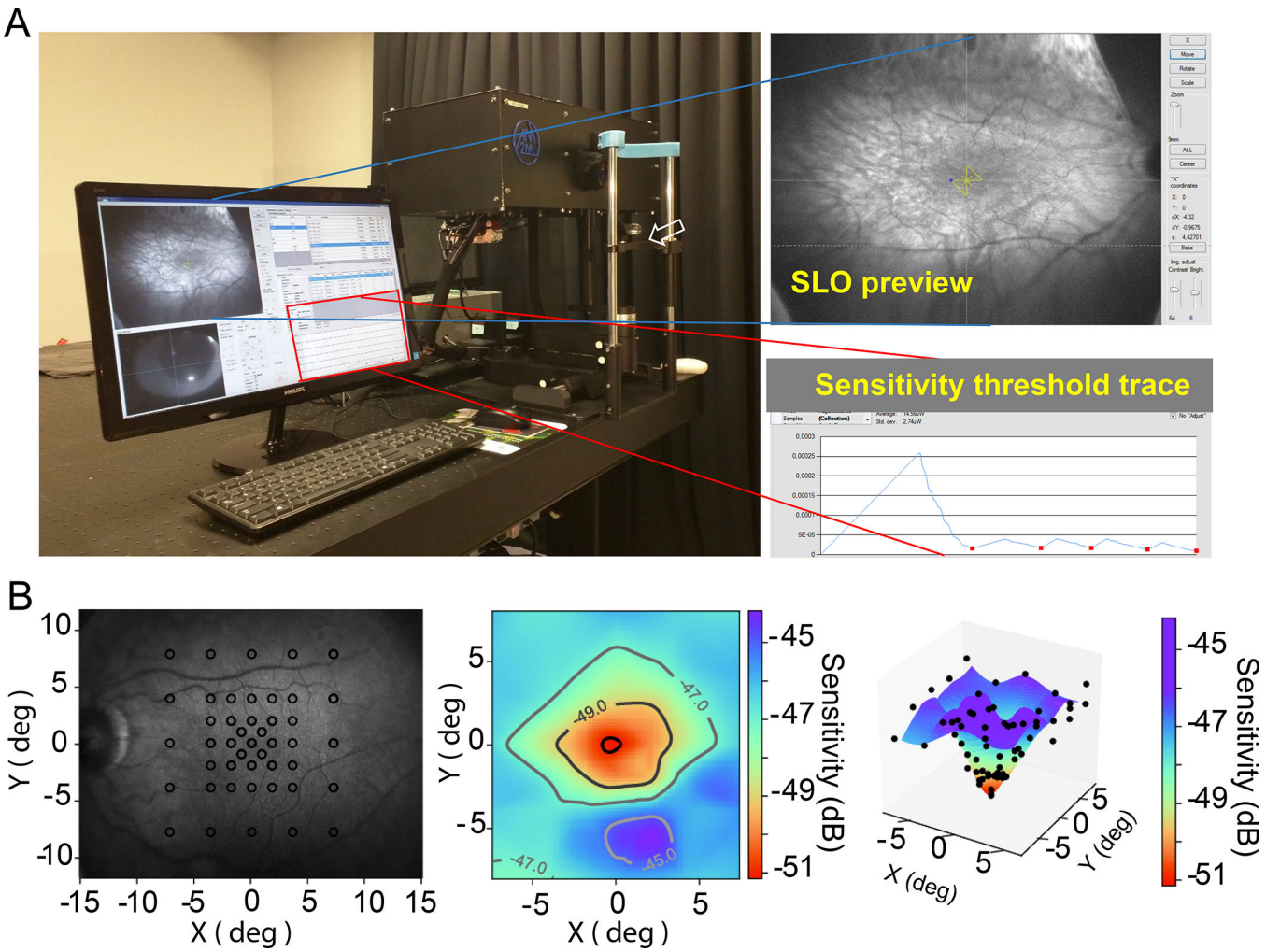

Fig. 21. IR perimetry of the human eye.

(**A**) First clinical instrument: the chinrest is indicated with a white-outlined arrow; enlarged panels on the right show a SLO fundus preview (top), and a preview of the measurement trace, with red points indicating the sensitivity threshold of the measured eye of the subject (bottom). (**B**) Visual field sensitivity map in response to IR stimulation. From left to right: 1) SLO image of the retina with overlaid stimuli locations outlined in black circles; 2) Contour map of visual sensitivity to IR light, where sensitivity isolines are drawn at 2-dB steps; 3) Three-dimensional visualization of sensitivity to IR light. Individual measurements, shown as black points, are overlaid on the colored interpolation, based on the color scale shown on the right. The results were published in (Ruminski *et al.*, 2019).

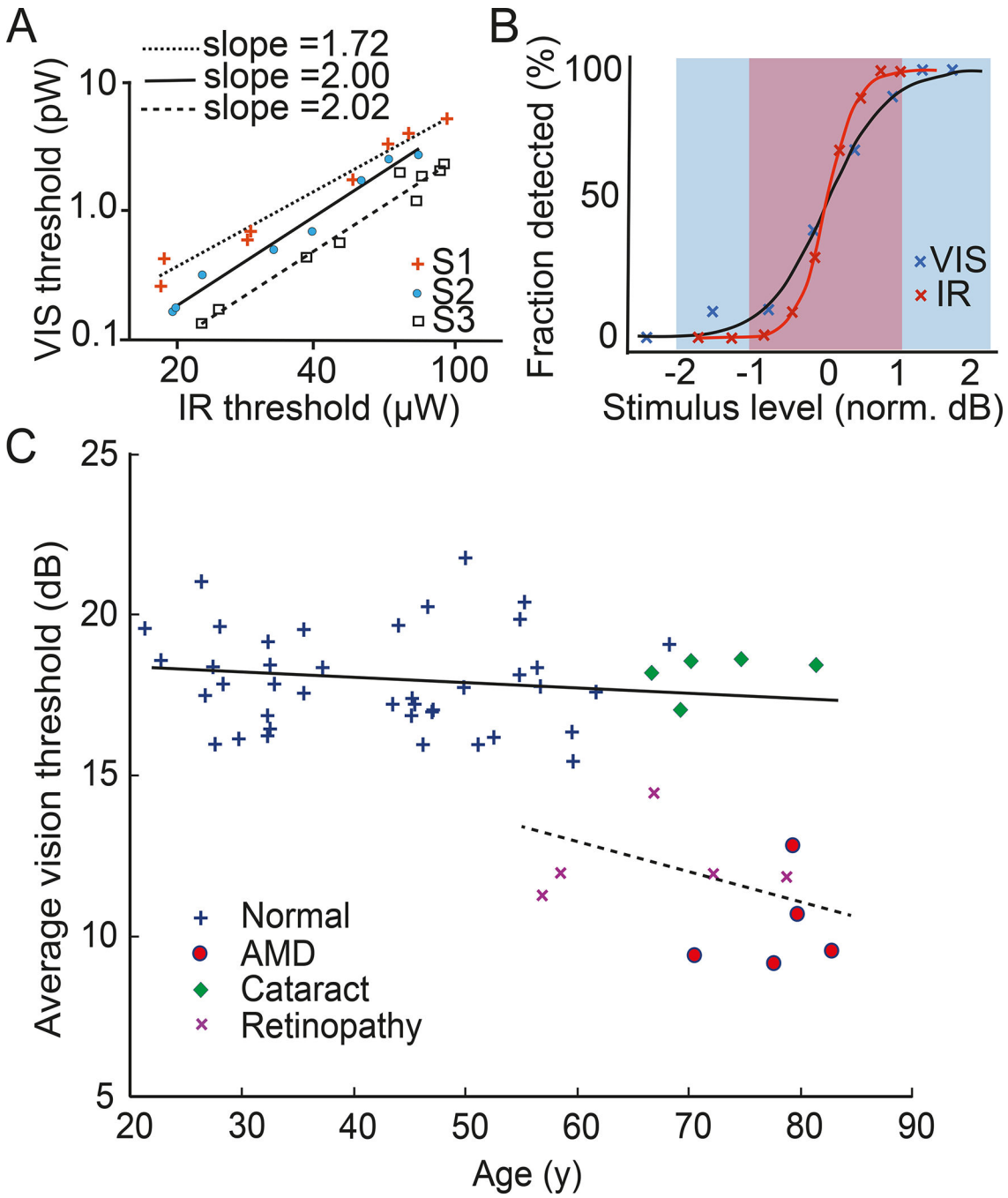

Fig. 22. Two-photon microperimetry measurements of human eyes:

(**A**) Graphs (log-log plots) of VIS light sensitivity thresholds *vs.* 2P vision obtained for three volunteers S1 (48 years old), S2 (61 years old), and S3 (32 years old). (**B**) Psychometric function design for visible and infrared light stimulation. In constructing the graph, values on the X-axis were normalized to the threshold power at which the stimulus pattern, VIS or IR, was visible in 50% of the trials. Ranges for 99.7% variation in psychometric function values are indicated with red background for IR, and blue background for visible light. (**C**) Average infrared visual thresholds for different age groups in the normal

population (crosses) compared with those in patients with AMD (red circles), cataracts (green diamonds), or diabetic retinopathy (purple crosses). Dashed and solid lines refer to the quantile of 0.50 for retinopathy and normal eyes, respectively. See open access publications (Labuz et al., 2020; Ruminski et al., 2019).

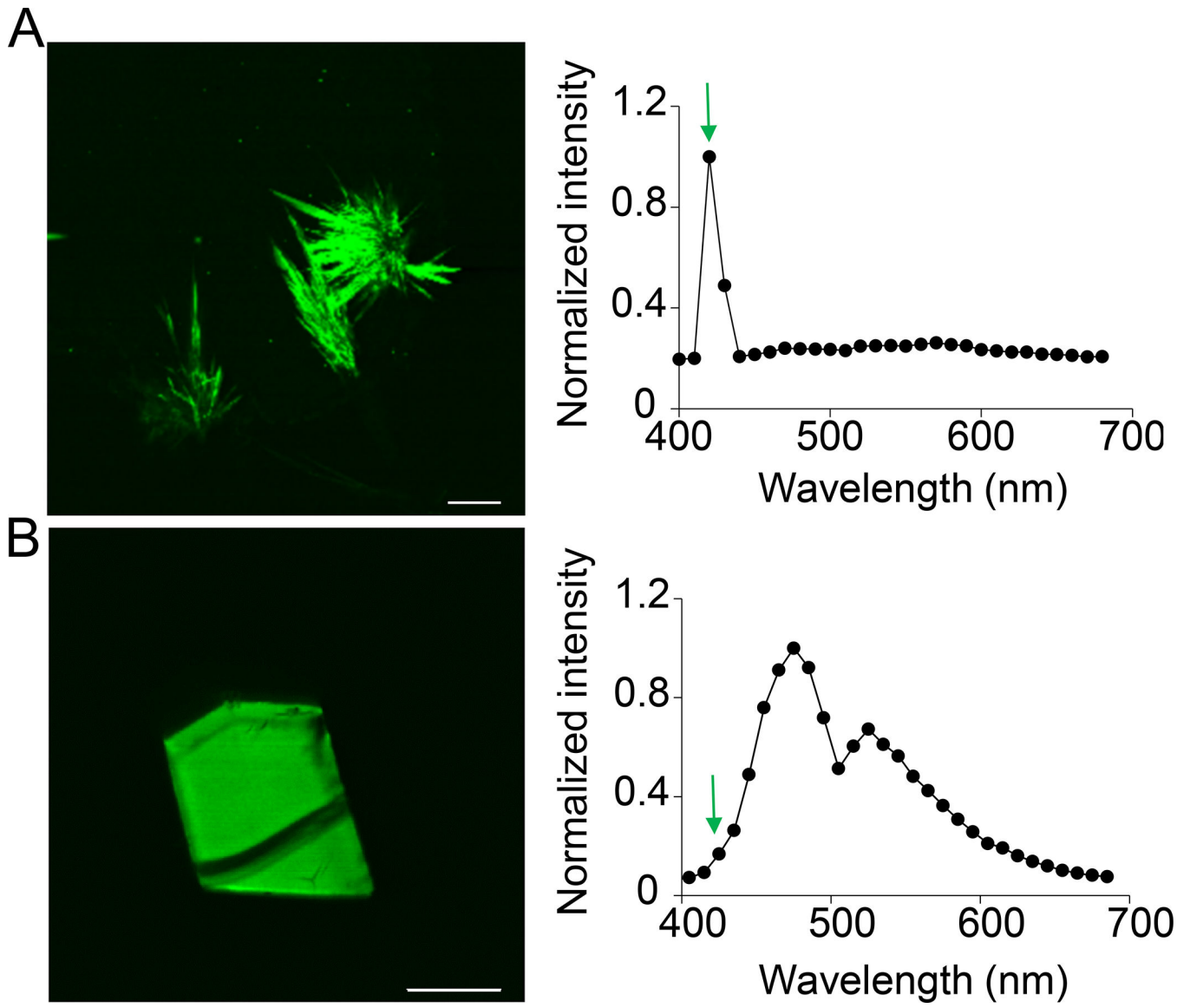

Fig. 23. Two-photon microscopy (TPM) imaging of protein crystals.

(**A**) Left, TPM image based on SHG from 5-HT4R crystals in mesophase (Padayatti et al., 2012); right, emission spectrum; green arrow indicates SHG. (**B**) Left, TPM image based on fluorescence emission from tetragonal lysozyme crystal; right, emission spectrum; green arrow indicates wavelength at which SHG signal was expected. Scale bars: 150 μm. Adapted with permission from P. Padayatti, G. Palczewska, W. Sun, K. Palczewski, and D. Salom. Imaging of protein crystals with two-photon microscopy, *Biochemistry* 2012, 51, 8, 1625–1637. Copyright 2012 American Chemical Society

Movie 1.

3D reconstruction of the *Abca4*$^{PV/PV}$*Rdh8*$^{-/-}$ mouse retina and RPE assembled from 2PEF images, obtained *ex vivo* using a 20-fs laser. Numbers along the X, Y, and Z axes indicate distances in μm. The RPE is located at the top of the 3D volume, z=0 μm; outer plexiform layer is at z=100 μm, and ganglion cell layer at around 200 μm.

Movie 2.

Retina in the intact eye of a BALB/c mouse 45 hr after intra-ocular injection with fluorescein-tagged PNA. RPE is at Z=0 μm; cone outer segments are visible directly under the RPE; cone pedicles are at 80 μm under the RPE. X and Y axes are stretched 2 times as related to the Z axis to visualize RPE-photoreceptor interdigitating. 2PEF microscopy images were obtained *ex vivo* with 800 nm excitation light.